POLITECNICO DI TORINO

SCUOLA DI DOTTORATO

Dottorato in Ingegneria per l'Ambiente Naturale e Costruito

- XXVII ciclo

PhD Dissertation

"*Pore-scale simulation of micro and nanoparticle transport in porous media*"

Candidate:

Francesca Messina

Tutors:

Prof. Rajandrea Sethi

Prof. Daniele Marchisio

April 2015

Ringraziamenti

La prima persona che voglio ringraziare è ovviamente Raja, come Professore, come capo, ma soprattutto come persona, per i continui incoraggiamenti a migliorarmi, per gli insegnamenti e la comprensione che spesso ha dimostrato in questo mio percorso.

Ovviamente un grazie a tutti i miei colleghi con i quali ho condiviso interamente o in parte questi tre anni, grazie per gli insegnamenti reciproci, gli aiuti, la condivisione di tante lunghe giornate e per aver reso la mia permanenza al Poli così piacevole e divertente: Tiziana, Alessandro, Michela, Francesca, Carlo, Eleonora, Alberto e Matteo. Un grazie anche a Daniele e Gianluca, per gli aiuti, i consigli e i confronti.

Thank you to Prof. Maša Prodanović for her help and discussions during my visit at UT, and to Maryam for having made my time in Austin so happy and pleasant.

Ovviamente un grande ringraziamento ai miei genitori, che mi hanno incoraggiata e spronata e che si sono sempre dimostrati pazienti e comprensivi.

Grazie a Diego che, non so come, è riuscito in tante circostanze a starmi vicino, a supportarmi (e sopportarmi) e ad esserci quando avevo bisogno.

Un grazie alle mie amiche "storiche": alla dolce Stefania, che fra bimbo (o forse bimbi?) in arrivo e un matrimonio mi ha regalato tante emozioni ed è sempre stata al mio fianco nei momenti più belli e più tristi. Alle triestine Stefania e Giorgia e al nostro trio che presto diventerà un felice quartetto, nonostante i quasi 600 km che ci separano, la nostra amicizia rimane quella di sempre e presto avremo un valido motivo per giocare nuovamente agli indiani nel giardino di Giò!

Un enorme ringraziamento alle amiche "più recenti" che nonostante le conosca da meno tempo sono state molto importanti in questi anni: Checca, che in poco tempo è diventata una super confidente e amica, che trova sempre le parole per aiutarmi e il tempo per ascoltarmi, con la quale non mancano mai le risate e le lunghe telefonate mentre mi alleno correndo, e Martina, la miglior vicina (quasi vegan) del mondo … non smetterò mai di ringraziarti per avermi svegliato alle due quella famosa notte, avrei altrimenti rischiato di non conoscerti mai … un amica sincera e schietta, pronta a darmi i suoi consigli e a farmi riflettere come pochi sanno fare!

E infine … un grazie a Te, ovunque tu sia … in qualche modo so che mi hai aiutato a portare a termine questo percorso e che non smetterai di starmi vicino.

Table of contents

Introduction

The transport and deposition of colloidal particles in saturated porous media are processes of considerable importance in many fields of science and engineering. A thorough understanding of particle filtration processes is essential for predicting the transport and fate of colloids in the subsurface environment (Tosco, et al. Submitted).

On the one hand, colloidal filtration is a phenomenon of pivotal importance to understand the propagation of contaminants and of microorganisms in aquifer systems (Bhattacharjee, et al. 2002; Bradford, et al. 2014; Liang, et al. 2013; Loveland, et al. 2003; Mccarthy and Zachara 1989; Schijven, et al. 2000; Seetha, et al. 2014; Syngouna and Chrysikopoulos 2012). This topic has received considerable attention due to the potential risk for human health: natural colloids can act as a carrier for a wide range of harmful strongly sorbing contaminants, thus extremely facilitating their migration into the subsurface. Moreover, bacteria, viruses, and engineered, potentially toxic nano-particles can also be found in the subsurface environment.

On the other hand, the study of colloids transport is also related to the development of new remediation technologies such as the use of micro- and nano-particles of zerovalent iron for groundwater remediation (Comba, et al. 2011; Dalla Vecchia, et al. 2009; Kocur, et al. 2014; O'Carroll, et al. 2013; Tosco, et al. 2014). In this context studying at the micro-scale the mechanisms that control the mobility of reactive micro- and nano-particles is essential for the design, implementation and performance evaluation of remediation field applications (Tosco, et al. 2013).

In addition to the groundwater environment, colloid transport in porous media is a relevant topic in numerous engineering applications. Particle transport and deposition are the basis of deep-bed granular filtration, commonly adopted in water and waste-water treatment and in other industrial separations (Tufenkji and Elimelech 2004). Particle removal efficiency and head loss along the packed bed both depend on a number of parameters, including suspension properties (particle size distribution and concentration, particle surface chemistry, and solution chemistry), filter design parameters (media size, type and depth), and operating conditions (filtration rate and filter runtime) (Cushing and Lawler 1998). Adequate predictive models are not yet available for use within a rational design framework, and hence, conservative designs or extensive pilot studies are required to develop design parameters. Responses to changes in influent quality or operating parameters are currently impossible to predict.

Other applications of colloid filtration processes are the clogging of depth filters and wells (Bensaid, et al. 2010; Bensaid, et al. 2009), the fine migration in proximity to production wells, which may be a critical issue for well efficiency and oil or gas production in petroleum engineering, enhanced oil recovery or imaging in reservoir engineering (Shi, et al. 2013), the delivery of agents for contrast (Tiraferri, et al. 2008) or for thermoradiotherapy in medicine (Gordon, et al. 2014; Pankhurst, et al. 2009) and several more (O'May and Tufenkji 2011).

Colloid transport is a peculiar multi-scale problem: pore-scale phenomena have an important impact on the larger-scale transport. Particles migrating through a porous medium can remain in suspension and be transported by advection and by dispersion phenomena, or can be retained by filtration (when the particle size exceeds the pore size or when the particle is entrapped in dead-end pores) and by deposition onto the porous matrix (phenomenon controlled by physical-chemical particle-particle and particle-porous medium interaction). For this reason, in recent years there has been a huge increase in the use of pore-scale modelling to study multiphase flow and transport in porous media (Blunt 2001). More specifically, concerning colloid transport, the motivation behind pore-scale modelling is to gain a better understanding of the mechanisms underlying colloidal processes such as deposition and aggregation, not only from a macro-scale point of view, but particularly at a micro-scale, studying the inter-granular dynamics (Elimelech 1995).

This thesis focuses on the study of particle transport and deposition in saturated porous media from a micro-scale point of view. The thesis is structured as follows:

- Chapter 1: An introduction on deep bed filtration is here given. Then an explanation about CFD simulations is presented: the representation of granular media, the flow field and particle transport simulation techniques. Also a description of the forces acting on particles and a literary review about the concept of single collector efficiency are provided.

- Chapter 2: The subject of this chapter is the development of a new correlation equation to predict single collector efficiency, a key concept in filtration theory. By performing Eulerian and Lagrangian simulations in a simple geometry and by using an innovative approach to interpret the results, a new correlation equation to predict single collector efficiency has been formulated. A hierarchical approach to interpret the results was exploited. The proposed correlation equation presents innovative features, such as validity for a wide range of parameters and total flux normalization. The final formula has also been extended to include porosity and a reduced model is proposed.

- Chapter 3: The good agreement between the correlation equation developed in the previous chapter and the existing models allows the validation of the simulation method used. Therefore, other simulations were performed in a geometry with a column of five spherical collectors. The results indicate that the behaviour of each collector of the column is different; in particular, when gravity is not negligible. Hence, at least two efficiency values have to be considered, one for the first sphere of the packing and another for the other grains. Two models, which need more refinement, are proposed.

1 Chapter 1 - Colloidal transport in porous media

This chapter is mainly based on the manuscript *Computational models for nanoparticle transport in porous media: from pore- to macro-scale* by Tosco T., Messina F., Sethi R., Crevacore E., Raoof A. and Hassanizadeh M.

1.1 Introduction to deep bed filtration

The deposition of colloidal particles in saturated porous media is a typical issue related to granular filtration and, more precisely, to deep bed filtration.

Granular filtration is a fluid–particle separation technology; it refers to a collection of processes for removing (as contaminants or impurities), separating (suspended particles from suspending fluid or one type of particles from a mixture of particles) and concentrating and recovering (as products) particles from fluid–particle suspensions. Most clarification processes operate on the principle of exclusion; this means that the size of the pores of the filter medium is such that particles suspended in the liquid are excluded to enter the pores. Such a particle-deposition mechanism is known as sieving and leads to the formation of filter cakes (cake filtration).

Conversely, in deep bed filtration a diluted suspension of particles in injected in a filter of granular or fibrous materials to remove the fines and/or colloidal particles present in the fluid phase. In this case particle deposition in the medium is obtained through interception, sedimentation and Brownian diffusion (see paragraph 1.5): particle deposition takes place at various depth throughout the medium: for this reason this kind of filtration is called deep-bed filtration (Tien and Payatakes 1979; Tien 1989).

Deep bed filtration is essential for a large number of manufacturing industries (chemical, mineral, food and beverages) as well as to pollution abatement and environment control. The fluid phase can be a liquid or a gas; besides water or air, also other substances may be treated by granular filtration, such as flue gas, combustion products, molten metal, petrochemical feedstocks, polymers, alcoholic or non-alcoholic beverages (Tien 1989). One of the most notable applications of depth filtration is the use of sand filters for the treatment of water and wastewater (Figure 1-1), but other applications of deed bed filtration are very common.

Figure 1-1: Water treatment plant aerial view.

Also in the groundwater engineering field, the use of micro and nano-particles of zerovalent iron (MZVI - NZVI) for groundwater remediation is related to deep bed filtration (Figure 1-2). As a matter of fact, when the injected suspension flows through the porous medium (the solid matrix of the aquifer), some particles, due to several forces acting on them, move toward and become deposited on the surface of the aquifer matrix (particle deposition). This process depends on several parameters (e.g., water and particle chemistry, particle and flow field characteristics, etc.) and should be understood in order to correctly design field scale interventions.

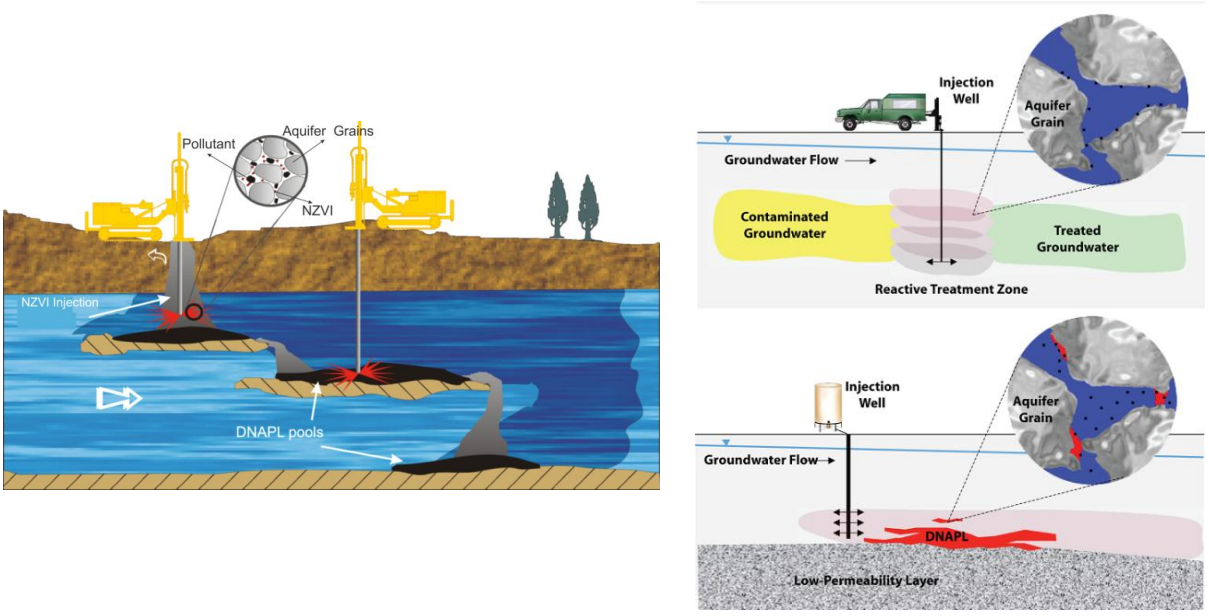

Figure 1-2: Schematic representations of NZVI injection in aquifer systems.

Particle deposition and filtration are intrinsically transient processes, since deposited material changes both the geometry of the interstitial spaces of the filter (porous medium) and the nature of the collector surfaces, therefore affecting the deposition of other colloidal particles. Nevertheless, due to the complexity of the topic, it is usually modelled under steady state conditions, assuming that the deposited particles suddenly "disappear" after

contacting the filter medium (clean bed filtration theory). This assumption is valid at the initial stage of the phenomenon.

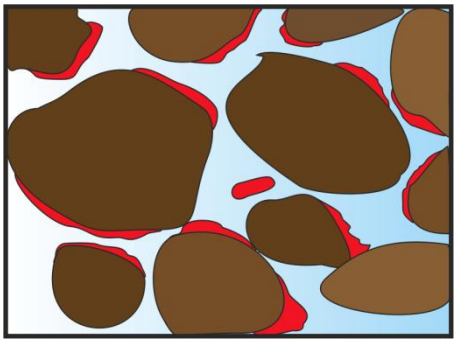

Figure 1-3: Changes of grain shape and of interstitial spaces in a porous medium as results of particle deposition.

The main issues related to deep bed filtration which need to be investigated are the nature of the conditions leading to the retention of particles throughout the filter bed: a reasonably complete understanding of the pertinent phenomena is essential for the establishment of a comprehensive deep bed filtration theory which can be used as support of rational designs. The ultimate objective is to derive mathematical formulations which quantitatively describe the complete dynamics of deep bed filtration, taking into account the complete interactions between the filter grains and the particles in the liquid solution to be removed as well as the effect of operating and system variables. For this purpose the phenomenon needs to be studied from a micro scale point of view since the complex system of particle-grain interactions and the deposition mechanisms are not visible at a larger scale: microscopic theories of deep bed filtration are intended to provide information and insight about the mechanisms of particle deposition, the condition under which deposition may be facilitated or hindered. On the other hand, the macroscopic studies are aimed at the phenomenological description of the filtration process, the prediction of its dynamic behaviour, and the development of methodologies and techniques for design, calculation and optimization (Tien and Payatakes 1979).

In the following paragraphs the numerical approach to study particle deposition from a microscale point of view will be presented, starting from the representation of a porous medium, then analyzing fluid flow and colloid transport simulations.

1.2 Representation of granular media

The soil structure and, in particular, the grains and consequently the pores shape of a deep-bed filter form a complex and random structure, and the hydrodynamic of the system cannot be described in details in a

mathematical framework at this time. This problem, related to the complexity of the system, can be approached in two different ways (Cushing and Lawler 1998):

- the physical system can be approximated crudely enough that an exact mathematical solution to the problem is feasible (analytical solution);
- a more accurate representation of the system can be used and this requires an approximate mathematical solution (numerical solution).

For large portions of porous medium (e.g., for the representation of a typical column used in laboratory tests of colloid transport), the solution of flow and transport equations in the pores is not feasible, and up-scaled continuum averaged equations must be considered. Moreover, when solving large-scale problems (e.g., multi-dimensional representation of field-scale processes), modelling approaches are still under development, and up-scaled kinetics are to be defined from lower scales, from the micro-scale.

At the pore scale, the porous medium is represented as an assembly of collectors, whose structure, geometry and size distribution must be known into details (Tien 1989). The geometry of the collectors can be geometrically simplified (e.g., spheres) or realistic and obtained from imaging of a real sample (i.e. a packed sand sample). One grain (single collector) or multiple packed grains (multiple collectors) can be considered, both in two or three dimensions. An overview of the most commonly adopted geometric representations is reported in Figure 1-4.

The simplest representation of a single collector is a 2D circle or a 3D sphere, which allow exploiting the radial symmetry of the collector by adopting polar coordinates. It is also possible to represent non perfect spherical collectors and to explore the influences of mineral-grain shape and of surface roughness (Saiers and Ryan 2005). Moreover, for a detailed study of phenomena arising at grains contact and in the inter-granular space, Ma and co-authors (Ma, et al. 2009) proposed the hemispheres-in-cell model, which incorporates grain-to-grain contact. Johnson et al. (Johnson, et al. 2007) used two porous media packing structures: simple cubic (SC) packing and dense cubic (DC) packing. Moreover the sinusoidal constricted tube accounts for the geometry nature of the pores: collectors (soil grains) are piled up and leave many interstitial pores with constricted passages (Wei and Wu 2010).

Regarding multiple collectors, synthetic 2D or 3D geometries usually adopt an assembly of circles (or spheres) arranged in an ordered pattern, e.g. the dense cubic packing arrangement presented by (Cushing and Lawler 1998), or randomly packed (Prodanovic, et al. 2010). Sometimes a domain (normally 3D) of randomly packed collectors with irregular geometries are adopted (Boccardo, et al. 2014).

Another approach are pore network models, in which a network made by spheres are connected by channels representing the void spaces. In the most simple case, pore volumes are located at the knots of a regular lattice, whereas in more complex pore network models a large variety of irregular networks can be selected (Blunt and King 1990; Fenwick and Blunt 1998; Lowry and Miller 1995; Mehmani, et al. 2013).

Realistic representations of the pore space geometry, in both 2D and 3D, are sometimes adopted, even though in this case computational costs are significantly higher, and the reconstruction of the pore space requires specific software. The geometric characteristics of pores and channels and the pores position can be chosen randomly from prescribed distributions, or alternatively are selected to match experimentally determined pore space geometries (Meakin and Tartakovsky 2009), while the structure of a granular medium can be obtained by carrying out image analyses of real samples. For 2D domains, SEM images of grains can be used (Tosco, et al. 2013), and 3D digital images can be obtained from high-resolution three-dimensional X-ray tomography or NMR tomography experiments.

Each representation of the pore space corresponds to a different degree of simplification, and consequently requires different simplifying assumptions when solving flow and transport equations. In the following paragraphs, an overview of the approaches adopted in the most common cases is provided and briefly discussed (Tosco, et al. Submitted).

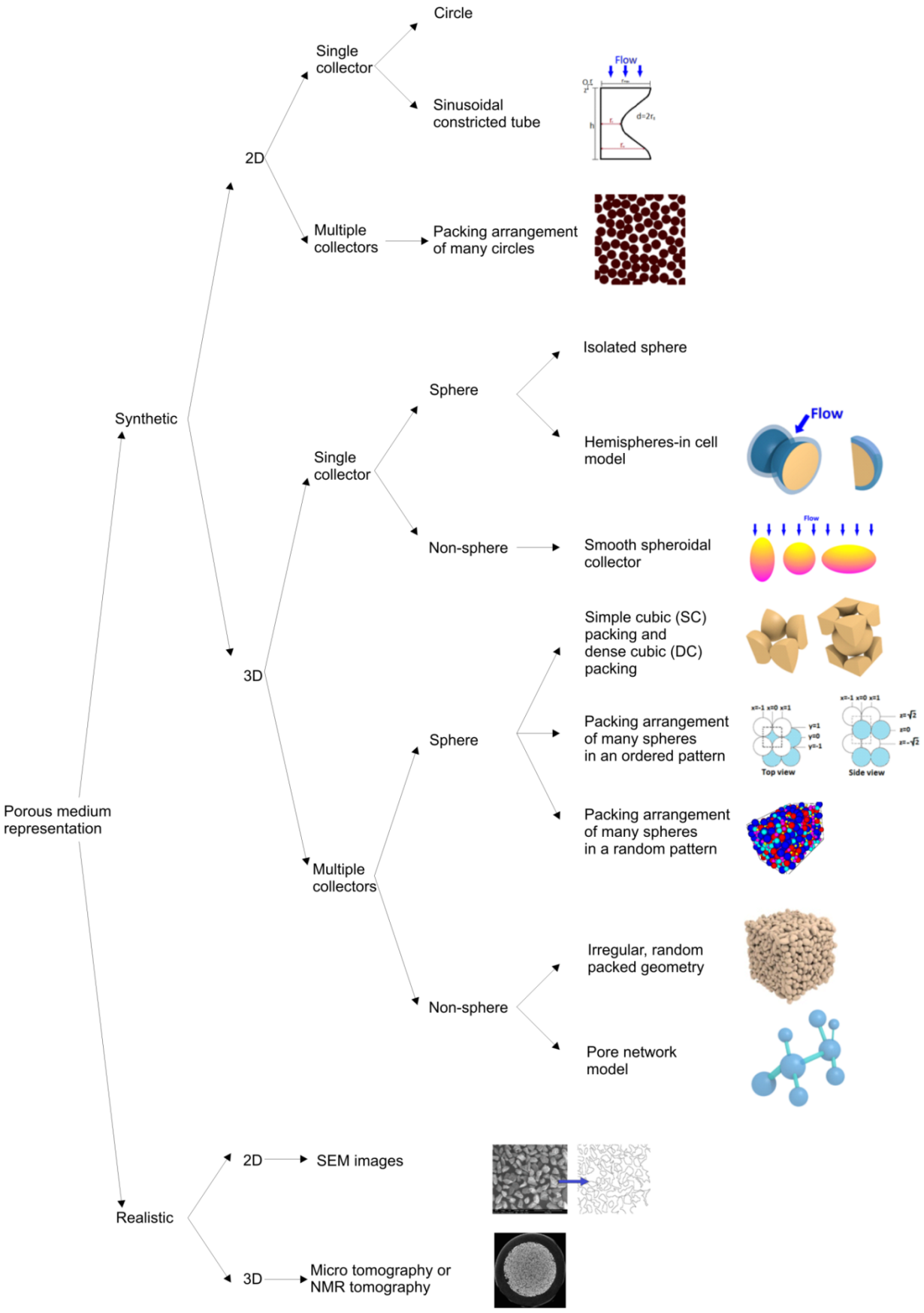

Figure 1-4: Geometric representations of a porous medium [from (Tosco, et al. Submitted)].

1.3 Flow field description in granular media

When studying colloid transport in most part of the geometries and approaches described above, it is commonly assumed that flow and colloid transport are not coupled problems (i.e., the presence of colloidal particles does not affect the flow field). As a consequence, a quantitative description of the undisturbed flow field is an essential prerequisite to the solution of the transport problem, and the flow field must be solved before simulating colloid transport with any approach (Elimelech 1995).

As a general rule, the flow behaviour of the carrier fluid is described by mass and momentum conservation equations, usually written in the differential form, for intensive variables (Ferziger and Peric 1999). The equations can be closed and simplified thanks to some approximations and assumptions on the nature of the fluid considered. The most common assumption consists in incompressible, Newtonian fluid (Elimelech 1995; Ferziger and Peric 1999): in this case the continuity equation and the Navier-Stokes equations are (Elimelech 1995):

$$\nabla \cdot \mathbf{v} = 0$$

Eq. 1-1

$$\frac{\partial \mathbf{v}}{\partial t} + \mathbf{v} \cdot \nabla \mathbf{v} = -\frac{\nabla p}{\rho} + \frac{\mu}{\rho} \nabla^2 \mathbf{v} + f_e$$

Eq. 1-2

where μ is the constant (dynamic) viscosity, $\boldsymbol{v}$ is the fluid velocity (vector), p is the hydrostatic pressure and $\boldsymbol{f_e}$ is the external forces exerted on a unit mass of the fluid. In most cases, steady state is assumed and the external forces are neglected, thus leading to the (dimensionless) formulation:

$$N_{Re} \tilde{\mathbf{v}} \cdot \nabla \tilde{\mathbf{v}} = -\nabla \tilde{p} + \nabla^2 \tilde{\mathbf{v}}$$

Eq. 1-3

where $\tilde{\mathbf{v}}$ and $\tilde{p}$ are the normalized (dimensionless) velocity vector and fluid pressure:

$$\begin{cases} \tilde{\mathbf{v}} = \dfrac{\mathbf{v}}{U_0} \\ \tilde{p} = \dfrac{pL_0\mathbf{v}}{\mu U_0} \\ N_{Re} = \dfrac{pL_0U_0}{\mu} \end{cases}$$

Eq. 1-4

N_{Re} is the Reynolds number and it describes the ratio of inertial forces (linear term $\tilde{\mathbf{v}} \cdot \nabla \tilde{\mathbf{v}}$) to the viscous one (non-linear term $\nabla^2 \tilde{\mathbf{v}}$) (Elimelech 1995; Ferziger and Peric 1999). The lower is N_{Re}, the more the momentum equation is close to a linear equation, the higher is N_{Re}, the more the non-linear terms are important. In the first case the solution of the equation is ordered and so the fluid flow is *laminar*, while in the second case the solution is disordered, and then the flow is *turbulent*. It is worth to mention that the value of the Reynolds number, and hence the flow regime, is determined by the characteristic length scale and velocity used for reference. Thus, although a suspension flowing through a pipe at high speed may be turbulent, the local flow field around each suspended particle may still be laminar.

For $N_{Re} << 1$, under steady state conditions and neglecting external forces, Eq. 1-2 can be simplified leading to Stokes or *creeping* flow equation (Eq. 1-5), which is important to describe the flow field in porous media.

$$\nabla^2 \mathbf{v} = \frac{\nabla p}{\mu}$$

Eq. 1-5

Eq. 1-5 has the advantage of being a linear differential equation, so the superposition technique can be employed to decompose complex flow field into simpler ones (Elimelech 1995).

The conservation equations can be written in different forms, depending on the coordinate system and on the basis vectors used. For example, one can select Cartesian, cylindrical, spherical, curvilinear orthogonal or non-orthogonal coordinate system, which may be fixed or moving. The choice depends on the geometry, the target flow and may influence the discretization method and grid type to be used (Ferziger and Peric 1999).

Experience shows that Navier-Stokes equations describe the flow of a Newtonian fluid accurately, but only in few cases and in very simple geometries (e.g., flow around an isolated sphere) it is possible to obtain an exact, analytical solution of the momentum and Navier-Stokes equations (Elimelech 1994; Tien 1989). In other cases, an analytical solution can be still retrieved, but under the assumption of neglecting some terms of the equations or assuming simplified boundary conditions. Such assumptions may be acceptable under a restrictive number of hypotheses (Ferziger and Peric 1999). More in general, in those cases when simplifying assumptions required for analytical solutions cannot be accepted, or when the pore space geometry is irregular and a detailed flow field is required, a numerical solution can be obtained applying the computational fluid dynamics approach (CFD). In these cases, a key aspect is the selection of the discretization method, i.e. the method of approximating the differential equations by a system of algebraic equations for the variable at some set of discrete locations in space and time. Many approaches are available, whose detailed discussion is beside the purpose of this study. However, among the approaches more often adopted in the field of colloid transport, finite differences (FD),

finite volumes (FV) and finite elements (FE) methods are all worth to be mentioned. Other methods, like spectral schemes, boundary element methods and cellular automat are used in CFD, but their use is limited to special problem categories (Ferziger and Peric 1999).

In the following paragraphs the most commonly used approaches to the solution of the flow field in pore-scale models are summarized. The section is not intended as an exhaustive an complete description of all available models for pore-scale flow simulations, but focuses specifically on those approaches which are most used for colloid transport simulations and which will be used in the next chapters.

1.3.1 Flow past a single sphere

In most cases, a porous medium grain, called collector, may be approximated as a sphere, and the granular medium is therefore represented as a set of collectors, each of them behaving in a similar way. Under such an assumption, spherical coordinates are adopted for a more efficient representation of the domain. In some cases (e.g., isolated sphere, Happel's and Kuwabara's models) a symmetry along the vertical axis is assumed, and consequently the flow is solved in 2D (coordinates r and θ, Figure 1-5a-b), while in other cases a full 3D domain is required (hemisphere-in-cell model Figure 1-5c).

The simplest model represents the grain as an *isolated sphere* in an infinite fluid domain, and each grain in the porous medium is totally independent from the others. The flow field around the grain is solved as the flow of fluid of infinite extent over a single sphere, under creeping flow conditions (i.e., Stokes solution). If spherical coordinates with symmetry with respect to the vertical axis are adopted (Figure 1-5a), the following boundary conditions can be imposed:

$$\begin{aligned} &\text{a) } v_r = 0, v_\theta = 0 && \text{for } r = a_c \\ &\text{b) } v_r \to -U_\infty \cos\theta && \text{for } r \to \infty \\ &\text{c) } v_\theta \to -U_\infty \sin\theta && \text{for } r \to \infty \end{aligned}$$

Eq. 1-6

where r and θ are the coordinates, v_r and v_θ are the components of the fluid velocity along, respectively, r and θ, U_∞ is the modulus of the undisturbed (vertical) flow velocity at infinite distance from the sphere and a_c is the radius of the collector. An analytical solution can be derived for creeping flow (Tien 1989):

$$v_r = -U_\infty \cos\theta \left(\frac{1}{2}\frac{a_c^3}{r^3} - \frac{1}{2}\frac{a_c}{r} + 1 \right)$$

Eq. 1-7

$$v_\theta = -U_\infty \sin\theta\left(-\frac{1}{4}\frac{a_c^3}{r^3}-\frac{3}{4}\frac{a_c}{r}+1\right)$$

Eq. 1-8

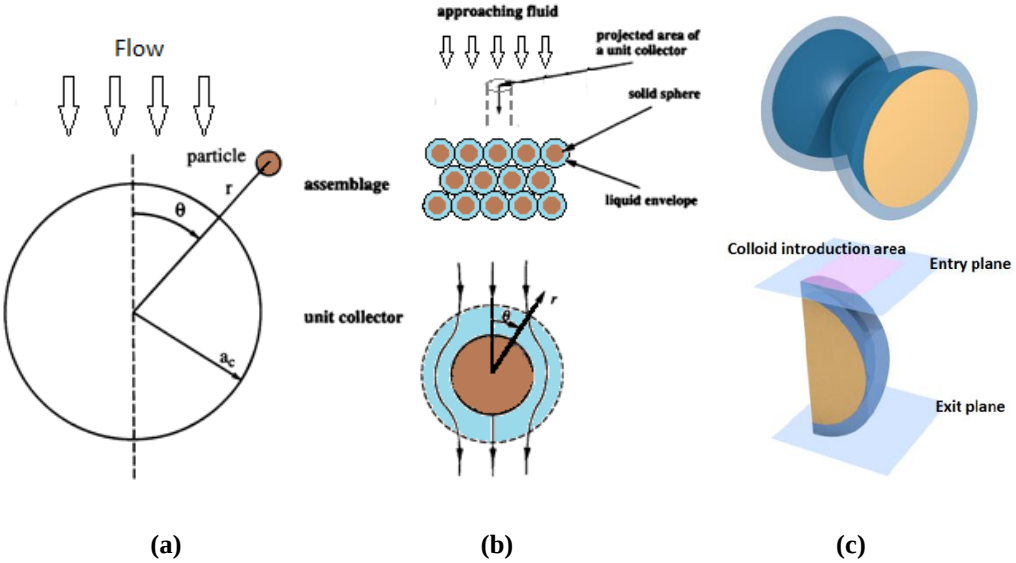

(a) **(b)** **(c)**

Figure 1-5: Schematic description of single sphere models for homogeneous porous media: (a) isolated sphere (Elimelech 1994), (b) Happel's model (Elimelech 1994), and (c) hemisphere-in-cell model (Ma, et al. 2009).

A set of models involving a single spherical collector, but also taking into account possible modifications to the flow due to the vicinity of other grains are the so called *sphere-in-cell models*, among which the *Happel's model* (Happel 1958) is the first, and probably the most widely applied one (Rajagopalan and Tien 1976; Tufenkji and Elimelech 2004). In such model the granular medium is represented as a collection of identical cells consisting of a solid sphere surrounded by a fluid envelope whose thickness is proportional to the porous medium porosity (Figure 1-5b). The flow field is usually solved by use of the stream function (Rajagopalan and Tien 1976). In the Happel's model in particular, the collector is a sphere of radius a_c surrounded by a fluid envelope of radius b (Figure 1-5b). The sphere radius a_c represents the actual radius of the collector, while b scales with a_c and the porosity n of the porous medium:

$$b = a_c\left(1-n\right)^{-\frac{1}{3}}$$

Eq. 1-9

The equation of motion for the creeping flow is solved assuming symmetry around the vertical axis (i.e. variation along the third spherical coordinate ϕ is neglected) and the following boundary conditions are imposed (Tien 1989):

$$\begin{aligned} &\text{a) } v_r = 0, v_\theta = 0 \qquad \text{for } r = a_c \\ &\text{b) } v_r \to -U_\infty \cos\theta \qquad \text{for } r = b \\ &\text{c) } \frac{1}{r}\frac{\partial v_r}{\partial \theta} + r\frac{\partial}{\partial r}\left(\frac{v_\theta}{r}\right) = 0 \qquad \text{for } r = b \end{aligned}$$

Eq. 1-10

In this simplify geometry an analytical solution exists (Elimelech 1994):

$$v_r = -\frac{1}{r^2 \sin(\theta)}\frac{\partial \Psi}{\partial \theta}$$

Eq. 1-11

$$v_\theta = \frac{1}{r \sin(\theta)}\frac{\partial \Psi}{\partial r}$$

Eq. 1-12

where Ψ is the stream function, which general solution is Eq. 1-13 and the particular Happel's coefficient are defined in Eq. 1-14.

$$\Psi = A\left[K_1\left(\frac{a_c}{r}\right) + K_2\left(\frac{r}{a_c}\right) + K_3\left(\frac{r}{a_c}\right)^2 + K_4\left(\frac{r}{a_c}\right)^4\right]\sin^2(\theta)$$

Eq. 1-13

$$\begin{aligned} A &= U a_c^2 / 2 \\ K_1 &= 1/w \\ K_2 &= -(3 + 2\gamma^5)/w \\ K_3 &= (2 + 3\gamma^5)/w \\ K_4 &= -\gamma^5 / w \end{aligned}$$

Eq. 1-14

with γ and w defined by:

$$\begin{aligned} \gamma &= (1-n)^{1/3} = a_c / b \\ w &= 2 - 3\gamma + 3\gamma^5 - 2\gamma^6 \end{aligned}$$

Eq. 1-15

The *Kuwabara's model* is identical to Happel's model in conception and formulation, but it applies different boundary conditions (Happel and Brenner 1983; Tien 1989):

$$\begin{aligned} &\text{a) } v_r = 0, v_\theta = 0 && \text{for } r = a_c \\ &\text{b) } v_r \to -U_\infty \cos\theta && \text{for } r = b \\ &\text{c) } \frac{\partial v_\theta}{\partial r} + \frac{v_\theta}{r} - \frac{1}{r}\frac{\partial v_r}{\partial \theta} = 0 && \text{for } r = b \end{aligned}$$

Eq. 1-16

The *hemisphere-in-cell model* has been proposed as an extension and generalization of the Happel's model to incorporate the effects of a grain-to-grain contact (Ma, et al. 2009). The spherical collector is represented as a portion (i.e. a quarter) of a sphere, surrounded by a shell of fluid. Symmetry planes along the two sections of the sphere and at the portion representing grain-to-grain contacts are applied (Figure 1-5c). Continuity and steady state Navier-Stokes equations under laminar flow assumption are solved in full spherical coordinates (i.e. r, θ and ϕ) by imposing the following boundary conditions:

$$\begin{aligned} &\text{a) } v_r = 0, v_\theta = 0, v_\phi = 0 && \text{for } r = a_c \\ &\text{b) } v_r \to U_\infty \cos\theta && \text{for } r = b \\ &\text{c) } v_\theta = \frac{U_\infty}{2}\sin\theta\left(\frac{-4+3\gamma+5\gamma^3-6\gamma^5+2\gamma^6}{2-3\gamma+3\gamma^5-2\gamma^6}\right) && \text{for } r = b \\ &d) \; v_\phi = 0 && \text{for } r = b \end{aligned}$$

Eq. 1-17

where γ is defined in Eq. 1-15. No closed-form solution is available for this model, and the flow filed is therefore solved numerically (Ma, et al. 2009).

It is finally worth to mention the Brinkman's model (Brinkman 1947), another approach which couples the pore-scale accurate solution of the flow field around a sphere with a large-scale, continuum solution of flow at large distances. In this case, the collector is represented as a solid sphere of radius a_c, embedded in a granular mass. The flow field far from the collector is solved by applying the Darcy law, while close to the sphere surface the Navier-Stokes equations are applied under creeping flow conditions (Tien 1989):

$$\nabla p = -\frac{\mu}{k}\mathbf{v} + \mu\nabla^2\mathbf{v}$$

Eq. 1-18

where k is the permeability. By imposing the boundary conditions reported in Eq. 1-19, it is possible to recover the analytic formulation for both the components of the velocity vector, v_r and v_θ.

$$\text{a) } \mathbf{v} = 0 \qquad \text{for } r = a_c$$
$$\text{b) } \mathbf{v} = U_\infty \qquad \text{for } r = b$$

Eq. 1-19

The above presented models, despite their differences, are all formulated on the assumption that a relatively simple configuration can be used to represent randomly packed granular media, but due to their simplicity they only approximate realistic porous media (Tien 1989). With the only exception of the isolated sphere model, all of them, even if representing processes taking place around a single collector, do not neglect the presence of the surrounding porous medium, with different degrees of approximation, which make them suitable for different problems, depending on the required accuracy of the solution.

1.4 Pore-scale particle transport simulations

Two theoretical approaches are available to simulate colloid transport and to calculate the particle deposition rate onto the porous medium, namely Lagrangian and Eulerian approaches. Any of the two approaches is chosen, it is necessary to know which are the mechanisms of transport that determine particle movement into the porous medium, which are the forces that act on particles and the natures of the interactions between colloids and the grains of the solid matrix (collectors) in which they move.

In theoretical analysis of colloidal deposition system, it is usually assumed that the presence of colloidal particles does not disturb the flow field of the carrying fluid, therefore flow and transport problems are treated independent (Elimelech 1995). In the next paragraph the forces acting on particles and the particle-porous medium interactions mechanisms will be described.

1.4.1 Forces acting on an uncharged particle

The *gravity force* is the algebraic sum of two contributors: the weight force of the particle and the buoyancy force (see Table 1-1).

The simplest formulation for the *drag force* is reported in Table 1-1 and it holds under general conditions (Brenner 1961). However, corrections are required when the particle size is comparable with the average free path of fluid particles, or when the particle is close to the surface of the collector. In this second case in

particular, close to the collector surface the particle velocity differs from that of the fluid in the same point, and the drag force has to be corrected by applying coefficients called hydrodynamic correction functions, presented in Table 1-2 (Warszyński 2000). These coefficients are function of H, the dimensionless distance between particle and collector equal to h/a_p, where h is the distance between the two surfaces and a_p is the particle radius. The trend of these functions is shown in Figure 1-6.

Table 1-1: Mathematical formulation of the forces acting on colloidal particles. Parameters: *v* fluid velocity, *u* particle velocity, a_p particle radius, ρ_p particle density, ρ_f fluid density, *g* acceleration of gravity, μ is the fluid viscosity, *R* random-normal distribution number, k_B Boltzmann constant, *T* absolute temperature, ξ friction coefficient (equal to $6\pi\mu a_p$), Δt simulation time step.

Forces	Mathematical expressions
Gravity force	$\mathbf{F_G} = \frac{4}{3}\pi a_p^3 \left(\rho_p - \rho_f\right)\mathbf{g}$
Drag force	$\mathbf{F_D} = 6\pi\mu a_p \left(\mathbf{v}-\mathbf{u}\right)$
Brownian force	$F_B = R\sqrt{\frac{2\xi k_B T}{\Delta t}}$

Table 1-2: Hydrodynamic correction function and their range of variability (Warszyński 2000).

$f_1(H) = \frac{19H^2 + 4H}{19H^2 + 26H + 4} \quad \forall H$
$f_2(H) = 1 + \frac{1.79}{(0.828 + H)^{1.167}} \quad \forall H$
$\begin{cases} f_3(H) = \frac{1}{0.754 - 0.256\ln(H)} & \text{for } H < 0.137 \\ f_3(H) = 1 - \frac{0.304}{(1+H)^3} & \text{for } H \geq 0.137 \end{cases}$
$\begin{cases} f_4(H) = \frac{1}{1.062 - 0.516\ln(H)} & \text{for } H < 0.11 \\ f_4(H) = \left(\frac{H}{2.639 + H}\right)^{1/4} & \text{for } H \geq 0.11 \end{cases}$

The drag force is therefore, for freely moving particles, corrected to take into account the presence of a rigid wall that influences its motion. The force is corrected in both its component: the normal and the tangent to the wall surface; also the rotating motion is modified. The new formulation of the Drag force is reported in Eq. 1-20, where the subscripts *n* and *t* count for *normal* and *tangential* components of both the particle and the fluid velocities.

$$\begin{cases} F_D^n = 6\pi\mu a_p u_n f_2 - \dfrac{6\pi\mu a_p v_n}{f_1} \\ F_D^t = 6\pi\mu a_p u_t \dfrac{f_3}{f_4} - \dfrac{6\pi\mu a_p v_t}{f_4} \end{cases}$$

Eq. 1-20

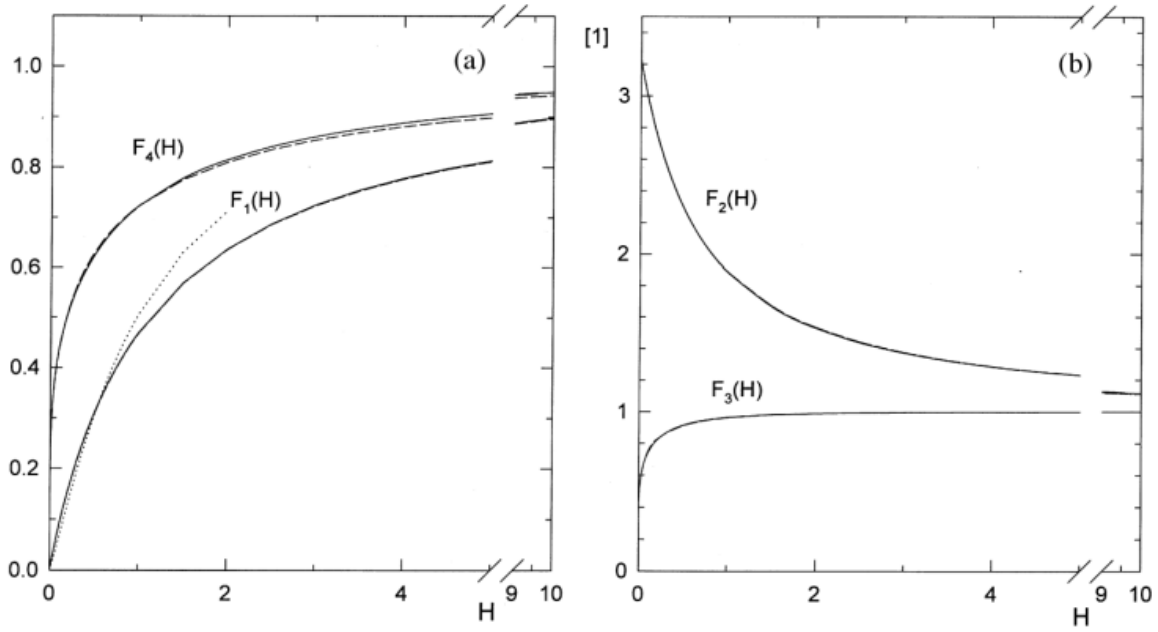

Figure 1-6: Graphical representation of the hydrodynamic correction function [From: (Warszyński 2000)].

The studies show that the increase of the hydrodynamic resistance in the presence of macroscopic interfaces is due to the viscous resistance to the motion exerted on the fluid by the solid. The correction to the component of particle velocity perpendicularly to the rigid interface is significantly larger than the one applied to the parallel component: during the movement towards the rigid wall the liquid is pushed out of the gap between particle and interface and this phenomena requires much more energy than the drag of the liquid near the rigid wall by the particle (parallel motion).

The *Brownian force* (see Table 1-1) is usually modelled as a Gaussian white noise process and must be decomposed in normal and tangential components (Eq. 1-21), in order to take into account the hydrodynamic retardation.

$$\begin{cases} F_B^n = R\sqrt{\dfrac{2\xi_n k_B T}{\Delta t}} \quad \text{with} \quad \xi_n = \dfrac{6\pi\mu a_p}{f_1(H)} \\ F_B^t = R\sqrt{\dfrac{2\xi_t k_B T}{\Delta t}} \quad \text{with} \quad \xi_t = \dfrac{6\pi\mu a_p}{f_4(H)} \end{cases}$$

Eq. 1-21

Brownian motion cannot be solved analytically, but rather as a series of uncorrelated random movements. For a correct calculation, the time step Δt employed in the trajectory simulation should fulfil specific requirements:

- the time step must be much greater than the particle momentum relaxation time, m/ξ, ξ being the friction coefficient ($6\pi\mu a_p$) and m the particle mass;
- the time step must be small enough to consider all forces constant during the time step considered (Ma, et al. 2009).

1.4.2 Interactions among charged bodies: DLVO and extended DLVO theory

The *DLVO* (*Derjaguin-Landau-Verwey-Overbeek*) *theory* defines the interaction potentials between two faced charged surfaces, which is given by the combined effects of Van der Waals attraction and electrostatic repulsion. According to the classical DLVO theory, the interaction potential between two surfaces is the sum of the attractive Van der Waals interaction and of the electrostatic interaction (repulsive or attractive):

$$V_{tot} = V_{VdW} + V_{EDL}$$

Eq. 1-22

where V indicates the potential energy [J]. Colloids are assumed to be uniform spheres, small relative to the sand grains which can be considered as a plate. In the following, formulas for sphere-plate interactions are reported, for calculation of particle-collector interactions. Particle-particle interactions are obtained with the sphere-sphere geometry, and can be shown to be half the value of sphere-plate interactions (Derjaguin's approximation) (Elimelech 1995).

London-Van der Waals forces are generated by fluctuating spontaneous electrical and magnetic polarizations that give rise to an electromagnetic field in the region between the surfaces. The magnitude of this force depends on material properties of the particles, of the filter medium and of the solution. Van der Waals interaction for a single-species electrolyte is usually calculated following Hamaker's approach (Elimelech 1995), basing on Gregory's formulation (Gregory 1981):

$$V_{VdW} = -\frac{Aa_p}{6h\left(1+\frac{14h}{\lambda}\right)}$$

Eq. 1-23

where A is the Hamaker constant, a_p is the particle radius, h is the distance between the two bodies and λ is the characteristic wavelength of the interaction, that accounts for the retardation effect due to the finite time of propagation of the interaction. The value of 100 nm is often used for λ (Elimelech 1995). The formulation is accurate for $h<0.1a_p$. For larger distances other formulations are available (Elimelech 1995; Lifshitz 1956).

The Van der Waals force, obtained from $F_{VdW} = -\nabla V_{VdW}$, is always attractive and acts along the direction normal to the surface **n** (Eq. 1-24).

$$\mathbf{F_{VdW}} = -\frac{Aa_p}{6h^2}\frac{\lambda(\lambda+28h)}{(\lambda+14h)^2}\mathbf{n}$$

Eq. 1-24

The Hamaker constant depends on the properties of the particle, of the collector and of the separating medium; several formula exist to estimate it, between those the one proposed by (Hunter 2001) is:

$$A_{132} \approx \left(\sqrt{A_{11}} - \sqrt{A_{33}}\right)\left(\sqrt{A_{22}} - \sqrt{A_{33}}\right)$$

Eq. 1-25

where A_{132} is the Hamaker constant for the material 1 interacting with the material 2 through the material 3. Similarly, A_{11} is the constant for the material 1 interacting with the same material through void space, A_{22} for the material 2, and A_{33} for the material 3.

Electrical double layer interaction is due to the partial overlapping of the diffuse double layers that surround the faced particles or surfaces (Masliyah and Bhattacharjee 2006). As the charge in the double layer depends on the charge on the particle surface, the interaction for particles of the same material is always repulsive. A number of solutions for the calculation of V_{EDL} are available, that are valid over different ranges of distances and under different assumptions. As a general rule, the interaction potential (or the force) depends on the separation distance, on the ionic strength and on the charge or potential at each surface. However, analytical formulations depend on the boundary conditions applied at the surfaces. For similarly charged surfaces, the *constant charge approach* (no relaxation of the electric double layer) yields the largest repulsive force or energy barrier, whereas the *constant potential approach* (fully relaxed electric double layer) yields much lower values. An intermediate

solution is provided by the *regular surface interaction* (Tobiason and O'Melia 1988). For most natural and synthetic colloids interacting with natural porous media, the equation proposed by Hogg and co-workers (Hogg, et al. 1966) could be considered the most appropriate, based on the assumption of constant potential at the surface (CPA):

$$V_{EDL} = \varepsilon_0 \varepsilon_r \pi a_p \frac{\zeta_p^2 + \zeta_c^2}{4} \left[\frac{2\zeta_p \zeta_c}{\zeta_p^2 + \zeta_c^2} \ln\left(\frac{1+e^{-\kappa h}}{1-e^{-\kappa h}} \right) + \ln\left(1-e^{-2\kappa h}\right) \right]$$

Eq. 1-26

where ζ_p and ζ_c are respectively the particle and the collector zeta potential, κ is the Debye-Huckel reciprocal length, h is the distance between the two bodies, a_p is the particle radius, ε_0 is the dielectric constant of the free space and ε_r is the relative dielectric constant of the fluid. The Debye-Huckel reciprocal length κ is calculated as in Eq. 1-27, where e is the electron charge ($-1.602 \cdot 10^{-19}$ C), $n_{i,0}$ is the bulk number concentration of ions of the i-th type (tied to the ionic strength), z_i is the valence of the i-th ions, k_B is the Boltzmann constant ($1.381 \cdot 10^{23}$ J/K), T is the absolute temperature, ε_0 is the dielectric permittivity of the free space and ε_r is the relative dielectric permittivity of the fluid.

$$\kappa = \sqrt{\frac{e^2 \sum_i n_{i,0} z_i^2}{\varepsilon_0 \varepsilon_r k_B T}}$$

Eq. 1-27

The CPA approach is valid for $\zeta_p \approx \zeta_c < 60$ mV and $\kappa a_c > 5$, its accuracy decreases for small separation distances. From the potential formulation of the electric double layer, the force can be calculated:

$$\mathbf{F_{EDL}} = \varepsilon_0 \varepsilon_r a_p \frac{\left(\xi_p^2 + \xi_c^2\right) \kappa e^{-\kappa h}}{2\left(1-e^{-2\kappa h}\right)} \left[2\frac{\xi_p \xi_c}{\left(\xi_p^2 + \xi_c^2\right)} - e^{-\kappa h} \right] \mathbf{n}$$

Eq. 1-28

The sum of Van der Waals attraction and electrical double layer repulsion can result in a completely repulsive profile (Figure 1-7a), in a completely attractive profile (Figure 1-7b), or in a profile with a primary and a secondary minimum (Figure 1-8). When particle and sand grains are similarly charged, both Van der Waals and electrical double layer interactions are attractive: no repulsive barrier exists and deposition takes place under favorable conditions. The primary negative (attractive) minimum is always found, as attractive Van der Waals forces predominate at small separation distances. Particles are stably deposed on the porous matrix when they can reach this minimum, and are likely not to be released unless the profile changes dramatically (irreversible attachment). Conversely, when surface charges of particles and collector are opposite in sign, the electrical

double layer interaction is repulsive: the deposition takes place under unfavourable deposition conditions, and a barrier against deposition can exist. In this case only few colloids are able to overcome the barrier and to stably depose in the primary minimum. However, in some cases, a secondary, weak minimum is also found at larger distances, where particles can reversibly depose (Figure 1-8). Also moderate changes in pore water chemistry can significantly affect the depth of this minimum, thus causing a release of the particles (reversible attachment). Changes in solution chemistry promote, in fact, colloid mobilization mainly by altering the double layer potential energy. The attractive Van der Waals forces are independent of changes in solution chemistry. Short-range (up to a few nanometers separation distance) repulsion forces may also be affected by changes in solution chemistry, but these forces are not yet understood well enough to assess their effects. The change in solution chemistry must produce repulsive forces between attached colloids and grains that exceed the attractive forces. According to the energy barrier approach, the rate of colloid mobilization depends on the height of the barrier in DLVO potential energy that attached colloids must exceed (Ryan and Elimelech 1996). Electrical interaction between colloidal particles (especially in aqueous systems) is one of the most important influences on particle stability, aggregation and deposition. In most cases, the only practical means of manipulating the stability of particles and their tendency to deposit on surfaces is by changing the electrical interaction through changes in the solution chemistry.

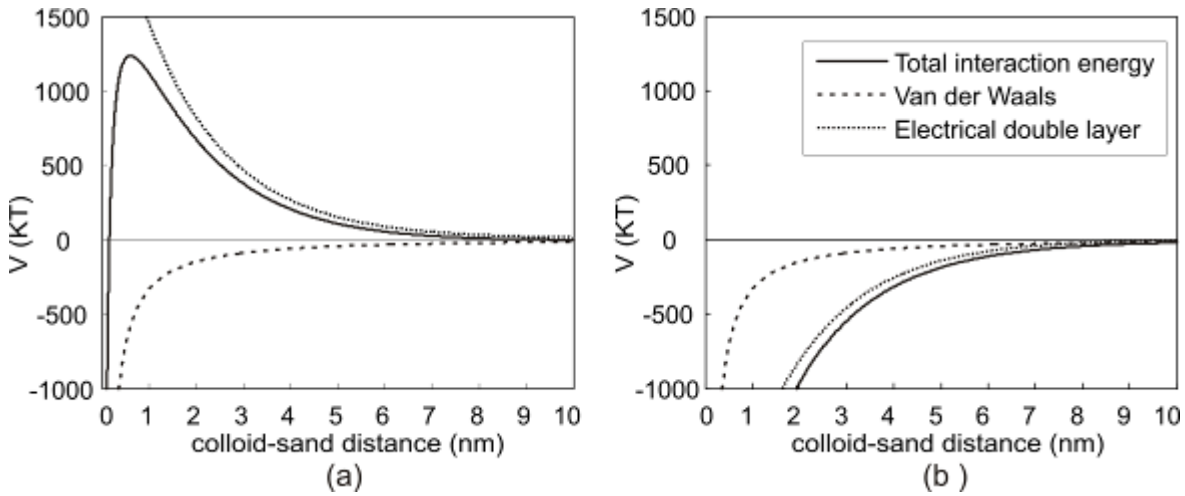

Figure 1-7: Interaction energy profile for a sand (plate) – colloid (sphere) system in unfavourable (a) and favourable (b) deposition conditions. Values of the parameters: $A = 1 \cdot 10^{-20}$ J, $a_p = 0.95$ µm, $\lambda = 100$ nm, $\varepsilon_r = 78.5$, $T = 296$ K, $I = 100$ mM, $\zeta_c = -2.56 \cdot 10^{-2}$ V, colloid surface potential $\zeta_p = -5.57 \cdot 10^{-2}$ V (case a), $\zeta_p = +5.57 \cdot 10^{-2}$ V (case b). [From (Tosco 2010)].

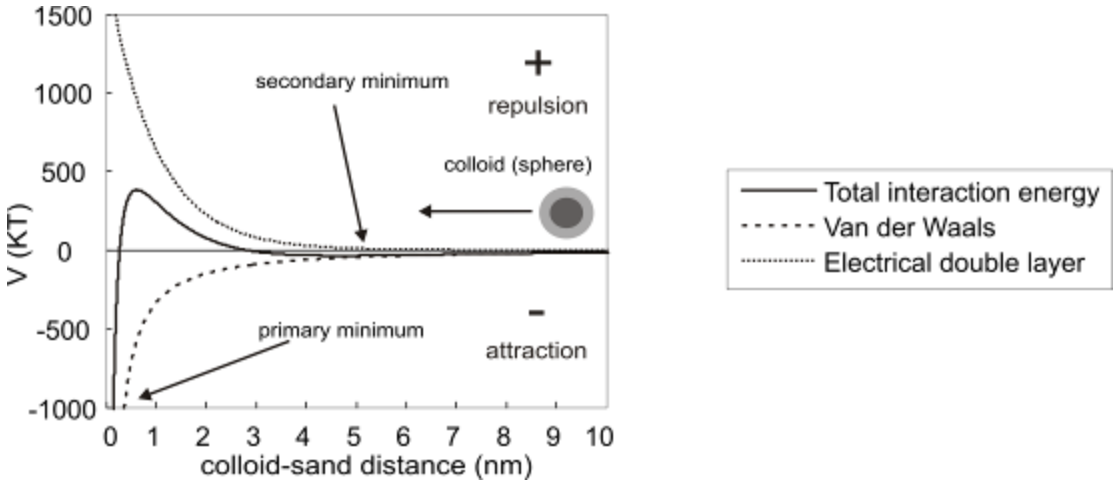

Figure 1-8: Interaction energy profile for a sand (plate) – colloid (sphere) system. Values of the parameters: A = 1·10-20 J, a_p = 0.95 µm, λ = 100 nm, ε_r = 78.5, ζ_c = -2.56·10-2 V, ζ_p = -3.74·10-2 V, T = 296 K, I = 100 mM. [From (Tosco 2010)].

Beside the two interaction forces considered by the classical DLVO theory, additional interaction forces can be taken into account:

- *Born repulsion*, due to short-range repulsive forces generated by the interpenetration of electron shells, when the surface-surface distance significantly decreases;
- *Osmotic repulsion*, due to osmotic forces generated by compression of the brush layer (polymer chains and liquid phase) that surrounds colloidal particles, when they approach each other;
- *Elastic repulsion* due to the presence of polymeric chains adsorbed on particle surface;
- *Magnetic attraction*, that generates between surfaces with a residual magnetic saturation also in the absence of external magnetic fields.

Also for these additional interactions the hypothesis of linear superposition of all potentials (or forces) contributing to the overall interaction profile is assumed (Kamiyama and Israelachvili 1992).

Although a rigorous formulation for inter-atomic potentials (Born repulsion plus London-van Der Waals interaction) should be based on quantum-mechanics, several simplified formulations were proposed in the past, e.g. the Lennard-Jones potential (Hunter 2001). An estimation for the Born *repulsion* alone, with an accuracy comparable to that of DLVO theory, was firstly proposed by Ruckenstein and Prieve (Ruckenstein and Prieve 1976):

$$V_b = \frac{A\sigma_c^6}{7560}\left[\frac{8a_c + h}{(2a_c + h)^7} + \frac{6a_c - h}{h^7}\right]$$

Eq. 1-29

where σ_c is the collision diameter, usually estimated equal to 0.5 nm (Elimelech 1995).

In many real applications, when the presence of adsorbed polymer chains on the surface of colloids is likely to occur, Born repulsion never acts a significant role, as polymers prevent colloids to approach closer than few nanometers, or fractions of the nanometer (Elimelech 1995).

The combined effects of osmotic and elastic interactions give rise to the so-called *steric repulsion*, generated by the compression of the brush layer that surrounds the colloidal particles (Vincent, et al. 1986). *Osmotic interactions* can be calculated following Vincent et al. (Vincent, et al. 1986):

$$\begin{cases} V_{osm}(0 < h < l) = \dfrac{2\pi d_c \phi_x^2}{\bar{v}}(0.5 - \chi) l^2 \left[\dfrac{h}{2l} - 0.25 - \ln\dfrac{h}{l}\right] \\ V_{osm}(l < h < 2l) = \dfrac{2\pi d_c \phi_x^2}{\bar{v}}(0.5 - \chi) l \left[l - \dfrac{h}{2}\right]^2 \\ V_{osm}(h > 2l) = 0 \end{cases}$$

Eq. 1-30

where φ_x is the volume fraction of the brush layer occupied by the adsorbed polymer, $\bar{v}$ is the volume of one single polymer molecule, χ is the Flory-Huggins parameter (that assumes values lower than 0.5 for good solvents, higher for bad solvents; for colloidal particles dispersed in water typical values range between 0.45 and 0.48) and l is the thickness of the brush layer.

The *elastic interaction* can be calculated as:

$$\begin{cases} V_{el}(0 < h < l) = \dfrac{\pi a_p}{2M_w}\phi_x l^2 \rho_x \left[\dfrac{h}{l}\ln\left(1.5 - \dfrac{h}{2l}\right)^2 - 6\ln\left(1.5 - \dfrac{h}{2l}\right) + 3\left(1 - \dfrac{h}{l}\right)\right] \\ V_{el}(h > l) = 0 \end{cases}$$

Eq. 1-31

where M_w is the molecular weight of the polymer and ρ_x is the density of the polymer (Vincent, et al. 1986).

The magnetic interaction between two generic magnetic dipoles is calculated as (de Vicente, et al. 2000; Garcia-Otero, et al. 2000; Matijevic 1971):

$$V_m = \frac{\nu_0}{4\pi}\left[\frac{\overline{m_1}\cdot\overline{m_2}}{h^3} - 3\frac{\left(\overline{m_1}\cdot\bar{h}\right)\left(\overline{m_2}\cdot\bar{h}\right)}{h^5}\right]$$

Eq. 1-32

where $\overline{m_1}, \overline{m_2}$ are the magnetic dipole moments, and v_0 is the magnetic permeability in the vacuum (equal to $4\pi \cdot 10^{-7}$ Tm/A). For two identical dipoles ($m_1=m_2=m$), and a head-to-tail disposition of magnetic dipoles, the magnetic interaction reduces to:

$$V_m = -\frac{\pi v_0 M_s^2 d_p^3}{9\left(\frac{2h}{d_p}+2\right)^3}$$

Eq. 1-33

where M_s is the saturation magnetization of the material (de Vicente, et al. 2000; Phenrat, et al. 2007).

1.4.3 Eulerian and Lagrangian approaches to investigate particle transport

As already pointed out, the study of colloid transport can be faced with two approaches: the Lagrangian method which describes the trajectory of the particles or the Eulerian method which describes the evolution of particle concentration in time and space (Elimelech 1994).

The Lagrangian approach is suitable for the representation of the trajectories of individual particles at a microscopic level. Conversely, the Eulerian approach describes the particles collectively, in terms of their distribution or probability density function, in time and space (Elimelech 1995; Tufenkji and Elimelech 2004).

In case of Lagrangian approach the equation of motion, or Newton's law (defined in Eq. 1-34), where m is the mass of molecule, $\boldsymbol{f}$ is the resultant force acting on it and $\boldsymbol{u}$ is the particle velocity, needs to be solved.

$$m\frac{d\mathbf{u}}{dt} = \mathbf{f}$$

Eq. 1-34

In Eq. 1-34 the term $\boldsymbol{f}$ counts for all the forces presented before: drag force, gravity, interaction forces (DLVO) and also the Brownian force, which has a random direction. However even though the Lagrangian approach is, in principle, capable of dealing with Brownian particles, typically it has been used to describe the non-Brownian particles motion because their trajectories are deterministic and easier to express analytically. The representation of Brownian motion requires, in turn, the addition of a thermal random force in the equation, thus leading to a Langevin's type equation, the solution of which results in stochastic trajectories (Elimelech 1994). The solution of such equation requires laborious and time-consuming step-by-step integration of the stochastic equation of motion and, from a practical point of view, it is feasible only for a limited number of particles (Elimelech 1995).

Eulerian methods have been the most widely employed for describing transport and deposition phenomena at larger scales and in the presence of a considerable number of particles: the difficulty of accounting for Brownian

effects is eliminated, and these methods are more amenable to numerical or to approximate analytical solutions (Elimelech 1994). For this reason, the Lagrangian approach was less attractive than the Eulerian approach, especially before the widespread availability of high-performance computers. The Eulerian approach is based on the solution of the convective diffusive equation:

$$\frac{\partial c}{\partial t} + \nabla \cdot (\mathbf{v}c) = \nabla \cdot (D \nabla c) - \nabla \cdot \left(\frac{\mathbf{D} \cdot \mathbf{F}}{k_B T} c \right)$$

Eq. 1-35

where $\boldsymbol{v}$ is local fluid velocity, c is the particle concentration, $\boldsymbol{D}$ is the particle diffusion tensor, k_B is the Boltzmann constant, T is the absolute temperature and $\boldsymbol{F}$ is the external force vector which takes into account the gravity force and the interaction forces (i.e., Van der Waals force and electric double layer). In this case the Brownian force is implicitly considered in the diffusion tensor. Quite often this can be considered as a scalar coefficient, normally evaluated with the Stokes - Einstein's formulation (Eq. 1-36). Rarely this coefficient is corrected with the hydrodynamic retardation functions to account for, also in the Brownian force, the effects due to the presence of a solid wall.

$$D = \frac{k_B T}{6 \pi \mu a_p}$$

Eq. 1-36

Also the local fluid velocity $\boldsymbol{u}$ should be corrected with the appropriate hydrodynamic functions if hydrodynamic retardation is considered.

In order to solve Eq. 1-35, boundary conditions are required; two are the possibilities:

- *Perfect sink model*: this model assumes that all particles approaching the collector surface will be immediately and irreversibly adsorbed and subsequently disappear from the system. Concentration equal to zero is, therefore, set on the collector surface. This model ignores the formation of a separated phase (deposit) formed by adsorbed particles at the interface, and precludes the possibility of immobilization reaction at the finite rate. Therefore, prediction based on this model are only applicable to the initial stage of the deposition process (Elimelech 1995).

- *Non penetration model*: this model specifies a vanishing normal flux component at the collector surface.

1.5 The single collector deposition efficiency

Deposition of particles from a suspension to the collector surface may be viewed as a two-step process: (1) the transport of the particle from the bulk of the suspension to the proximity of the collector surface and (2) the subsequent particle adhesion to the collector/grain surface, which depends upon the nature of surface-particle interactions (Tien 1989).

The transport of colloidal particles from the pore fluid to the vicinity of a filter grain (collector) can be due to three mechanisms: advection, gravity and Brownian diffusion (Messina, et al. 2015). The particle deposition on the porous medium sand grains is typically described by three mechanisms: gravitational sedimentation, interception and Brownian diffusion (respectively represented Figure 1-9) (Tufenkji and Elimelech 2004). Gravitational sedimentation is due to the settling of the particles when their density is higher than that of water, interception happens when the particle touches the collector due to its finite size while moving along a streamline and Brownian diffusion is caused by the Brownian thermal movement that determines the divergence of particles from a streamline and brings them to the grain surface.

Colloid deposition due to interception and gravity grows with an increase in the size of the suspended particles, while transport by diffusion increases with a decrease in particle size. In general, under physical conditions typical for water and wastewater filtration, the transport of sub-micrometric particles is dominated by diffusion while that of larger (non- Brownian) particles is dominated by interception (Elimelech 1995).

The second step, properly called *attachment*, is controlled by surface interaction forces, which can be described using the Derjaguin-Landau-Verwey-Overbeek (DLVO) theory. Therefore, if the conditions are favourable to deposition (e.g., the net colloidal force is attractive), the transport stage dictates the rate of deposition. On the contrary, if the conditions are unfavourable (e.g., there is an energy barrier for particles to overcome before being deposited), the deposition stage decides the rate of deposition (Elimelech 1995).

The aim of pore-scale transport models is to predict removal of particles as a function of suspension characteristics, physical and chemical properties of the filter and flow conditions. Important suspension characteristics include: density, size, particle size distribution and surface chemistry, temperature, viscosity and solution chemistry of the suspending medium. The parameters which describe the properties of packed-bed filters are: bed depth, grain size, grain shape, grain surface chemistry and porosity. Another important parameter in packed-bed filtration is the approach (superficial) velocity U, defined as the ratio of the volumetric flow rate to the filter cross-section area (Elimelech 1995).

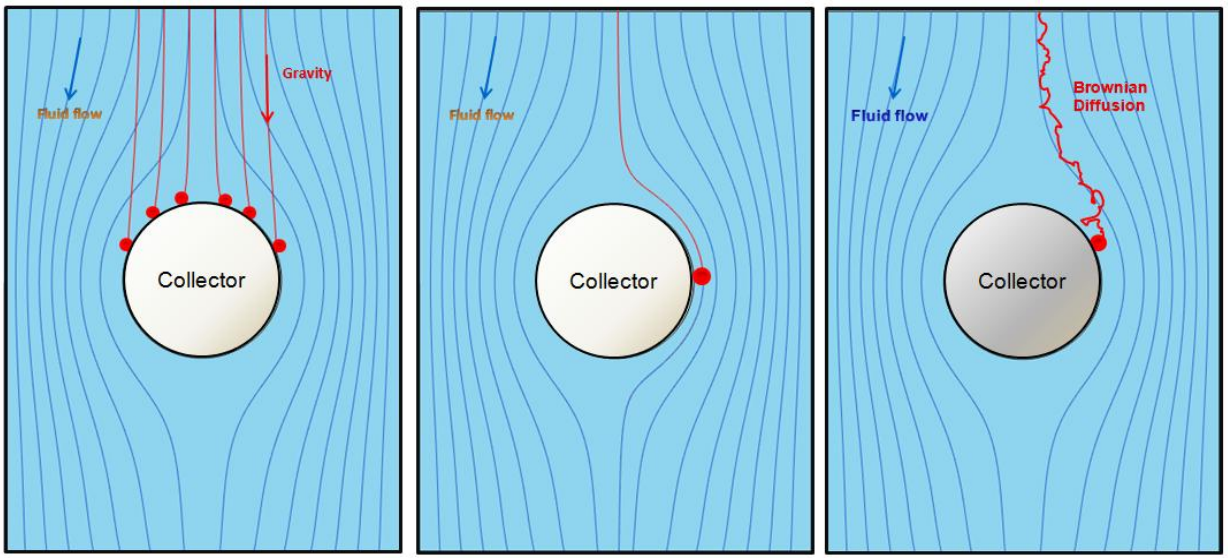

Figure 1-9: The three particle deposition mechanisms.

In clean bed filtration (Yao, et al. 1971), the first step of the deposition process is usually quantified by η_0, the single collector contact efficiency, that expresses the number of particles that reach the collector I_s divided by the advective rate entering through an area equal to the projection of the collector (Eq. 1-37, where U is the approach velocity, a_c is the collector radius and C_0 is the influent particle concentration). The second step is commonly quantified by the attachment efficiency α, which is the fraction of the particles coming into contact with the collector that actually attaches onto it. The product of these two values gives, as a result, the single collector removal efficiency η, which accounts for both the transport and attachment steps (Eq. 1-38) (Elimelech 1995; Petosa, et al. 2010). η_0 is related to non-chemical processes while α is and an empirical collision efficiency, describing the attachment step due to DLVO interactions and other processes not included in η_0.

$$\eta_0 = \frac{I_S}{UC_0\left(\pi a_c^2\right)}$$

Eq. 1-37

$$\eta = \alpha\eta_0$$

Eq. 1-38

Normally η_0 is calculated with microscale equations while α is determined experimentally; numerous approaches have been proposed for the calculation of η_0 from microscopic (fundamental) equations. η and η_0

are equivalent in case of favourable chemistry condition (when α =1) (Elimelech 1995; Tobiason and O'Melia 1988).

The deposition of colloids in porous media has been investigated by several researchers to improve existing methods by incorporating the forces such as hydrodynamic and attractive forces into the governing equations.

In this context it is essential to mention the *Smoluchowski-Levich approximation* which assumes that *(i)* the particle-wall hydrodynamic interaction is counterbalanced by Van der Waals attractions between particles and the wall, and all other colloidal and external forces are absent or simply neglected, *(ii)* particles move with the undisturbed fluid velocity and *(iii)* interception plays no role in deposition. For particles with diameter smaller than about 0.1 μm, the use of the Smoluchowski-Levich approximation may be adequate and so the deposition rate can be calculated neglecting Van der Waals forces, electrical double layer and hydrodynamic interactions.

Both the Eulerian and Lagrangian approaches have been used to derive a correlation equation for η_0 (or η, depending on the forces considered). The Eulerian approach, since it requires lower computational efforts, was the first approach applied in these studies. On the other hand, the Lagrangian method, based on trajectory analysis, is more computationally demanding and has been widely applied more recently, thanks to the increasing powerful computers and sophisticated numerical software. It was first applied to all deposition phenomena except Brownian motion, due to the excessive computational requirements (Elimelech 1995; Tobiason and O'Melia 1988), and only recent studies fully incorporated Brownian motion also in trajectory analysis.

Early studies on the definition of η_0 were carried out using analytical calculations. The first evaluation of particle deposition due to Brownian diffusion (in presence of both diffusion and advection) on a spherical collector in an infinite fluid flow domain was proposed by Levich (Levich 1962). His result was then used by Yao et al. (Yao, et al. 1971), the first who proposed a complete model to predict particle deposition due to interception, gravity and diffusion onto a single spherical collector in an undisturbed vertical flow with no influence of possible surrounding collectors. In this model interaction forces were not considered, therefore η_0 was investigated. Yao et al. (Yao, et al. 1971) deposition efficiency formulation was obtained assuming that the three deposition mechanisms listed above are additive, thus the three terms corresponding to Brownian diffusion deposition (η_D), gravity deposition (η_G) and interception (η_I) were derived and summed, without considering any possible interaction. This assumption of additivity was later on validated by Prieve et al. (Prieve and Ruckenstein 1974). The formulation proposed by Yao et al. (Yao, et al. 1971) is presented in Table 1-3; the three terms are respectively η_D, η_G and η_I, which trend and contributions are shown in Figure 1-10.

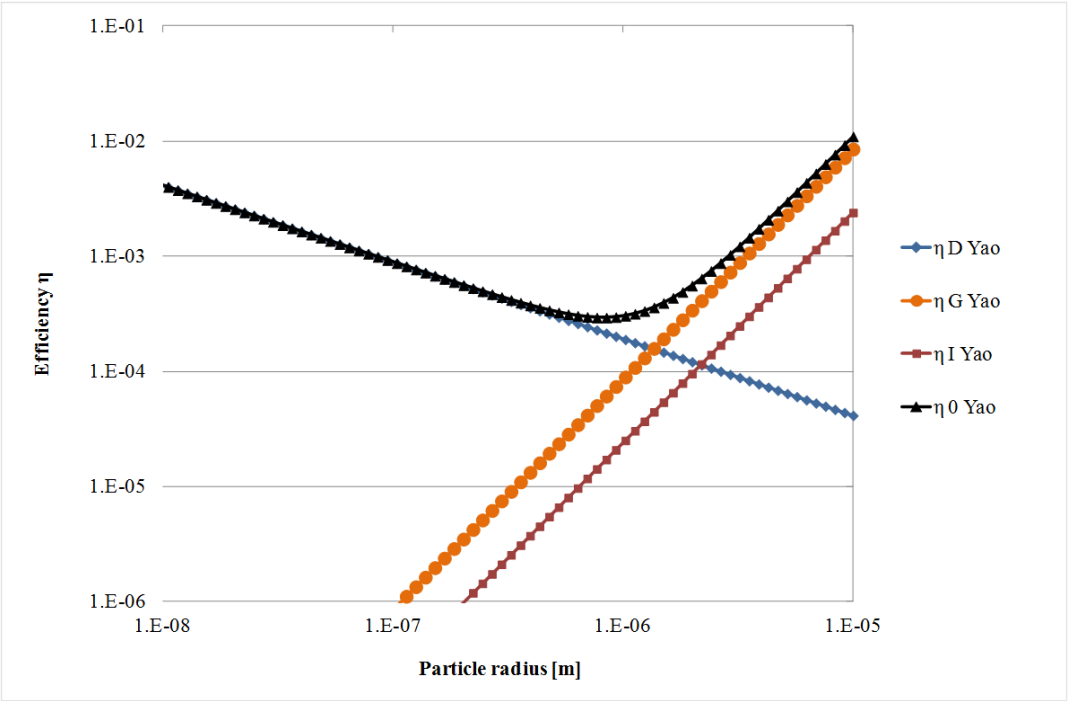

Figure 1-10: The trend of the single collector correlation equation proposed by Yao et al. (Yao, et al. 1971) and the contributions of the three terms, η_D (in blue), η_G (in orange) and η_I (in red) are also highlighted. Data: U=1.36·10^{-3}m/s, ρ_p =1050 kg/m^3, ρ_f =998 kg/m^3, T=298 K, μ =9.8·10^{-4} Pa·s, a_c =250 µm. [Adapted from (Yao, et al. 1971)].

Table 1-3: List of the main existing correlation equations to predict single collector contact (or removal) efficiency. See Table 1-4 for the parameter definitions.

Acronym	Authors	Equation
Yao	Yao et al. 1971 (Yao, et al. 1971)	$\eta_0 = 4.04 N_{Pe}^{-2/3} + \frac{3}{2} N_R^2 + N_G$
RT	Rajagopalan and Tien 1976 (Rajagopalan and Tien 1976) Corrected by Logan et al. (Logan, et al. 1995)	$\eta_{0,\gamma} = \gamma^2 \left[4.04 N_{Pe}^{-2/3} A_S^{1/3} + A_S N_R^{15/8} N_{Lo}^{1/8} + 0.00338 A_S N_G^{1.2} N_R^{-0.4} \right]$
TE	Tufenkji and Elimelech 2004 (Tufenkji and Elimelech 2004)	$\eta_0 = 2.4 N_R^{-0.081} A_S^{1/3} N_{Pe}^{-0.715} N_{vdW}^{0.052} + 0.55 A_S N_R^{1.675} N_A^{0.125} + 0.22 N_R^{-0.24} N_G^{1.11} N_{vdW}^{0.053}$
MPFJ	Ma et al. 2009 (Ma, et al. 2009)	$\eta_\gamma = \gamma^2 \left[2.3 A_S^{1/3} N_R^{-0.080} N_{Pe}^{-0.65} N_A^{0.052} + 0.55 A_S N_R^{1.8} N_A^{0.15} + 0.2 N_G^{1.1} N_R^{-0.10} N_A^{0.053} N_{Pe}^{0.053} \right]$
NG	Nelson and Ginn 2011 (Nelson and Ginn 2011)	$\eta_{0,\gamma} = \gamma^2 \left[2.4 A_S^{1/3} \left(\frac{N_{Pe}}{N_{Pe}+16} \right)^{0.75} N_{Pe}^{-0.68} N_{Lo}^{0.015} N_{Gi}^{0.8} + A_S N_{Lo}^{1/8} N_R^{15/8} + 0.7 N_G N_R^{-0.05} \left(\frac{N_{Gi}}{N_{Gi}+0.9} \right) \right]$
MHJ	Ma et al. 2013 (Ma, et al. 2013)	$\eta_{0,\gamma} = \gamma^2 \left[\frac{8 + 4(1-\gamma) A_S^{1/3} N_{Pe}^{1/3}}{8 + (1-\gamma) N_{Pe}^{0.97}} N_{Lo}^{0.015} N_{Gi}^{0.8} N_R^{0.028} + A_S N_{Lo}^{15/8} N_R^{1/8} + 0.7 N_R^{-0.05} N_G \left(\frac{N_{Gi}}{N_{Gi}+0.9} \right) \right]$

Table 1-4: Summary of the dimensionless parameters governing filtration: U is the approach velocity, a_c is the collector radius, D is the diffusion coefficient, μ is the water dynamic viscosity, a_p is the particle radius, ρ_p is the particle density, ρ_f is the fluid density, g is the gravity acceleration vector, A is the Hamaker constant, k is the Boltzmann constant, T is the absolute temperature, n is the porosity; [Adapted from (Tufenkji and Elimelech 2004)].

Dimensionless parameter	Definition	Physical interpretation
N_R	$\frac{a_p}{a_c}$	Steric number or Aspect ratio
N_{Pe}	$\frac{2Ua_c}{D}$	Peclet number It characterize the ratio between convective and diffusive transport
N_G	$\frac{2a_p^2(\rho_c-\rho_f)g}{9\mu U}$	Gravity number It is defined as the ratio of Stokes particle settling velocity to approach velocity of the fluid
N_{Gi}	$\frac{1}{1+N_G}$	-
N_A	$\frac{A}{12\pi\mu a_p^2 U}$	Attraction number It represents combined influence of van der Waals attraction forces and fluid velocity on particle deposition rate due to interception
N_{Lo}	$\frac{A}{9\pi\mu a_p^2 U}$	London group (variation of the Attraction number)
N_{VdW}	$\frac{A}{k_B T}$	Van der Waals number It characterizes the ratio of van der Waals interaction energy to the particle's thermal energy
A_s	$\frac{1(1-\gamma^5)}{2-3\gamma+3\gamma^5-2\gamma^6}$	Porosity dependent variable
γ	$(1-n)^{1/3}$	Porosity dependent variable

The original Yao et al. model was independent from porosity since it was derived for a sphere in an infinite domain ($n \to 1$). Yao et al. (Yao, et al. 1971) reported a correction for the diffusive term by introducing the porosity dependent coefficient $A_S^{1/3}$ (defined in Table 1-4). This coefficient was derived by Pfeffer (Pfeffer 1964) and it accounts for the effect of porosity on particle deposition. Also the interception term was corrected by A_S leading to the following equation (Elimelech 1995):

$$\eta_{0\_As\_Yao} = 4.04 N_{Pe}^{-2/3} A_S^{1/3} + \frac{3}{2} N_R^2 A_S + N_G$$

Eq. 1-39

Rajagopalan and Tien (Rajagopalan and Tien 1976) used a Lagrangian approach (i.e., particle trajectory analysis) in the Happel's model to derive interception and gravity removal efficiencies considering also the hydrodynamic retardation and the van der Waals force, while Brownian diffusion was treated separately by adding the Yao et al. term. Their correlation equation was then refined by Logan et al. (Logan, et al. 1995), who

made it consistent with the efficiency definition valid for the Happel's model, defined in Eq. 1-40 and named, in this work of thesis, $\eta_{0,\gamma}$. Thus Rajagopalan and Tien's corrected equation (Rajagopalan and Tien 1976) became the one reported in Table 1-3.

$$\eta_{0,\gamma} = \frac{I_S}{UC_0\left(\pi b^2\right)} = \gamma^2 \frac{I_S}{UC_0\left(\pi a_c^2\right)} = \gamma^2 \eta_0$$

Eq. 1-40

$\eta_{0,\gamma}$ normalizes the particle deposition flux, I_s, with the advective flux of particles coming from the projection of the full fluid envelope of the Happel's model and not only from the collector projection (a schematic representation is available in Figure 1-11). γ^2 permits to switch from η_0 to $\eta_{0,\gamma}$ (Eq. 1-40).

η and η_γ can be considered instead of η_0 and $\eta_{0,\gamma}$ in Eq. 1-37 and Eq. 1-40, if also the electric double layer effect is considered.

Tufenkji and Elimelech (Tufenkji and Elimelech 2004) developed a closed-form solution for calculating colloid deposition efficiency on a solid grain using an Eulerian approach in the Happel's model. They accounted for the superposition of the effects of hydrodynamic forces, Van der Waals interactions, Brownian diffusion and gravity effects, and proposed the correlation equation reported in Table 1-3.

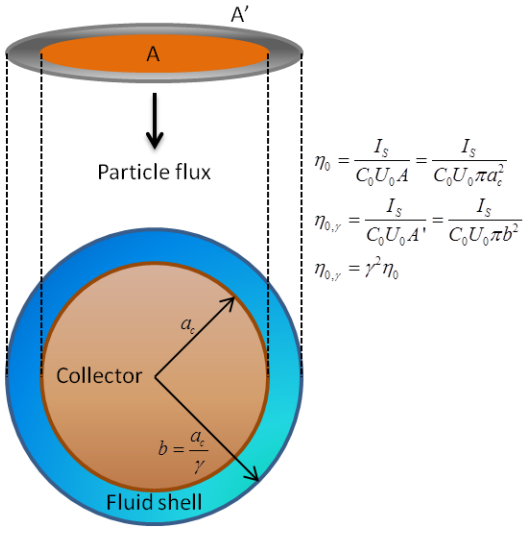

Figure 1-11: Schematic representation of the Happel's sphere in cell model and a visualization of the difference between the two definitions of the single collector contact efficiency.

The Lagrangian approach was successful applied in recent years for a deeper understanding of colloid retention processes. Nelson and Ginn (Nelson and Ginn 2005) applied a Lagrangian trajectory analysis in the Happel's

sphere-in-cell geometry with Stokes flow by using the concept of limiting trajectory and by considering only deterministic forces, while the stochastic Brownian force was added in a second step. Their results are in good agreement with the deterministic trajectory analysis of Rajagopalan and Tien (Rajagopalan and Tien 1976) when diffusion is neglected and in excellent agreement with the Levich solution (Levich 1962) for convection-diffusion when external forces and interception are neglected. Conversely, they found that the interaction of Brownian diffusion with sedimentation and interception have a significant effect on η_0, thus suggesting that the original assumption of additive rule on η_0 does not hold. This conclusion is consistent with the results of Tufenkji and Elimelech (Tufenkji and Elimelech 2004) for the large particles, while for submicrometer particles unexpected discrepancies are found.

The Lagrangian approach was also applied by several other authors to elucidate the role of grain-to-grain contacts in particle retention. Cushing and Lawler (Cushing and Lawler 1998) used a regular packing of spheres to investigate the mutual influence of multiple collectors and showed that contact points play a relevant role in particle retention due to complex hydrodynamic processes which funnel particles toward them, where particles are stably retained. This model, however, is less sensitive to particles size than experimental data, and to the influence of surface chemical properties, likely due to the predominance of hydrodynamic processes at grain-to-grain contacts.

Johnson et al. (Johnson, et al. 2007) further elucidated the role of grain-to grain contacts by means of a three-dimensional particle tracking that predicts colloid retention in porous media in the presence of an energy barrier via two mechanisms, namely wedging of colloids within grain to grain contacts, and retention of colloids (without attachment) in flow stagnation zones. Both wedging and retention in flow stagnation zones were sensitive to colloid surface interaction forces (energy barrier height and secondary energy minimum depth). The model provides a mechanistic basis for colloid retention in the presence of an energy barrier via processes that were recently hypothesized to explain experimental observations.

Ma et al. (Ma, et al. 2009) developed a full Lagrangian approach. All physical (drag, gravity, Brownian motion) and chemical (DLVO) forces were used for particle trajectory analysis in the hemisphere-in-cell model geometry. The flow field was solved numerically via CFD. This choice is justified by the goal of predicting colloid deposition in the presence of energy barriers, which has been shown in previous literature to involve deposition within grain to grain contacts for colloid to collector ratios greater than approximately 0.005. A correlation equation for predicting collector efficiencies in the hemispheres-in-cell model in the absence of energy barriers was developed via regression of numerical results to dimensionless parameters (see Table 1-3).

In 2010 Wei and Wu (Wei and Wu 2010) developed a new trajectory simulation algorithm to describe the efficiency of a single collector (pore) to catch sub-micrometer particles moving through saturated porous media. A constricted-tube model incorporating the deterministic (interception, hydrodynamic retardation, Van der Waals force and gravitational sedimentation), stochastic (Brownian diffusion), and thermodynamic (electrostatic and steric repulsion force) mechanisms was established to predict nano-scale zerovalent iron particles transport and deposition by applying Lagrangian trajectory analytical approach. The simulation results show good agreement with the results predicted by existing energy-barrier-free models except for the particle size less than 100 nm at low approach velocity. The model successfully described the breakthrough curve of polymer modified nano-scale zerovalent iron in a bench top soil column as well. The novel simulation scheme can be a useful tool for predicting the behaviour of the nano-scale colloidal particles moving through filter beds or saturated soil columns under conditions with repulsion and attraction forces among surfaces.

Long and Hilpert (Long and Hilpert 2009) developed a correlation equation using Lattice Boltzmann simulations in a random packing of spheres neglecting both van der Waals force and hydrodynamic retardation. Recently Boccardo et al. (Boccardo, et al. 2014) solved the full Navier Stokes flow field exploiting an Eulerian approach proposing an extension of the correlation equation for higher Reynolds numbers.

As already pointed out by Song end Elimelech (Song and Elimelech 1992), Nelson and Ginn (Nelson and Ginn 2011) and Ma et al. (Ma, et al. 2013), the previous available models overestimate the rate of particle deposition in some particular conditions. For very small or very big particle dimensions and/or for very low approach velocities, the existing correlation equations predict single collector contact efficiency higher than one, which is physically questionable (Petosa, et al. 2010).

Song and Elimelech (Song and Elimelech 1992) analysed the Happel's-in-cell model and found out that the failure was in the transposition of the boundary conditions from the isolated sphere collector to the sphere-in-cell model: due to the different geometry the same boundary conditions are not correct in case of very small Peclet numbers (the commonly used boundary conditions for the Happel's model and the boundary conditions proposed by Song and Elimelech are reported in Annex I – Different boundary conditions for the Happel's model).

Nelson and Ginn (Nelson and Ginn 2011) proposed a normalized correlation equation (see Table 1-3), further refined two years later (Nelson, et al. 2013), explaining that values above unity are due to an overestimation of the contributions of diffusion (for small particles) and of sedimentation (for large particles).

Ma et al. (Ma, et al. 2013) proposed a normalized correlation equation (see Table 1-3) clarifying that, in case of Lagrangian simulations, the prediction of efficiency values greater than one are due to the correlation equations

themselves and not to mechanistic trajectory models. They also underlines that the existing correlation equations are valid only for Peclet number N_{Pe} between 70 and 10^4.

1.6 Filter bed efficiency

As firstly suggested by Payatake et al. (Payatake.Ac, et al. 1973), a filter/porous media can be viewed to be an assembly of particle collectors. It can be considered as a serie of randomly homogeneous portions, named unit bed elements (*UBE*), each of which, in turn, is composed of a number of collectors. Several geometrical configurations for the collectors present in a *UBE* are admitted (see paragraph 1.2); almost any model which adequately describes the flow field in a porous medium can be used. Nevertheless, the choice is limited by practical considerations that only relatively simple geometrical entities should be used. The capacity of a general unit (UBE_i) to remove particle particulate matters from the liquid stream flowing through it (with concentration *c*) can be characterized by its collection efficiency η (Tien and Payatakes 1979):

$$\frac{c_{1-i} - c_i}{c_{1-i}} = \eta$$

Eq. 1-41

Following the passages proposed by Johnson and Hilpert (Johnson and Hilpert 2013), the efficiency of the entire porous medium (view as a column of identical spherical collectors) can be written as:

$$\frac{C}{C_0} = (1-\eta)^{N_C}$$

Eq. 1-42

where N_c is the total number of *UBE* in series (the relationship between N_c and the total length *L* of the filter/porous media is related to the geometry of the unit collector), (see Figure 1-12).

Analogously, by looking at the porous medium (filter) as a continuum and by following the Yao's procedure (Yao 1968), we can state that the performance of a packed bed, in case of spherical grains, is related to the efficiency of a single collector by:

$$\frac{C}{C_0} = \exp\left[-\frac{3}{4}\frac{(1-n)}{a_c}\eta L\right]$$

Eq. 1-43

C and C_0 are the influent and effluent particle concentration, *n* is the bed porosity, *L* is the bed length and the other parameters have already been defined, see Figure 1-13 (if the efficiency definition of Eq. 1-40 needs to be used in Eq. 1-43, the argument of the exponent has to be divided by the porosity *n*).

Eq. 1-42 and Eq. 1-43 permit to upscale the results from the microscale, which is the point of view of this thesis, to the macroscale, which is the scale considered to project real remediation activities and field interventions. This scale-up approach implies the independence of colloid retention in the history of transport in preceding collectors (Johnson and Hilpert 2013), in other words it is assumed that each collector acts as all the others, independently on reciprocal position.

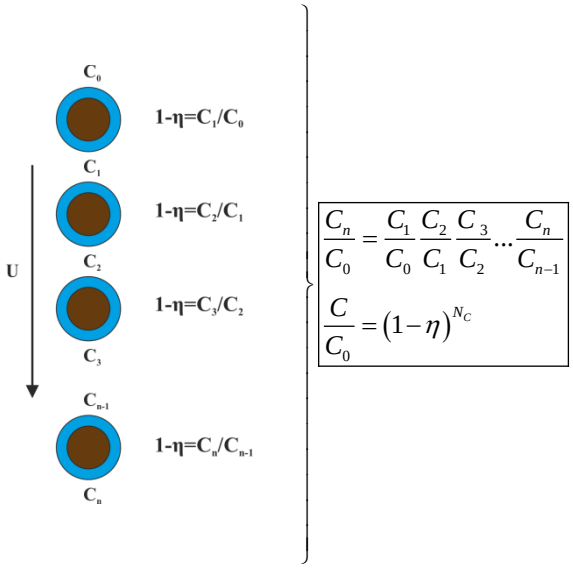

Figure 1-12: Upscaling method from unit cell to macroscale [adapted from (Johnson and Hilpert 2013)].

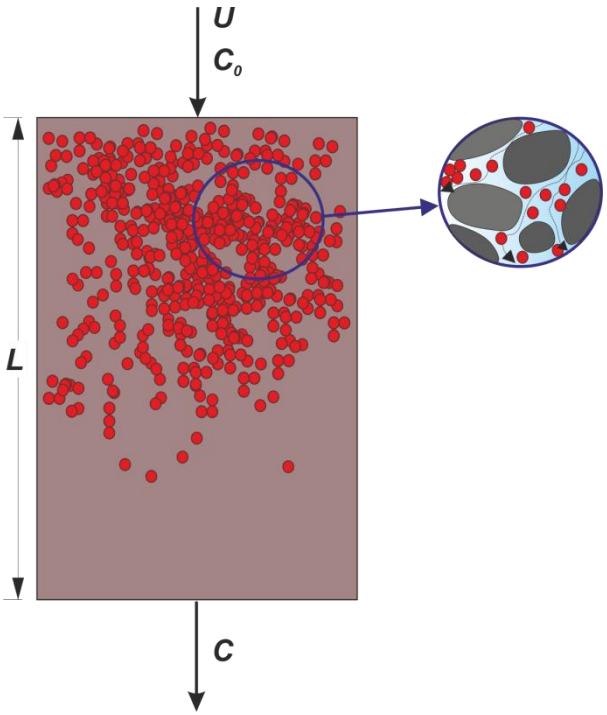

Figure 1-13:Schematic representation of fixed bed granular filtration [adapted from (Tien 1989)].

2 Chapter 2 – An extended and total flux normalized correlation equation for predicting single-collector efficiency

This chapter is based on the manuscript *An extended and total flux normalized correlation equation for predicting single-collector efficiency* by Messina F., Marchisio D.L. and Sethi R, Journal of Colloid and Interface Science (2015).

2.1 Introductions and Objectives

The importance of the single collector contact efficiency concept has been already explained in the previous chapter. In literature several correlation equations already exist to predict it. However, most of them, as explained by Ma et al. (Ma, et al. 2013), are valid only in a specific range of Peclet number ($70 < N_{Pe} < 10^4$), and predict efficiency values greater than one under some particular conditions, which is physically questionable (Petosa, et al. 2010).

Moreover these models were derived by using the additivity concept and it is important to remind here that the additivity is clearly a simplification hypothesis, as the different mechanisms, which are inherently non-linear, operate jointly and, therefore, neglecting their interactions may lead to large errors.

The aim of this study is, hence, the development of a novel correlation that overcomes the two main limitations described above, namely the simplification assumption of additivity and the overestimation of the collector efficiency (i.e., greater than one) for low approach velocities. This is accomplished by exploiting a hybrid Eulerian-Lagrangian approach for the solution of the colloidal transport problem around a single sphere, by properly accounting for the fact that the different mechanisms operate jointly and interact, and by correctly normalizing the deposition rate with the actual total particle flux entering a control volume. This latter feature ensures efficiency values lower than one, over a broad range of parameters.

2.2 Governing equations and numerical simulations

2.2.1 Geometry

Flow and colloidal transport simulations were performed using the finite-elements software COMSOL Multyphisics®. The geometry studied by Yao et al. (Yao, et al. 1971) was recreated in two dimensions under the assumption of axial symmetry, placing a single spherical collector characterized by a radius a_c in a cylindrical domain 15 times wider and 30 times longer than the collector itself (Figure 2-1), in order to minimize the influence of the boundary conditions. a_c was set equal to 250 μm.

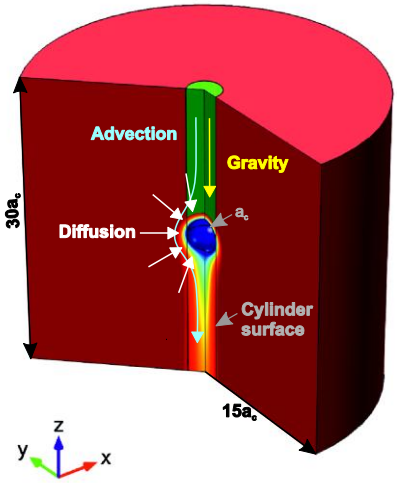

Figure 2-1: Geometry characteristics of the domain and directions of the main fluxes.

2.2.2 Mesh

Meshing was performed using triangular elements with the exception of the boundary layer close to the collector surface, where a mesh refinement with quadrilateral elements was adopted (Figure 2-2). A total number of 249186 elements was used ranging from 10^{-8} to 10^{-5} m; further information on the quality of the mesh is available in Table 2-1.

The thickness and the number of mesh layers close to the collector surface was chosen considering the mass transfer boundary layer thickness δ_m. Since the simulations were performed under creeping flow conditions, the Reynolds number cannot be defined, but Eq. 2-1 was anyway used to have an estimation of the mass transfer boundary layer thickness. N_{Sc} is the Schmidt number, defined as $\mu/(\rho_f D)$.

$$\delta_m = \frac{4.91 \cdot 2a_c}{\sqrt{N_{\mathrm{Re}}}\sqrt[3]{N_{Sc}}}$$

Eq. 2-1

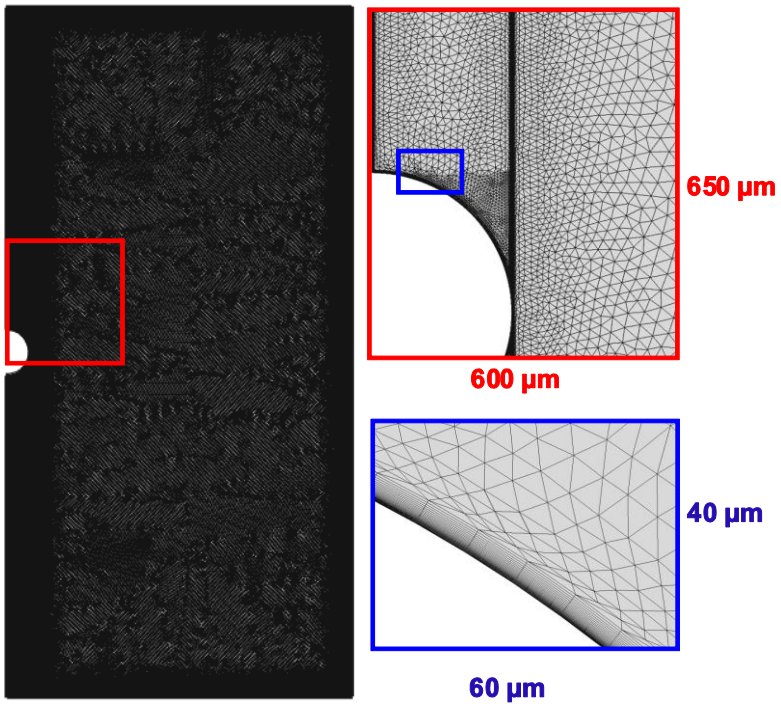

Figure 2-2: Mesh on the studied domain.

Table 2-1: Mesh information.

Number of triangular elements	127986
Number of quadrilateral elements* *40 layer around the spherical collector and the cylinder surface. The first layer is 10 nm thick, then they increase with a stretching factor of 1.1	121200
Edge elements	3110
Vertex elements	9
Total number of elements	249186
Minimum element quality	1.348e-9
Average element quality	0.4789
Mesh Area	2.803e-5 m^2
Maximun growth rate	12910.0
Average growth rate	12.02

2.2.3 Flow field

Stokes flow field was solved numerically imposing non-slip boundary conditions on the surface of the collector, vertical component of the velocity *U* at the inlet of the domain and zero pressure at the outlet of the domain. Symmetry boundary condition was used at the lateral side of the domain: this means no flow normal to this wall and vanishing of the shear stress.

2.2.4 Transport simulations

Point-particles can come into contact with the collector by three mechanisms of transport: advection (A), gravity (G) and Brownian diffusion (D). Interception, as explained in Chapter 1, is usually defined as the deposition of a particle which strikes the collector, due to its finite size, while moving along a streamline. This term is, therefore, related to the deposition of a finite-size particle in presence of advective transport only. In real systems steric size of the particles can influence deposition of particles transported by gravity (not just affecting the settling velocity), by Brownian motion (not just through change of diffusion coefficient) and by a combination of the transport mechanisms. Therefore in this study we prefer to refer to the steric effect (S) as the increases of deposition due to finite-size particles, in the presence of any other transport mechanism.

The additivity assumption was not considered in this study and different kind of simulations were performed considering (1) one only transport mechanism (advection (A), gravity (G) or Brownian diffusion (D)), (2) two transport mechanisms acting together and (3) all the three transport mechanisms active. These three cases are rapresented in Figure 2-3 where point particles deposition is shown in the right part of each figure and the effect of particle finite size is shown in the left part (steric effect) .

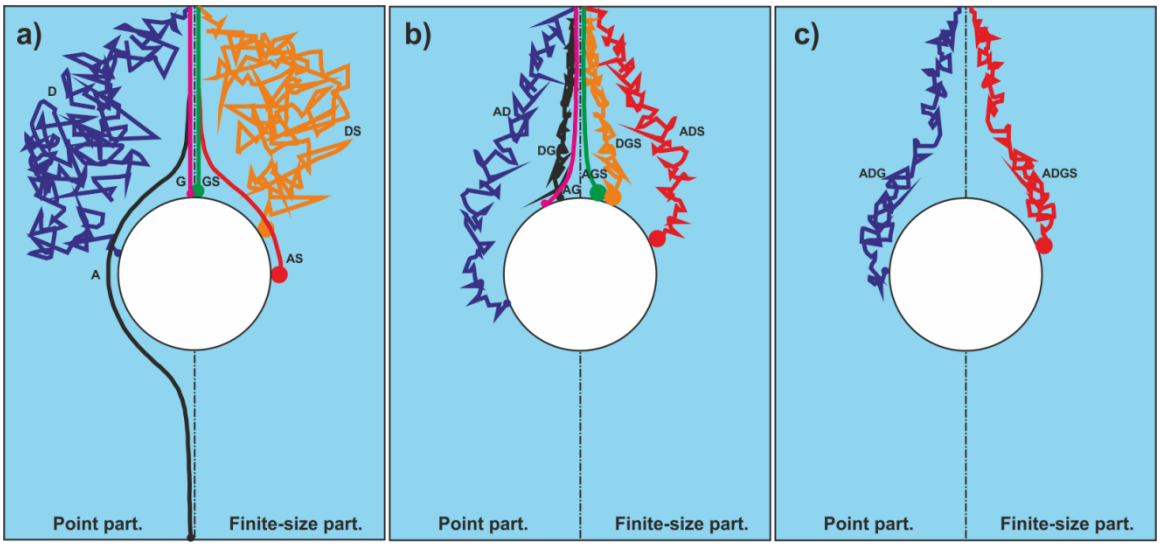

Figure 2-3: Main mechanisms of particles transport and deposition. (a) Single transport mechanism: diffusion D (blue line), advection A (black line), gravity G (magenta line), diffusion and steric effect DS (orange line), advection and steric effect AS (red line), gravity and steric effect GS (green line); (b) Two active transport mechanisms: diffusion and advection AD (blue line), gravity and diffusion DG (black line), advection and gravity AG (magenta line), diffusion-advection and steric effect ADS (red line), gravity-diffusion and steric effect DGS (orange line), advection-gravity and steric effect AGS (green line); (c) Three transport mechanisms acting together: advection-diffusion and gravity ADG (blue line), advection-diffusion-gravity and steric effect ADGS (red line).

A Lagrangian approach was used only for the null diffusion cases, which is virtually impossible to be simulated with the Eulerian approach, while most of transport simulations were performed in an Eulerian framework, thus numerically solving the advection diffusion equation reported in Eq. 2-2, where ***v*** is local fluid velocity, ***V*** is the velocity induced by the gravity force (Stokes or terminal velocity, defined in Table 2-2), *c* is the particle concentration and *D* is the diffusion coefficient of the suspended particle defined in Table 2-2.

$$\nabla \cdot \left(\mathbf{v}c + \mathbf{V}c \right) = \nabla \cdot \left(D \nabla c \right)$$

Eq. 2-2

Eq. 2-2 corresponds to Eq. 1-35 in steady state condition and considering only gravity as external force ***F*** $\left(\mathbf{V} = \frac{D\mathbf{F}_G}{k_B T} \right)$. Inlet concentration was set equal to C_0 and a perfect sink scenario was simulated placing an assigned $c=0$ concentration on the surface of the collector for point-particles (or at distance a_p from the surface of the sphere to account for steric effect associated with finite-size particles). In order to recreate the scenario proposed by Yao et al., the London van der Waals force and the hydrodynamic interactions between particles and the solid wall were neglected. This choice is coherent with the Smoluchowski–Levich approximation which assumes that hydrodynamic retardation experienced by the particle is balanced by the London Van der Waals forces between particles and collector (Adamczyk, et al. 1983; Elimelech 1995; Elimelech, et al. 1998; Tien C. 1989). This approximation holds true when particle dimension is less than the particle diffusion boundary layer (Boccardo, et al. 2014; Prieve and Ruckenstein 1974) (which is always in the micrometer range for the simulations performed).

2.2.5 Simulation setting

The simulations were performed over a wide range of variation of the non-dimensional parameters involved in the problem as reported in Table 2-2: the values were chosen with a logarithmic pattern. A total of 200 Lagrangian and 1320 Eulerian simulations were performed.

The performed simulations are represented by a point in a $\mathbb{R}^3$ space in Figure 2-4. Figure 2-4A shows the full set of simulations on a $\left(N_{Pe}, N_G, N_R \right)$ space (for $U \neq 0$) and Figure 2-4B reports the set of simulations on a $\left(D/(2a_c), V, N_R \right)$ space (for $U = 0$).

The simulations were performed using an Eulerian approach except for the cases characterized by null diffusion where a Lagrangian approach was used. Table 2-3 reports a comparison between the parameters used in the simulations and the typical range of variation in natural and engineering systems.

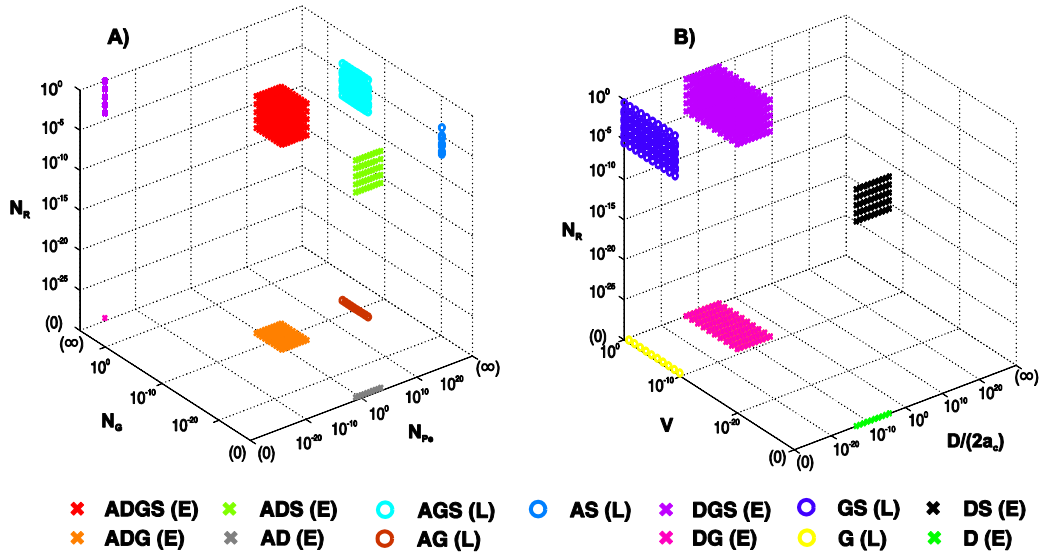

Figure 2-4: Representation of the numerical simulations performed: A) on a (N_{Pe}, N_G, N_R) space $(U \neq 0)$, B) on a $(D/(2a_c), V, N_R)$ space $(U = 0)$. (E) Eulerian simulations, (L) Lagrangian simulations.

Table 2-2: Range of variation of dimensional and non-dimensional parameters. *U* is the approach velocity (velocity far from the collector), *D* is the diffusion coefficient, *k* is the Boltzmann constant, *T* is the absolute temperature, μ is the water dynamic viscosity, a_p is the particle radius, *V* is the sedimentation velocity given by the Stokes low (Tien C. 1989), ρ_p is the particle density, ρ_f is the fluid density, *g* is the gravity acceleration vector and a_c is the collector radius.

	Parameters	Type of simulations	Values	# Values	Units
Advection	U	Eulerian	0; 10^{-5}	2	m/s
		Lagrangian	0; 10^{-5}	2	
Diffusion	$D = \frac{kT}{6\pi\mu a_p}$	Eulerian	$2.5\cdot10^{-17}$; $2.5\cdot10^{-16}$; $2.5\cdot10^{-15}$; $2.5\cdot10^{-14}$; $2.5\cdot10^{-13}$; $2.5\cdot10^{-12}$; $2.5\cdot10^{-11}$; $2.5\cdot10^{-10}$; $2.5\cdot10^{-9}$; $2.5\cdot10^{-8}$	10	m^2/s
		Lagrangian	0	1	
Gravity	$\mathbf{V} = \frac{2}{9}\frac{a_p^2(\rho_p - \rho_f)}{\mu}\mathbf{g}$	Eulerian	0; 10^{-9}; 10^{-8}; 10^{-7}; 10^{-6}; 10^{-5}; 10^{-4}; 10^{-3}; 10^{-2}; 10^{-1}; 1	11	m/s
		Lagrangian	0; 10^{-9}; 10^{-8}; 10^{-7}; 10^{-6}; 10^{-5}; 10^{-4}; 10^{-3}; 10^{-2}; 10^{-1}; 1	11	
Particle radius	a_p	Eulerian	0, 10^{-8}; 10^{-7}; 10^{-6}; 10^{-5}; 10^{-4}	6	m
		Lagrangian	0; $5\cdot10^{-9}$; 10^{-8}; $5\cdot10^{-8}$; 10^{-7}; $5\cdot10^{-7}$; 10^{-6}; $5\cdot10^{-6}$; 10^{-5}; 10^{-4}	10	
Peclet number	$N_{Pe} = \frac{2a_c U}{D}$	**Eulerian**	**0,10^{-1}; 1; 10^1; 10^2; 10^3; 10^4; 10^5; 10^6; 10^7; 10^8**	**10**	-
		Lagrangian	∞	**1**	
Gravity number	$N_G = \frac{V}{U}$	**Eulerian**	**0; 10^{-4}; 10^{-3}; 10^{-2}; 10^{-1}; 1; 10^1; 10^2; 10^3; 10^4; 10^5, ∞**	**12**	-
		Lagrangian	**0; 10^{-4}; 10^{-3}; 10^{-2}; 10^{-1}; 1; 10^1; 10^2; 10^3; 10^4; 10^5, ∞**	**12**	
Steric number or Aspect ratio	$N_R = \frac{a_p}{a_c}$	**Eulerian**	**0; $4\cdot10^{-5}$; $4\cdot10^{-4}$; $4\cdot10^{-3}$; $4\cdot10^{-2}$; $4\cdot10^{-1}$**	**6**	-
		Lagrangian	**0; $2\cdot10^{-5}$; $4\cdot10^{-5}$; $2\cdot10^{-4}$; $4\cdot10^{-4}$; $2\cdot10^{-3}$; $4\cdot10^{-3}$; $2\cdot10^{-2}$; $4\cdot10^{-2}$; $4\cdot10^{-1}$**	**10**	

Table 2-3: Minimum and maximum typical and simulated values of the main dimension and dimensionless parameters. *Eulerian simulations, **Lagrangian simulations, ( ) limit cases.

Parameter		Units of measurement	Typical values		Simulated values	
			Minimum value	Maximum value	Minimum value	Maximum value
a_p	Particle radius	m	$5.0 \cdot 10^{-9}$	$5.0 \cdot 10^{-5}$		
a_c	Collector radius	m	$5.0 \cdot 10^{-5}$	$5.0 \cdot 10^{-3}$	$2.5 \cdot 10^{-4}$	
U	Approach water velocity	m/s	$1.0 \cdot 10^{-7}$	$1.0 \cdot 10^{-3}$	0	$1.0 \cdot 10^{-5}$
ρ_p	Particle density	kg/m^3	998	$9.0 \cdot 10^{3}$		
T	Absolute temperature	K	278	323		
D	Diffusion coefficient	m^2/s	$4.1 \cdot 10^{-15}$	$4.7 \cdot 10^{-11}$	$2.5 \cdot 10^{-17*}$ 0^{**}	$2.5 \cdot 10^{-8}$
V	Stokes sed. velocity	m/s	0	$4.4 \cdot 10^{-2}$	0	$1.00 \cdot 10^{0}$
N_R	**Steric effect number**	-	**$1.0 \cdot 10^{-6}$**	**$1.00 \cdot 10^{0}$**	**$4.0 \cdot 10^{-5*}$ $2.0 \cdot 10^{-5}$ ** (0)**	**$4.0 \cdot 10^{-1}$**
N_G	**Gravity number**	-	**0**	**$4.4 \cdot 10^{5}$**	**0**	**$1.0 \cdot 10^{5}$ (∞)**
N_{Pe}	**Peclet number**	-	**$2.1 \cdot 10^{-1}$**	**$2.5 \cdot 10^{9}$**	**$2.0 \cdot 10^{-1}$ (0)**	**$2.0 \cdot 10^{8*}$ ∞^{**}**

2.3 *Result interpretation*

2.3.1 Normalized single collector contact efficiency definition

Previous studies determined the single collector contact efficiency η_0 as the ratio between the overall rate of particle collisions with the collector I_s, calculated integrating the particle flux over the entire surface of the sphere, and the advective particle flux entering the projected area of the collector (Eq. 1-37) (Tufenkji and Elimelech 2004; Yao, et al. 1971) or the collector plus the fluid envelope by introducing the correction factor γ^2 ($\eta_{0,\gamma}$ - Eq. 1-40) (Logan, et al. 1995).

In the framework of this study, we performed a mass balance over a cylindrical control volume tangent to the spherical collector (or with its radius incremented by a_p in case of finite-size particles to account for steric effect). We propose a *total flux normalized* single collector contact efficiency as the ratio between the rate of particle colliding with the collector I_s divided by the total rate of particles I_c entering by advection, gravity and diffusion into the cylindrical control volume (Eq. 2-3). The contribution of advection and gravity fluxes is predominant at the top of the cylindrical surface; conversely, diffusion is usually the dominant flux through the lateral wall of the cylinder (Figure 2-1).

$$\eta_N = \frac{I_s}{I_c}$$

Eq. 2-3

In this way the denominator of Eq. 2-3 is always greater than or equal to the one present in the definition of η_0 (Eq. 1-37). I_c is not only the advective flux coming from a limited part of the domain (as the projection of the collector), but it represents the total flux that could potentially deposit on the collector, thus it is always greater than or equal to I_s. In fact, I_c includes also *(i)* the effect of other transport mechanisms (gravity and diffusion) acting on the particles, *(ii)* lateral fluxes contributing to the movement of particles toward the collector and *(iii)* an increased area of the top projection of the sphere whose radius is increased by a_p to rigorously account for the finite size of the particles $\left(\pi\left(a_c + a_p\right)^2\right)$.

2.3.2 General formulation of the novel correlation equation

In the *total flux normalized* correlation equation the rate of particle collisions with the collector I_s and the total rate of particles entering into the cylinder I_c are expressed as a summation of seven terms (Eq. 2-4). As can be inferred from Eq. 2-5, each term is composed by the sum of two power functions: the first depends on the transport mechanisms (advection, gravity and Brownian diffusion), i.e. by their characteristic velocities $\left(U, V, D/\left(2a_c\right)\right)$, and the second depends also on the steric contribution induced by finite-size of the particles, thus N_R. Multiplication by the surface of the projection of the sphere $\left(\pi a_c^2\right)$ was performed in order to more easily compare the proposed model with the results of previous studies. The seven terms reported in Eq. 2-4 are therefore due to single and mutually interacting transport mechanisms and the steric effect:

- terms 1-3 depend on one transport mechanism (advection (A), gravity (G) or diffusion (D)) which acts alone, through its characteristic velocity (respectively $\left(U, V, D/\left(2a_c\right)\right)$), with or without steric contribution (S), through N_R;
- terms 4-6 depend on two combined transport mechanisms (AG, AD, DG) and therefore simultanously on two characteristic velocities and on steric contribution;
- term 7 depends on the mutual presence of the three combined mechanisms (ADG) and therefore on all the three caracteristic velocities and on steric contribution .

$\alpha_i, \beta_i, \gamma_i, k_{s1,i}$ and $k_{s2,i}$ are the exponents and the coefficients that need to be estimated by the fitting procedure.

For non-null advection, in order to compare the proposed correlation equation to previous formulations, it is possible to arbitrarily divide I_s and I_c by the denominator of η_0 definition (i.e., the advective rate passing through the top of the cylinder $\pi a_c^2 U C_0$, denominator of Eq. 1-37) obtaining Eq. 2-6. This equation depends on the non-dimensional numbers N_{Pe}, N_G and, of course, N_R. In this way, the numerator of the normalized efficiency (Eq. 2-6) can clearly be considered an extended formulation of Yao's η_0 (Eq. 2-7).

$$\eta_N = \frac{I_s}{I_c} = \frac{I_{s,1}^{A,S} + I_{s,2}^{G,S} + I_{s,3}^{D,S} + I_{s,4}^{AG,S} + I_{s,5}^{AD,S} + I_{s,6}^{DG,S} + I_{s,7}^{AGD,S}}{I_{c,1}^{A,S} + I_{c,2}^{G,S} + I_{c,3}^{D,S} + I_{c,4}^{AG,S} + I_{c,5}^{AD,S} + I_{c,6}^{DG,S} + I_{c,7}^{AGD,S}}$$

Eq. 2-4

$$I_s = \pi a_c^2 C_0 \sum_{i=i}^{7} U^{\alpha_i} V^{\beta_i} \left(\frac{D}{2a_c}\right)^{1-\alpha_i-\beta_i} \left(k_{s1,i} + k_{s2,i} N_R^{\gamma_i}\right)$$

$$I_c = \pi a_c^2 C_0 \sum_{i=i}^{7} U^{\alpha_i} V^{\beta_i} \left(\frac{D}{2a_c}\right)^{1-\alpha_i-\beta_i} \left(k_{c1,i} + k_{c2,i} N_R^{\gamma_i}\right)$$

Eq. 2-5

$$\eta_N = \left.\frac{I_s}{I_c}\right|_{U\neq 0} = \frac{\sum_{i=i}^{7} N_G^{\beta_i} N_{Pe}^{\alpha_i+\beta_i-1} \left(k_{s1i} + k_{s2i} N_R^{\gamma_i}\right)}{\sum_{i=i}^{7} N_G^{\beta_i} N_{Pe}^{\alpha_i+\beta_i-1} \left(k_{c1i} + k_{c2i} N_R^{\gamma_i}\right)} = \frac{\eta_0}{\sum_{i=i}^{7} N_G^{\beta_i} N_{Pe}^{\alpha_i+\beta_i-1} \left(k_{c1i} + k_{c2i} N_R^{\gamma_i}\right)}$$

Eq. 2-6

$$\eta_0 = \frac{I_s}{\pi a_c^2 U C_0} = \eta_0^A + \eta_0^{AS} + \eta_0^G + \eta_0^{GS} + \eta_0^D + \eta_0^{DS} + \eta_0^{AG} + \eta_0^{AGS} + \eta_0^{AD} + \eta_0^{ADS} + \eta_0^{DG} + \eta_0^{DGS} + \eta_0^{AGD} + \eta_0^{AGDS}$$

Eq. 2-7

2.3.3 Fitting of the results and parameter estimation

The fitting of the coefficients $\left(k_{s1,i}$ and $k_{s2,i}\right)$ and exponents $\left(\alpha_i, \beta_i$ and $\gamma_i\right)$ present in Eq. 2-5 was perfomed by simultaneously minimizing the residual between the CFD data of deposition $\hat{I}_s$, of the rate of particles entering the cilinder $\hat{I}_c$ and of the normalized efficiency $\hat{\eta}_N$ and their correspondent models (I_s, I_c, η_N, Eq. 2-4 and Eq. 2-5).

The parameter estimation was performed using a hierarchical procedure which begins from point-particles by determing the coefficients and exponents corresponding to only one transport mechanism, thus when two transport mechanisms are absent (first level in Figure 2-5). Subsequently, the procedure estimated the

coefficients and exponents for the case of two combined mechanisms acting together, therefore when at least one transport mechanism is absent (second level in Figure 2-5). Finally, the parameters of three combined transport mechanisms were determined (third level in Figure 2-5). The procedure was then repeated in order to estimate the coefficients for finite-size particles (considering steric effect). The procedure was therefore composed of 7x2 sub-tasks:

- First step (single transport mechanisms):
  - (1.a) A, (2.a) D, (3.a) G
  - (1.b) AS, (2.b) DS, (3.b) GS
- Second step (coupled transport mechanisms):
  - (4.a) AG, (5.a) AD, (6.a) DG
  - (4.b) AGS, (5.b) ADS, (6.b) DGS
- Third step (three transport mechanisms):
  - (7.a) ADG
  - (7.b) ADGS

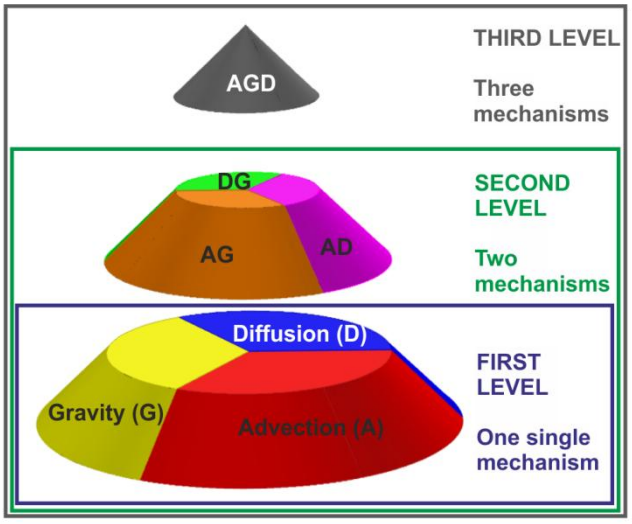

Figure 2-5: Schematic representation of the three step interpolation procedure. First level: single transport mechanisms; second level: coupled transport mechanisms; third level: advection, gravity and diffusion acting together.

For every sub task the weighted sum of the residual between the model (I_S, I_C, η_N) and the simulated data $(\hat{I}_S, \hat{I}_C, \hat{\eta}_N)$ of the flux on the sphere, of the flux through the cylinder and of the normalized efficiency was minimized according to Eq. 2-8.

$$R = min\left[\frac{1}{3}\sum\left(\log_{10}(I_s)-\log_{10}(\hat{I}_s)\right)^2+\frac{1}{3}\sum\left(\log_{10}(I_c)-\log_{10}(\hat{I}_c)\right)^2+\frac{1}{3}\sum\left(\log_{10}(\eta_N)-\log_{10}(\hat{\eta}_N)\right)^2\right]$$

Eq. 2-8

The simultaneous fitting of the rates and of the efficiency was adopted in order to improve and regularize the fitting procedure. The hierarchical procedure is necessary to guarantee the full independence of the fitting results when any of the transport mechanism is removed. On the opposite, a global fitting on all the data set (as those conducted in some of the previous studies) would have provided coefficients always indirectly dependent on the mutual presence of all the transport and steric effect mechanisms acting together (Nelson and Ginn 2005), thus biasing the results.

The results of each step of the fitting procedure are reported in Annex II - Fitting procedure steps.

2.4 *Novel normalized correlation equation to predict single collector contact efficiency*

The coefficients of the proposed correlation equation (reported in Table 2-4) were derived by applying the fitting procedure described in the previous paragraph to the data obtained from the CFD numerical simulations leading to Eq. 2-9 and Eq. 2-10, which are valid in case of non-null advection.

$$\eta_N = \eta_0 / \left[\left(1+6.0098N_R^{1.9834}\right)+N_G\left(1+6.0187N_R^{2}\right)+N_{Pe}^{-1}\left(7.5609+4.9534N_R^{1}\right)+N_G^{0.8741}\left(0.0442+0.1220N_R^{0.4210}\right)\right.$$
$$\left.+N_{Pe}^{-0.6338}\left(2.9352+2.7480N_R^{0.3737}\right)+N_G^{0.6550}N_{Pe}^{-0.3450}\left(2.7972+3.4372N_R^{0.6012}\right)+N_G^{0.5873}N_{Pe}^{-0.2565}\left(-1.1945-1.2616N_R^{0.5438}\right)\right]$$

Eq. 2-9

$$\eta_0 = 1.5062N_R^{1.9834}+N_G\left(1+6.0187N_R^{2}\right)+N_{Pe}^{-1}\left(7.5609+4.9534N_R^{1}\right)+N_G^{0.8741}\left(0.0442+0.1220N_R^{0.4210}\right)+$$
$$+N_{Pe}^{-0.6338}\left(2.9352+2.7480N_R^{0.3737}\right)+N_G^{0.6550}N_{Pe}^{-0.3450}\left(0.9461+1.1626N_R^{0.6012}\right)+N_G^{0.5873}N_{Pe}^{-0.2565}\left(-0.6740-0.7119N_R^{0.5438}\right)$$

Eq. 2-10

A calibration plot showing the excellent agreement between efficiency derived from numerical simulations and the correlation equation of η_N, over the wide and full set of data, is shown in Figure 2-6.

If the fitting procedure was interrupted at the end of the first step (only single transport mechanism with steric effect) or at the end of the second step (single and coupled transport mechanisms with steric effect), the final

total flux normalized equation would be less precise (these incomplete formulations of η_N and the corresponding calibration diagrams are reported in Annex III – Different η_N precision degrees).

In Figure 2-7 the proposed normalized correlation equation of η_N and the proposed η_0 are compared to numerical data obtained for typical values of engineering applications.

Table 2-4: Exponents and coefficients for Eq. 2-5 and Eq. 2-6. (*) Yao et al. values for the correspondent terms

Parameters			**Transport Mechanisms**						
			i=1	***i=2***	***i=3***	***i=4***	***i=5***	***i=6***	***i=7***
			Advection (A)	**Gravity (G)**	**Diffusion (D)**	**A - G**	**A - D**	**G - D**	**A - D - G**
Point-particles	**Exponents**	α_i	1 (*1)	0	0	0.1259	0.3662	0	0.1562
		β_i	0	1 (*1)	0	0.8741	0	0.6550	0.5873
		$1-\alpha_i-\beta_i$	0	0	1	0	0.6338 (*2/3)	0.3450	0.2565
	Coefficients	$k_{s1,i}$	0	1 (*1)	7.5609	0.0442	2.9352 (*4.04)	0.9461	-0.6740
		$k_{c1,i}$	1 (*1)	1	7.5609	0.0442	2.9352	2.7972	-1.1945
Steric effect for finite-size particles (S)	**Exponents**	γ_i	1.9834 (*2)	2	1	0.4210	0.3737	0.6012	0.5438
	Coefficients	$k_{s2,i}$	1.5062 (*3/2)	6.0187	4.9534	0.1220	2.7480	1.1626	-0.7119
		$k_{c2,i}$	6.0098	6.0187	4.9534	0.1220	2.7480	3.4372	-1.2616

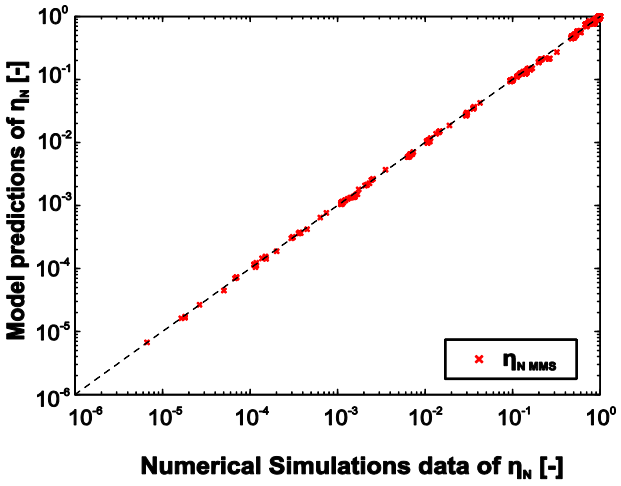

Figure 2-6: Calibration diagram of η_N .

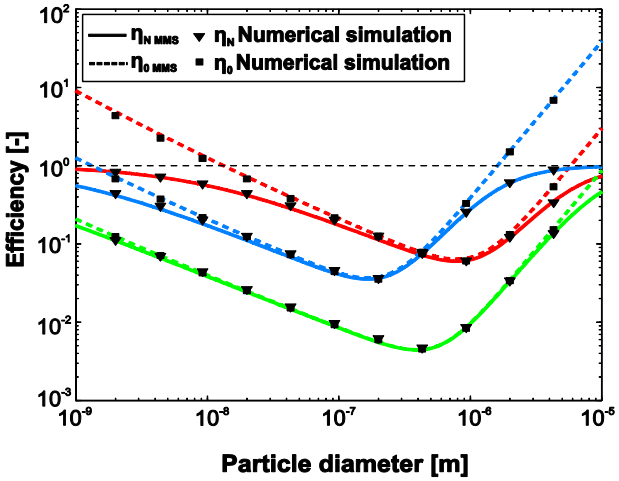

Figure 2-7: The proposed correlation equation of η_N (full line) and η_0 (dotted line) and some numerical simulation results (triangles for η_N and squares for η_0). Data: ρ_f =998 kg/m^3, T=288 K, μ =9.8·10^{-4} Pa·s, a_c=250 µm, U = 1·10^{-6} m/s (red lines), 1·10^{-5} m/s (blue lines), 1·10^{-4} m/s (green lines) and ρ_p = 1050 kg/m^3 (red lines), 7800 kg/m^3 (blue lines), 2500 kg/m^3 (green lines).

From the parameters listed in Table 2-4 the following considerations can be drawn:

- since $k_{s1}=0$, the advection contributes, coherently with previous models, to the rate of deposition on the collector only in presence of particle finite-size effect, i.e. when interception (advection associated with steric effect) is not negligible;

- the sum of the three exponents of the transport velocities is equal to one for every term coherently with dimensional analysis;

- the mixed terms account for mutual interaction among transport mechanisms including also the steric effect;

- the presence of other terms at the denominator of the expression for η_N allows normalization of the efficiency also when advection is not the dominant transport mechanism and in particular at high N_G and low N_{Pe} conditions. The value of η_N is less than or equal to one in all the simulated domain and also in limiting conditions (e.g., $U,V,D \to 0,\infty$);

- previous studies have argued that the three terms present in the model proposed by Yao et al. (Yao, et al. 1971) are due to the transport mechanisms of diffusion, gravity and interception. Analyzing the extended formulation of η_0 here proposed, it is possible to notice that the three terms introduced by Yao et al. and reported in the equation in Table 1-3, actually correspond to the

mechanisms of: advection and steric effect (interception) (*i=1*, η_0^{AS}, AS in Figure 2-3a), gravity (*i=2 with* $k_{s2}=0$, η_0^{G}, G in Figure 2-3a) and advection and diffusion (*i=5*, *with* $k_{s2}=0$, η_0^{AD}, AD in Figure 2-3b). As a matter of fact the term usually called η_D is actually due to the rate of attachment due to the mix processes of advection and diffusion divided by the advection rate passing through the projection of the sphere $\eta_0^{AD}=\frac{I_{s,5}^{AD}}{I_{c,1}^{A}}$. This conclusion agrees with the assumption adopted by Levich (Levich 1962) in deriving the total particle flux on a sphere at high N_{Pe} numbers (i.e., $N_{Pe}>70$), result later used by Yao for the calculation of the expression $N_{Pe}^{-2/3}$. The value of $k_{s1,5}$ derived in our expression is different from those proposed in previous studies due to the presence of a further term accounting only for diffusion as a transport mechanism $I_{s,3}^{D}$. The term η_G is $\eta_0^{G}=\frac{I_{s,2}^{G}}{I_{c,1}^{A}}$ and, therefore, is exactly the ratio between the rate of deposition due to the sole gravity and the advective rate through the top of the cylinder. Finally the interception term η_I is due to advection and steric effect and it is equal to $\eta_0^{AS}=\frac{I_{s,1}^{A,S}}{I_{c,1}^{A}}$;

- the novel correlation equation provides consistent results also for point particles (i.e. $N_R\to 0$);
- the total flux normalized equation provides values lower than one also for limiting conditions (Figure 2-9B).
- the formulation provides consistent results also when one or two transport mechanisms are absent (since some single or mixed terms are disappearing).

2.5 Comparison with existing models

A comparison with previous developed models and correlation equations was attempted in this section under two conditions:

- high porosities ($n\to 1$): this is the natural condition for the comparison of the different models since for porosities approaching to one they all produce a single collector in a pseudo-infinite domain (e.g., Yao's domain). In this case the normalizing flux (advective or total) is calculated over the projection of the collector $\left(\pi a_c^2\right)$;

- realistic porosities: in order to compare the models over a wide range of porosities and to normalize the efficiencies accounting for the fluxes entering the fluid enveloped $\left(\pi b^2\right)$, the porosity-dependent parameters γ and A_s were introduced in Eq. 2-9 and Eq. 2-10 leading to (for further information refer to Annex IV – Role of Porosity):

$$\eta_{N,\gamma} = \eta_{0,\gamma} / \left[\left(1 + A_S\, 6.0098 N_R^{1.9834}\right) + N_G \left(1 + 6.0187 N_R^2\right) + \gamma^2 N_{Pe}^{-1} \left(7.5609 + 4.9534 N_R^1\right) / (2 - 2\gamma) + \right.$$
$$+ A_S^{0.1259} N_G^{0.8741} \left(0.0442 + 0.1220 N_R^{0.4210}\right) + A_S^{0.3662} N_{Pe}^{-0.6338} \left(2.9352 + 2.7480 N_R^{0.3737}\right) +$$
$$\left. N_G^{0.6550} N_{Pe}^{-0.3450} \left(2.7972 + 3.4372 N_R^{0.6012}\right) + A_S^{0.1562} N_G^{0.5873} N_{Pe}^{-0.2565} \left(-1.1945 - 1.2616 N_R^{0.5438}\right) \right]$$

Eq. 2-11

$$\eta_{0,\gamma} = \gamma^2 \left[1.5062 A_S N_R^{1.9834} + N_G \left(1 + 6.0187 N_R^2\right) + N_{Pe}^{-1} \left(7.5609 + 4.9534 N_R^1\right) / (2 - 2\gamma) + \right.$$
$$+ A_S^{0.1259} N_G^{0.8741} \left(0.0442 + 0.1220 N_R^{0.4210}\right) + A_S^{0.3662} N_{Pe}^{-0.6338} \left(2.9352 + 2.7480 N_R^{0.3737}\right) +$$
$$\left. + N_G^{0.6550} N_{Pe}^{-0.3450} \left(0.9461 + 1.1626 N_R^{0.6012}\right) + A_S^{0.1562} N_G^{0.5873} N_{Pe}^{-0.2565} \left(-0.6740 - 0.7119 N_R^{0.5438}\right) \right]$$

Eq. 2-12

From the plots shown in Figure 2-9 (for the acronyms and formula see Table 1-3, MMS stayed for the proposed equations, (Messina, et al. 2015)), it is possible to state that the novel η_0 can be compared to the previous proposed equations normalized over the advective flux (namely Yao, TE, MPFJ), which provide efficiencies higher than one under low N_{Pe} and high N_G conditions both for unit and realistic porosities. Rajagopalan and Tien (Rajagopalan and Tien 1976) (RT) equation corrected by Logan et al. (Logan, et al. 1995) produces values different from the other equations at high porosity values. On the other side η_N generates values always lower than one over the all range of parameters. Under gravity dominating conditions it produces an asymptote which is equal to one for *n=1* and lower than one for realistic porosities accordingly with previous proposed models (NG and MHJ). For pure diffusion (low N_{Pe}) the proposed correlation tends asymptotically to one without showing any local maximum. This behaviour is different from those presented in previous models by NG and MHJ showing respectively values above unit (as stated in Nelson at al. (Nelson, et al. 2013)) and a local maximum at increasing N_{Pe} (see Figure 2-9 IIB). The absence of a local maximum in the MMS model can be explained by the presence of additional terms both at the numerator and at the denominator of the proposed formula, in particular by the presence of the pure diffusion term $I_{s,3}^D$ which is not present in previous proposed correlation equations. In Figure 2-8 the comparison between the proposed correlation equation and previous

models (both for unity and realistic porosity) is extended to very small particle sizes. The figure shows that both the numerical simulations and our model do not present any local maximum.

In Figure 2-10 further comparisons are presented including London Van der Waals force and hydrodynamic retardation mechanism in the previous correlation equations. The graphs in Figure 2-10 show that our correlation equation generates robust results over a wide range of parameters even if it was derived under the Smoluchowski-Levich approximation.

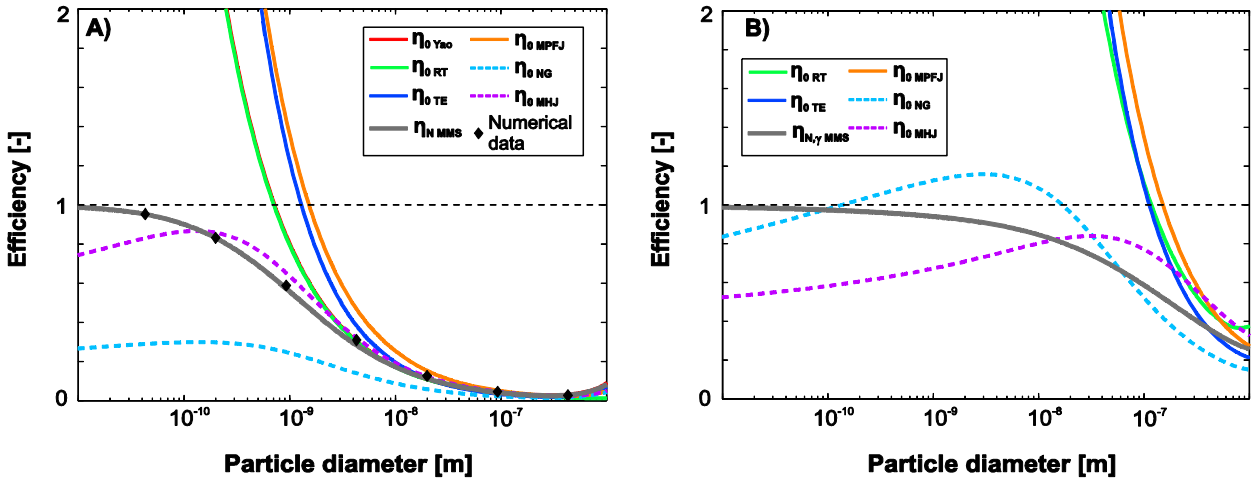

Figure 2-8: Comparison of the proposed η_N equation (Eq. 2-9 in A and Eq. 2-11 in B) with existing models for a range of very small particles. Parameter values: (A) Porosity n≈1, normalization over the collector projection, ρ_f = 998 kg/m^3, ρ_p = 2500 kg/m^3, T = 288 K, μ = 9.8·10^{-4} Pa·s, a_c =250 µm, U=1·10^{-5} m/s; (B) Porosity n = 0.25, normalization over the fluid envelope of radius b, ρ_f = 998 kg/m^3, ρ_p = 1050 kg/m^3, T = 288 K, μ = 9.8·10^{-4} Pa·s, a_c = 250 µm, U = 4.6·10^{-7} m/s.

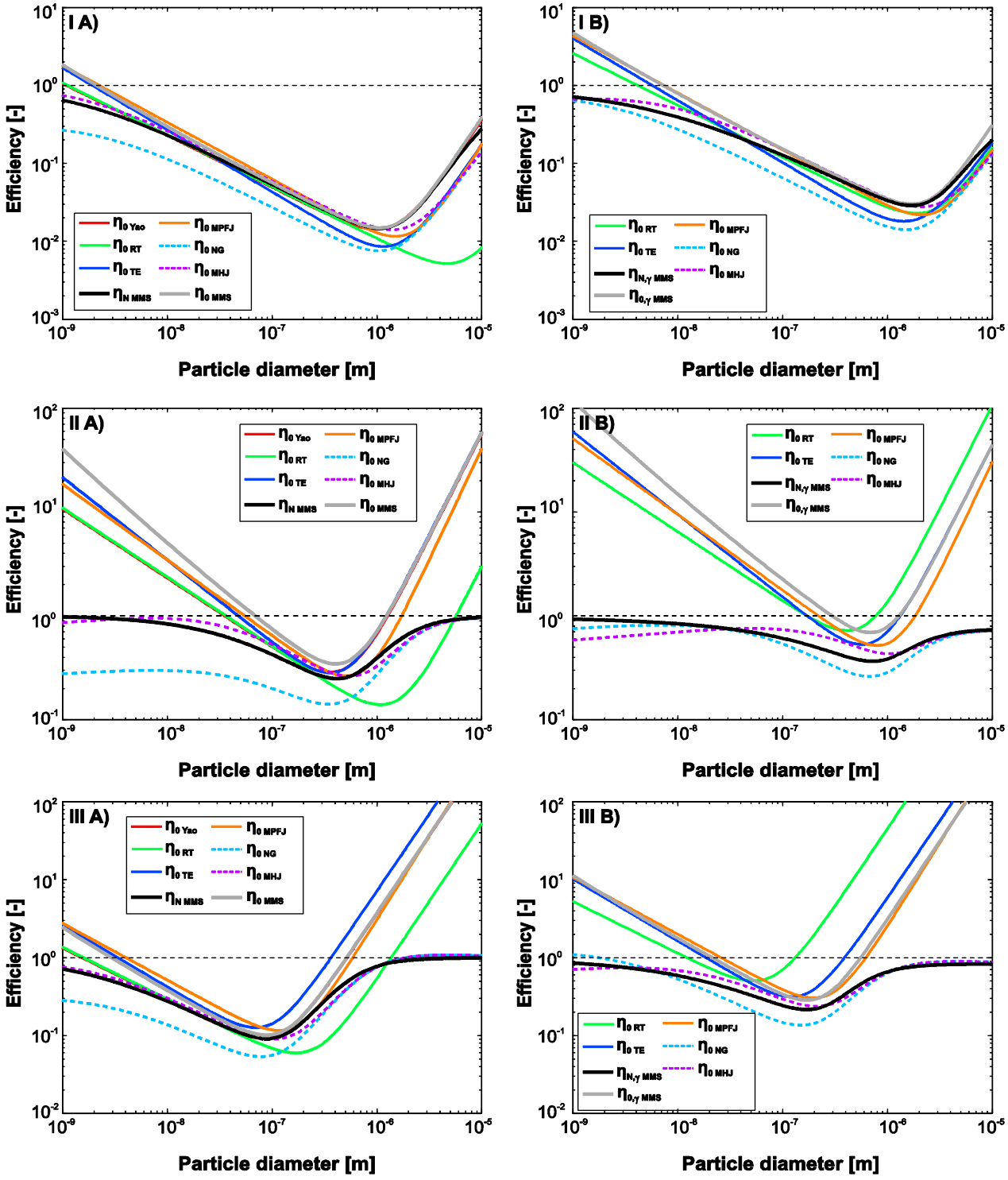

Figure 2-9: Comparison of the proposed η_N and η_0 equations with existing models. Van der Waals interactions were neglected. ρ_f = 998 kg/m^3, μ = 9.8·10^{-4} Pa·s. (A) Porosity n ≈ 1, normalization over the collector projection (Eq. 2-9 and Eq. 2-10); (B) Porosity n < 1, normalization over the fluid envelope of radius b (Eq. 2-11 and Eq. 2-12). (I) Case study from (Tufenkji and Elimelech 2004) (n = 0.39, a_c = 0.2 mm, U = 8·10^{-6} m/s, ρ_p = 1050 kg/m^3, T = 288 K); (II) Case study from (Nelson and Ginn 2011) (n = 0.35, a_c = 0.5 mm, U = 10^{-7} m/s, ρ_p = 1100 kg/m^3, T = 291 K); (II) Case study from (Ma, et al. 2013) (n = 0.25, a_c = 0.255 mm, U = 4.6·10^{-7} m/s, ρ_p = 4000 kg/m^3, T = 298.2K).

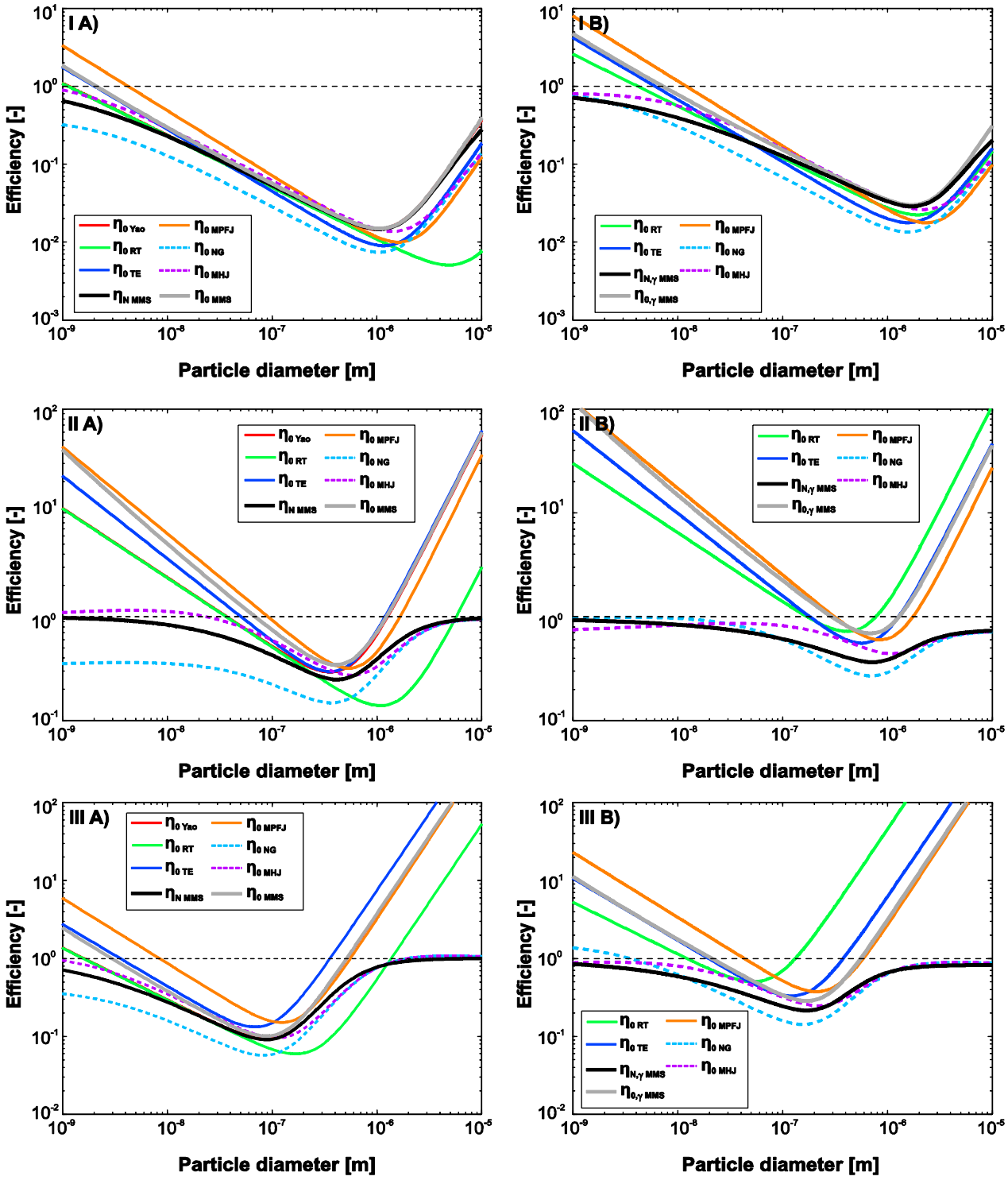

Figure 2-10: Comparison of the proposed η_N and η_0 equations with existing models. Van der Waals interactions were considered. ρ_f = 998 kg/m^3, μ = 9.8·10^{-4} Pa·s. (A) Porosity n ≈ 1, normalization over the collector projection (Eq. 2-9 and Eq. 2-10); (B) Porosity n < 1, normalization over the fluid envelope of radius b (Eq. 2-11 and Eq. 2-12). (I) Case study from (Tufenkji and Elimelech 2004) (n = 0.39, a_c = 0.2 mm, U = 8·10^{-6} m/s, ρ_p = 1050 kg/m^3, T = 288 K); (II) Case study from (Nelson and Ginn 2011) (n = 0.35, a_c = 0.5 mm, U = 10^{-7} m/s, ρ_p = 1100 kg/m^3, T = 291 K); (II) Case study from (Ma, et al. 2013) (n = 0.25, a_c = 0.255 mm, U = 4.6·10^{-7} m/s, ρ_p = 4000 kg/m^3, T = 298.2K).

2.6 Reduced models

Figure 2-11 shows the effect on the fitting residual when a single or a combination of mechanisms is removed from Eq. 2-9. The best fit of the numerical simulation is obtained, in a pseudo infinite domain, when all the mechanisms are acting with all the possible combinations leading to a residual of 0.23 (full η_N). As expected, the three terms included in Yao et al. (Yao, et al. 1971) model are the most important ones (advection term is obviously fundamental and present only at the denominator), but also the pure diffusion is a key term.

Several reduced models for the normalized correlation equation can be proposed by eliminating the less important terms in Eq. 2-9. In particular a reduced model providing a residual of 0.53 can be obtained including, both at the numerator and at the denominator, the mechanisms of A, G, AS, AD, D, DG, ADS (Eq. 2-13).

Furthermore, the extended expression of η_0 provides a residual of 0.38 if compared to numerical values derived from CFD simulations. Keeping only the terms present in the Yao's equation (A, G, AS, AD) leads to a residual of 36.09 that reduces to 5.09 if the same mechanisms reported above are included (i.e. A, G, AS, AD, D, DG, ADS) (Eq. 2-14). Further information is available in Annex V - Reduced models.

Moreover, Eq. 2-15 and Eq. 2-16 show the reduced models of η_N and η_0 including the porosity dependency. These two porosity dependent reduced models are consistent with the efficiency definition presented in Eq. 1-40, which normalizes the fluxes on the fluid envelope of the Happel's model.

It is important to note that both the full and reduced models, that we derived (a comparison is shown in Figure 2-12), include a term which accounts for pure diffusion, scaling with N_{Pe}^{-1}. This term is not present in the Yao et al. (Yao, et al. 1971) equation, but it is of pivotal importance in order to extend the correlation equation to low Peclet regime (i.e., $N_{Pe} < 70$). This conclusion is consistent with the study by Prieve and Ruckenstein (Prieve and Ruckenstein 1974) and by Ma et al. (Ma, et al. 2013).

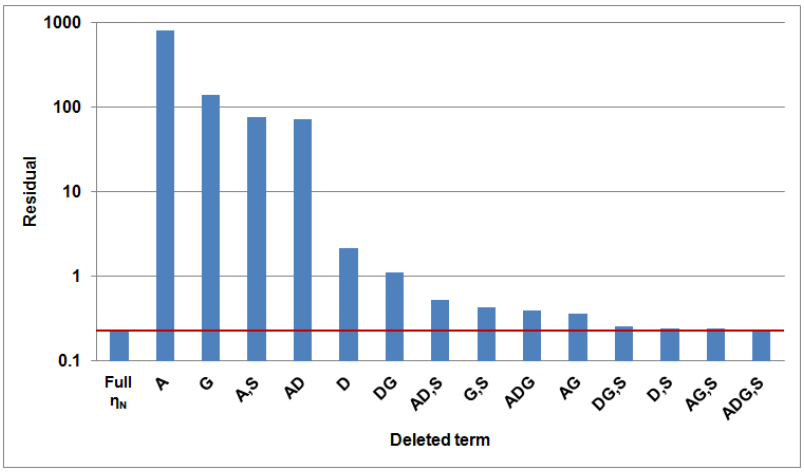

Figure 2-11: Residual of η_N neglecting the i^{th} term.

$$\eta_N^R = \frac{1.5062N_R^{1.9834} + 7.5609N_{Pe}^{-1} + N_G + 2.9352N_{Pe}^{-0.6338}\left(1+0.93621N_R^{0.3737}\right) + 0.9461N_G^{0.6550}N_{Pe}^{-0.3450}}{\left(1+6.0098N_R^{1.9834}\right) + 7.5609N_{Pe}^{-1} + N_G + 2.9352N_{Pe}^{-0.6338}\left(1+0.93621N_R^{0.3737}\right) + 2.7972N_G^{0.6550}N_{Pe}^{-0.3450}}$$

Eq. 2-13

$$\eta_0^R = 1.5062N_R^{1.9834} + 7.5609N_{Pe}^{-1} + N_G + 2.9352N_{Pe}^{-0.6338}\left(1+0.93621N_R^{0.3737}\right) + 0.9461N_G^{0.6550}N_{Pe}^{-0.3450}$$

Eq. 2-14

$$\eta_{N,\gamma}^R = \eta_{0,\gamma}^R \Big/ \Big[\left(1+6.0098A_S N_R^{1.9834}\right) + \gamma^2 7.5609N_{Pe}^{-1}/(2-2\gamma) + N_G + \\ + A_S^{0.3662}N_{Pe}^{-0.6338}\left(2.9352+2.7480N_R^{0.3737}\right) + 2.7972N_G^{0.6550}N_{Pe}^{-0.3450}\Big]$$

Eq. 2-15

$$\eta_{0,\gamma}^R = \gamma^2\left[1.5062A_S N_R^{1.9834} + 7.5609N_{Pe}^{-1}/(2-2\gamma) + N_G + A_S^{0.3662}N_{Pe}^{-0.6338}\left(2.9352+2.7480N_R^{0.3737}\right) + 0.9461N_G^{0.6550}N_{Pe}^{-0.3450}\right]$$

Eq. 2-16

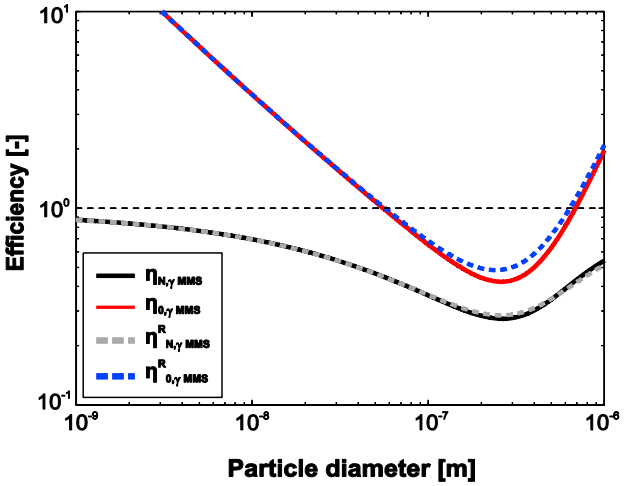

Figure 2-12: Comparison between the full equations of η_N and η_0 (Eq. 2-11 and Eq. 2-12) and the reduced equations (Eq. 2-15 and Eq. 2-16). Data: n=0.35, U=10^{-6}m/s, ρ_p =5500 kg/m^3, ρ_f =998 kg/m^3, T=288 K, μ =9.8·10^{-4} Pa·s and a_c =250 µm.

2.7 Conclusions

In this study a novel total flux normalized correlation equation (i.e., less than or equal to one in any conditions) for predicting single-collector efficiency was derived by means of a mass balance acting on a cylindrical domain including the collector. The proposed correlation equation is not derived by exploiting the additivity concept proposed by Yao et al. (Yao, et al. 1971), but includes also mixed terms accounting for the mutual interaction of concomitant transport mechanisms (i.e. advection, gravity and Brownian motion) and the steric effect. The correlation equation was extended in order to include porosity dependency and reduced forms were presented including the most relevant interacting mechanisms. In future studies the proposed approach will be further extended to more complex geometries and more particle-collector interactions.

3 Chapter 3 - Efficiency for an array of spheres

3.1 Introductions and Objectives

After the validation of the simulation method against the results presented in the previous chapter, the next step of this work investigates a more realistic geometry, which consists in an array of aligned collectors.

The aim of this second study was to investigate the collector efficiency of this simplified porous medium, composed by an array of five spheres. Moreover, the behaviour of each single collector was analysed to verify whether the efficiency varies from one collector to the others. This latter study is of particular importance since a constant collector efficiency along the porous medium is a common assumption in upscale methods.

3.2 Model setting

3.2.1 Geometry

The investigated geometry consists in a series of five spheres in column with a pre- and a post-mixing zone (Figure 3-1). In the following, the spheres will be named by a progressive number from one to five, starting from the top to the bottom.

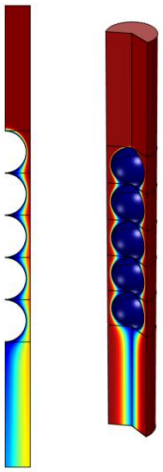

Figure 3-1: Investigated geometry, 2D and 3D: five spherical collectors in column.

The collector radius a_c was set equal to 250 µm and the separation distance between the spheres equal to 5 µm (which corresponds to 2/100 of the sphere radius). The width of the domain was imposed equal to $a_c(1-K)$, where K is an adjustable coefficient: by changing K it is possible to investigate different porosity values n:

$$n = \frac{\left(a_c(1-K)\right)^2\left(10a_c + 10a_c/100\right) - 5\frac{4}{3}a_c^3}{\left(a_c(1-K)\right)^2\left(10a_c + 10a_c/100\right)}$$

Eq. 3-1

The total high of the pre- and the post-mixing zones is equal to $3 \cdot a_c$ each. However, it is worth to mention that these two zones were not considered to evaluate the porosity.

3.2.2 Mesh

Meshing was performed using triangular elements, except for the boundary layer close to the collectors, where a mesh refinement with quadrilateral elements was adopted. The mass transfer boundary layer was calculated by using Eq. 2-1. Since the critical value was $2.37 \cdot 10^{-7}$ m, a mesh composed by 100 layers, each 10 nm thick, was imposed around the spheres. Further information about the mesh is available in Table 3-1.

Table 3-1: Mesh information (for *n* = 0.55).

Number of triangular elements	146586
Number of quadrilateral elements* *40 layer around the spherical collector and the cylinder surface. The first layer is 10 nm thick, then they increase with a stretching factor of 1.1	157000
Edge elements	6946
Vertex elements	31
Total number of elements	303586
Minimum element quality	0.007962
Average element quality	0.4564
Mesh Area	5.86e-5 m^2
Maximun growth rate	155.0
Average growth rate	1.363

3.2.3 Simulation setting

Two groups of simulations were performed. The first set, similarly to the previous chapter, considers one, two and then three transport mechanisms in sequence, but neglects the steric effect. A wide parameter range was investigated by a parametric sweep on *U*, *V*, *D* and *n*:

- 10 values for the diffusion coefficient *D* ranging between 10^{-17} and 10^{-8} m^2/s;
- 10 values of the gravity velocity *V* ranging between 10^{-14} and 10^{-4} m^2/s;
- 2 values of the fluid velocity *U*, namely: 0 and 10^{-6} m/s;
- 3 values of porosity *n* (see Table 3-2).

The second group of simulations was performed by considering also the steric effect and by investigating:

- 15 values of particles radius a_p in the range 1 nm to 1 μm;

- 5 values of particle density ρ_p (namely 998, 1050, 2500, 5000, 7800 kg/m^3);
- the 3 values of porosity reported in Table 3-2.

Particle radius and density are related to *V* and *D* by the definitions reported in

Table 2-2.

Table 3-2: Investigated range of porosity

K	Porosity
0.10	47%
0.15	51%
0.2	55%

Stokes equations were used to solve the fluid flow field: a constant approach velocity *U* was set as inlet boundary condition and a constant pressure equal to zero was set as outlet boundary condition. A no slip condition was set on the grains and symmetry (no normal flow and vanishing of the shear stress) was set at the lateral boundary. The transport was solved applying the same equations and boundary conditions discussed in the previous chapter.

3.3 Results

3.3.1 Variation of efficiency values along a column of spheres

The results of the second set of simulations (described in paragraph 3.2.3) were analysed to derive the efficiency of each collector of the array. The efficiency of each sphere was evaluated applying the definition reported in Eq. 1-41, thus by considering the concentration before and after each collector $\left(\eta_i = \left(c_{1-i} - c_i\right)/c_{1-i}\right)$.

It is evident from the results that, in case of no gravity effects ($\rho_p = \rho_f$ = 998 kg/m3, Figure 3-2), the efficiency of the individual spheres present a similar trend. The first sphere of the packing collects a little more compare to the following ones. However, the discrepancies are moderate and the collectors can be considered similar. The two graphs in Figure 3-2 correspond to two investigated porosity values: we can assert that porosity does not play a significant role.

Also for the simulations performed including the steric effect similar conclusions can be drown (Figure 3-3).

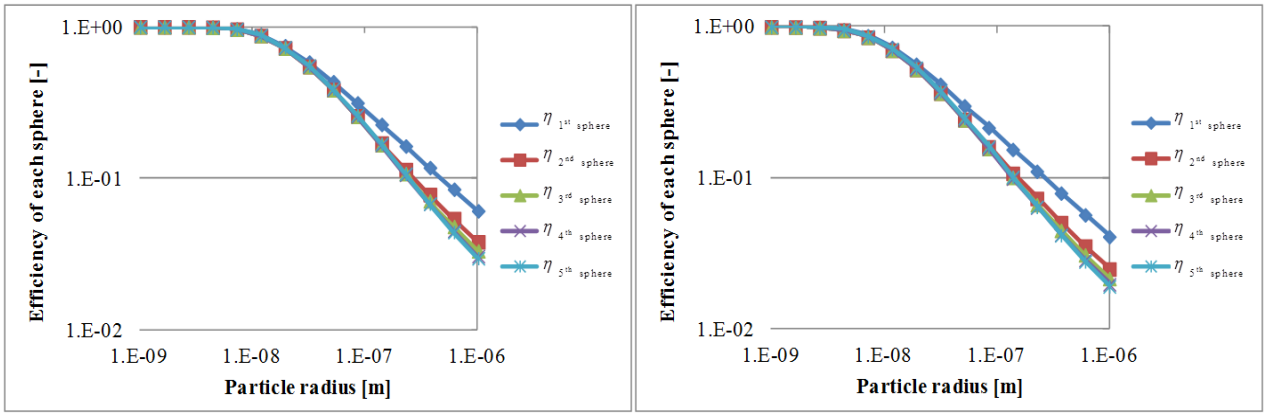

Figure 3-2: Collector efficiency η in case of advection and diffusion. Data: $U = 10^{-6}$ m/s, $a_c = 250$ µm, $T = 298$ K, $\rho_p = \rho_f = 998$ kg/m^3 and n (from left to right) = 0.46, 0.54.

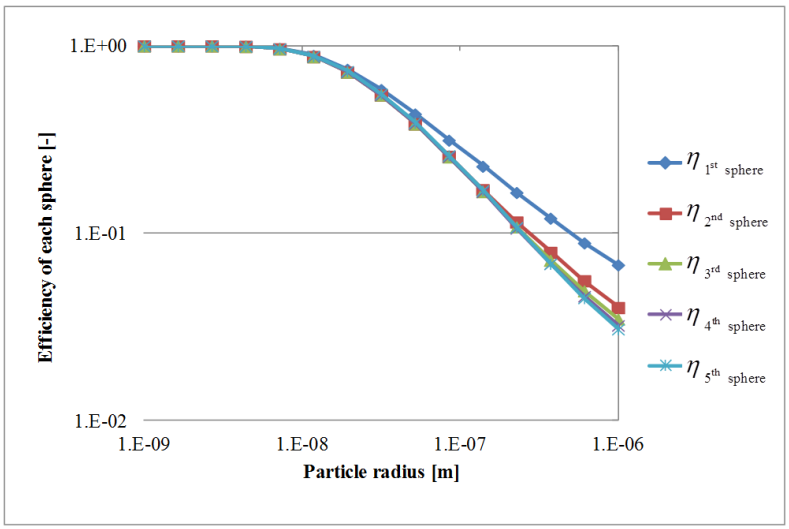

Figure 3-3: Collector efficiency η in case of advection, diffusion and steric effect. Data: $n = 0.46$, $U = 10^{-6}$ m/s, $a_c = 250$ µm, $T = 298$ K, $\rho_p = \rho_f = 998$ kg/m^3.

When gravity is introduced, the difference between the first sphere and the others becomes more evident (Figure 3-4): the results indicate that gravity plays a key role in the deposition onto the first sphere of the column, while it has a very minor effect on the others.

A very similar trend (Figure 3-5) was obtained also increasing the separation distance between the spheres, corresponding to an increased porosity ($n = 0.66$ and sphere separation distance equal to the collector radius a_c).

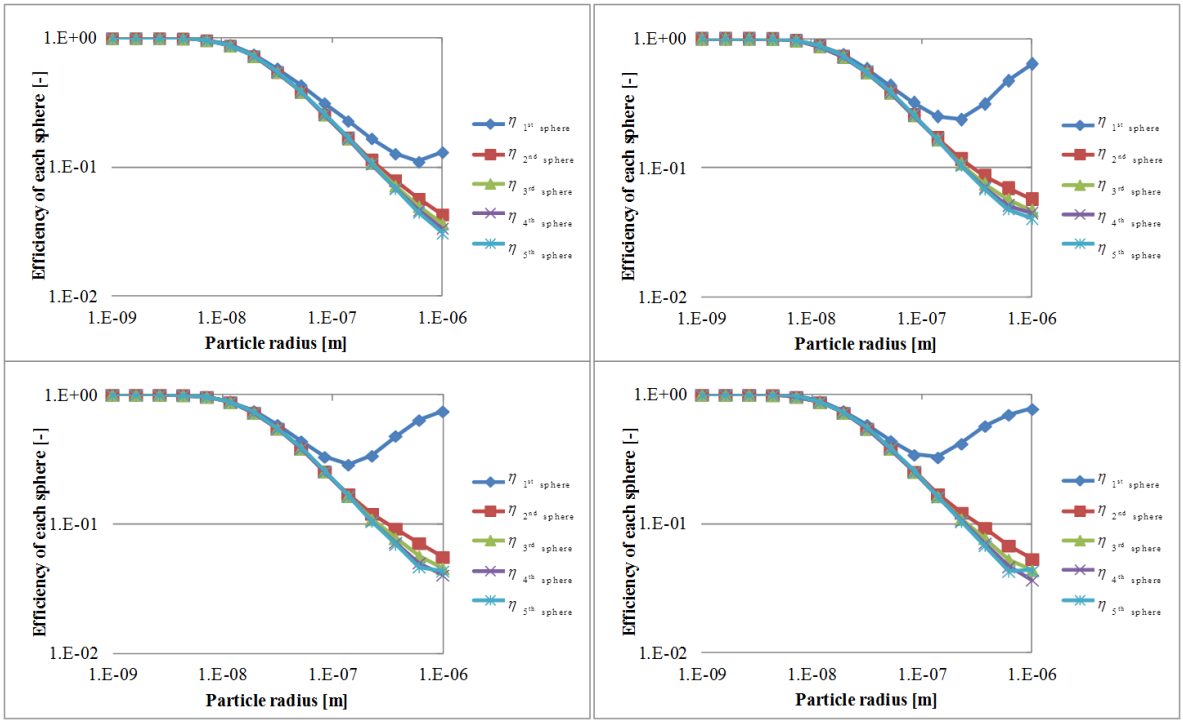

Figure 3-4: Collector efficiency η in case of advection, diffusion, gravity and steric effect. Data: n = 0.46, U = 10^{-6} m/s, a_c = 250 µm, T = 298 K, from (left to right and from top to bottom) ρ_p = 1050, 2500, 5000, 7800 kg/m^3.

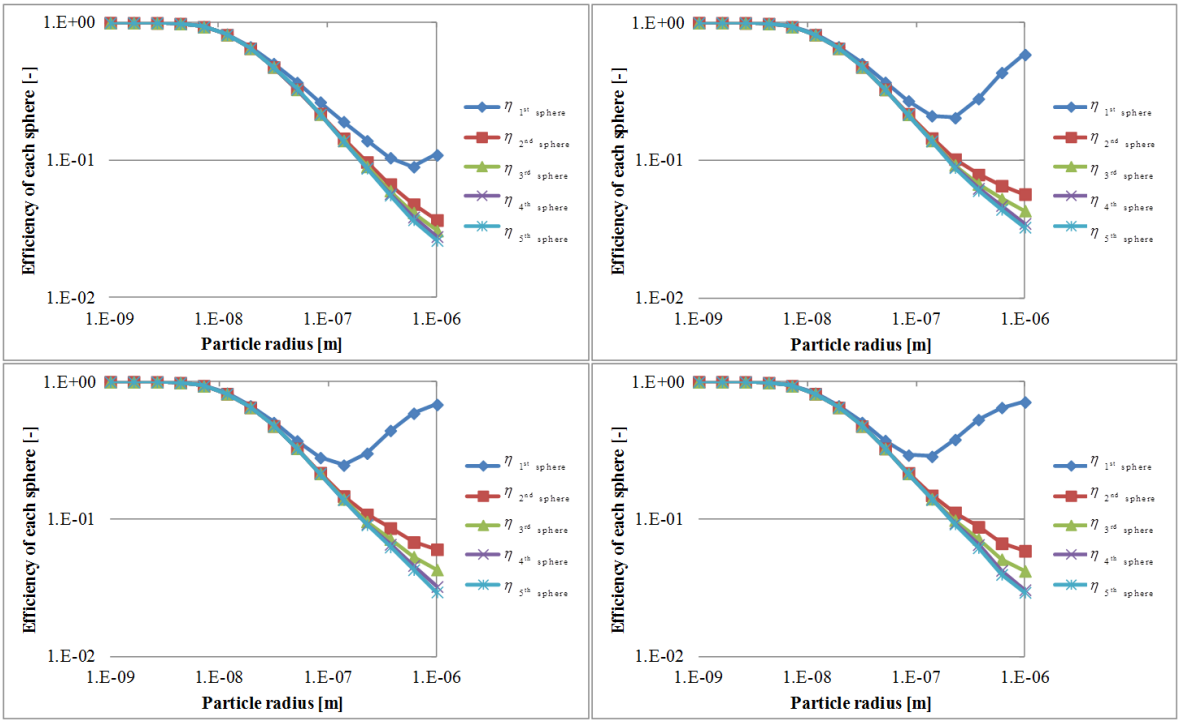

Figure 3-5: Collector efficiency η in case of advection, diffusion and gravity. Data: n = 0.66, U = 10^{-6} m/s, a_c = 250 µm, T = 298 K and (from left to right and from top to bottom) ρ_p = 1050, 2500, 5000, 7800 kg/m^3.

In conclusion, the results of the simulations indicate that the first collector of a column presents an efficiency higher than the others. The difference is emphasized with increasing the importance of gravity effect (that is, increasing the density contrast between particles and fluid and for larger particles) and cannot be neglected.

3.3.2 Upscaling methods

The bed filter efficiency proposed by Johnson and Hilpert (Johnson and Hilpert 2013) and reported in Eq. 1-42, was derived by assuming that the single collector efficiency of the first sphere is equal to all the others.

In this paragraph, the trends of the outlet normalized concentration C/C_0 obtained from the numerical simulations are compared with the values predicted by Eq. 1-42.

In the absence of gravity effects (Figure 3-6), the values predicted by Eq. 1-42 and the CFD results are in good agreement.

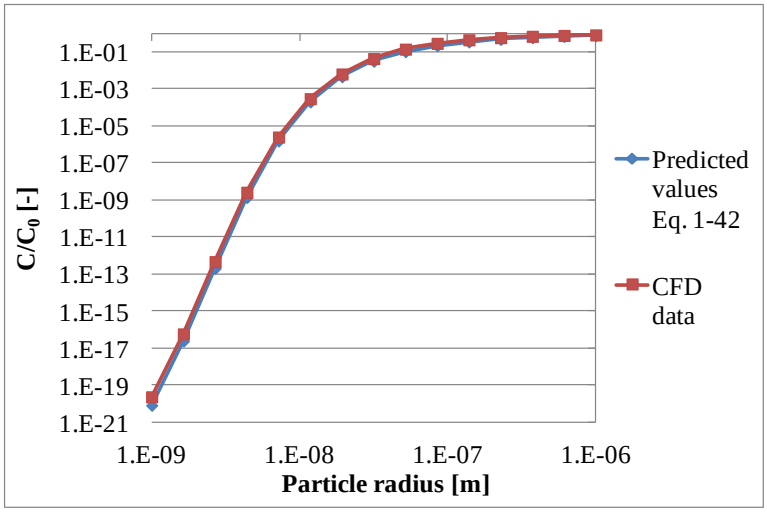

Figure 3-6: C/C_0 in case of advection and diffusion, in red the numerical data and in blue the values predicted by Eq. 1-42. Data: n = 0.50, U = 10^{-6} m/s, a_c = 250 µm, T = 298 K and ρ_p = 998 kg/m^3.

On the contrary, when gravity effects are relevant (large particles), the filter bed efficiency evaluated with Eq. 1-42 significantly deviates from the numerical results. The effluent concentration C, predicted by the model, underestimates the values obtained from the CFD simulations (Figure 3-7). The discrepancy is due to the fact that the first collector efficiency is significantly greater than those of the other spheres.

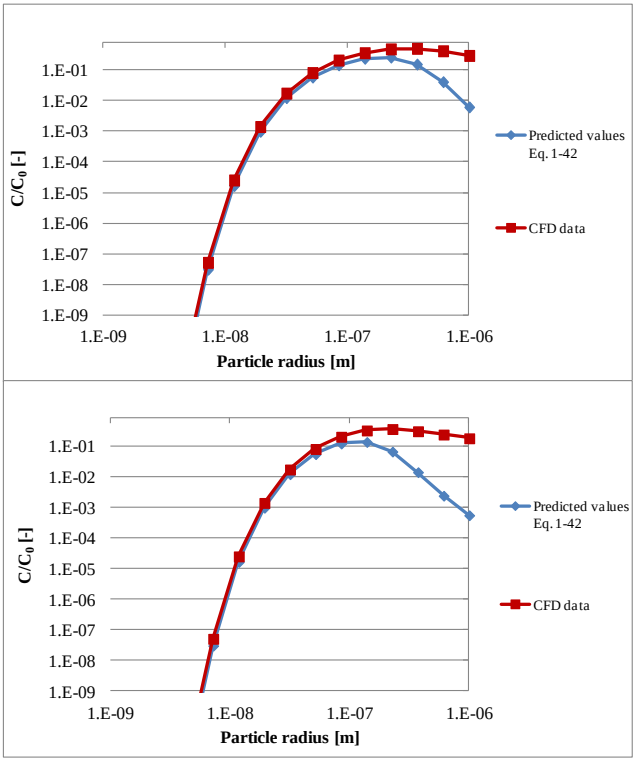

Figure 3-7: C/C_0 in case of advection, diffusion, gravity and steric effect, in red the numerical data and in blue the values predicted by Eq. 1-42. Data: n = 0.46, $U = 10^{-6}$ m/s, a_c = 250 µm, T = 298 K and (from top to bottom) ρ_p = 2500, 7800 kg/m^3.

3.3.3 A new equation for predicting bed filter efficiency

The CFD results discussed in the previous paragraph indicate that the efficiency changes among the spheres in a packed bed. As a consequence, under certain conditions, the change in concentration along the packed bed cannot be calculated assuming the collector efficiency of the single sphere, but the η_j of each collector is to be taken into account:

$$\frac{C}{C_0} = \prod_{j=1}^{N_c} (1-\eta_j)$$

Eq. 3-2

The simulations results also suggeste that, even if the efficiency of the first sphere is different, the η_j of the other collectors can be assumed constant. As a consequence, Eq. 3-2 can be simplified to:

$$\frac{C}{C_0} = (1-\eta)(1-\eta_M)^{(N_c-1)}$$

Eq. 3-3

where η is the efficiency of the first sphere (corresponding to the single collector efficiency as reported in the literature) and η_M is the efficiency representative of a sphere in the bulk of the porous medium.

Figure 3-8 reports the values of C/C_0 predicted by Eq. 1-42, those predicted by Eq. 3-3 and the CFD data. η_M was here calculated as the average efficiency on the spheres 2-5. It can be observed that Eq. 3-3 properly reproduces numerical results.

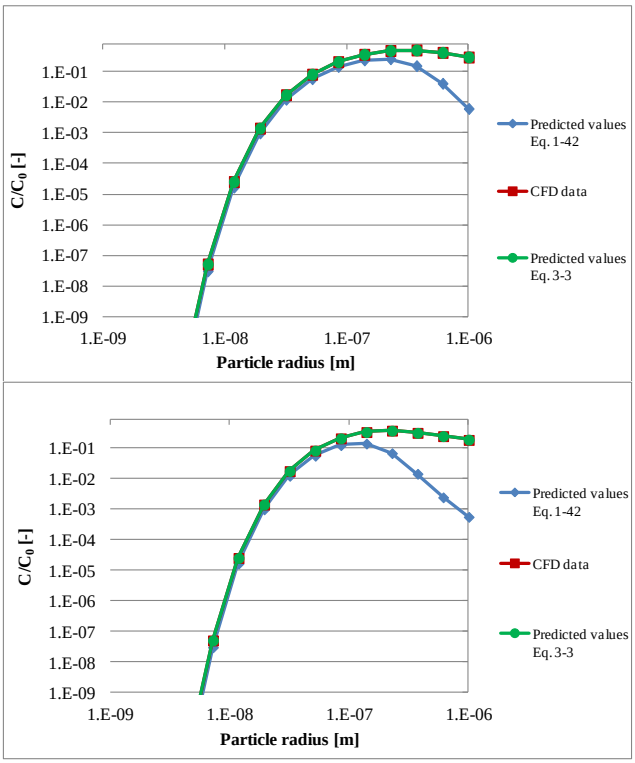

Figure 3-8: C/C_0 in case of advection, diffusion, gravity and steric effect, in red the numerical data, in blue the values predicted by Eq. 1-42 and in green the values predicted by Eq. 3-3. Data: n = 0.46, U = 10^{-6} m/s, a_c = 250 µm, T = 298 K, from top to bottom: ρ_p = 2500, 7800 kg/m^3.

3.3.4 Single collector contact efficiency correlation equations for spheres in a packing

The results of the previous paragraph highlight the need to use at least two different collector efficiencies to describe the total efficiency of a column of spheres: one, η, for the first collector and another one, η_M, representative of all the others.

Starting from the results of the first set of simulations (described in 3.2.3) and performing the same hierarchical fitting carried out in Chapter 0, a new correlation equation (Eq. 3-4) was derived to predict the efficiency of the

first sphere, in the absence of steric effect. The same structure used to derive $\eta_{0,\gamma}$ in Chapter 0 was adopted:

$$\eta = \gamma^2 \frac{\begin{array}{c} V + 0.0881(D/2a_c)/(1-\gamma) + 10.7100A_S^{0.2606}U^{0.2606}(D/2a_c)^{0.73941} + \\ 3\cdot 10^{-7} A_S^{0.4594}U^{0.4594}V^{0.5406} + 23.9249V^{0.4251}(D/2a_c)^{0.5749} - 0.0903A_S^{0.5147}U^{0.5147}V^{0.3675}(D/2a_c)^{0.1178} \end{array}}{\begin{array}{c} 0.8334U + 0.8334V + 0.0881(D/2a_c)\gamma^2/(1-\gamma) + 6.1226A_S^{0.2606}U^{0.2606}(D/2a_c)^{0.73941} - \\ 0.1225A_S^{0.4594}U^{0.4594}V^{0.5406} + 14.7590V^{0.4251}(D/2a_c)^{0.5749} + 0.2986A_S^{0.5147}U^{0.5147}V^{0.3675}(D/2a_c)^{0.1178} \end{array}}$$

Eq. 3-4

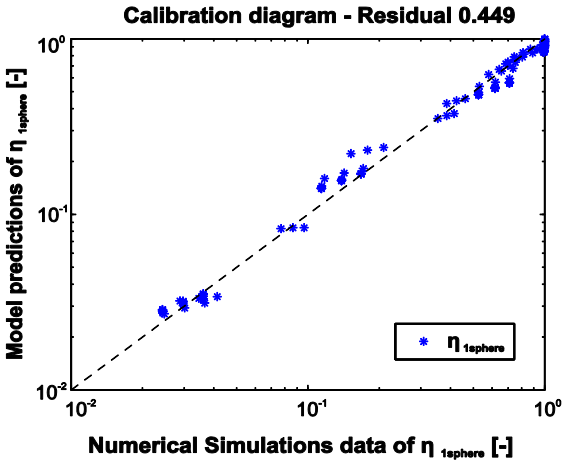

Figure 3-9: Calibration diagram of η (1st sphere)

The good agreement between the new correlation equation (Eq. 3-4) and the CFD data, as inferable from the calibration diagram in Figure 3-9, proves the mathematical structure reliability of the correlation equation proposed in the previous chapter. The coefficients and exponents are different because of the geometry (the new one is neither an isolate sphere neither the Happel's sphere-in-cell model).

In a similar way, a correlation equation to predict η_M (in absence of steric effect) was derived:

$$\eta_M = \gamma^2 \frac{13.0096A_S^{0.1939}U^{0.1939}(D/2a_c)^{0.8061} + 10.1225V^{0.3674}(D/2a_c)^{0.6325} - 5.1178A_S^{0.1278}U^{0.1278}V^{0.2494}(D/2a_c)^{0.6228}}{0.8334U + 0.2010V + 7.3612A_S^{0.1939}U^{0.1939}(D/2a_c)^{0.8061} + 6.1155V^{0.3674}(D/2a_c)^{0.6325} - 3.7885A_S^{0.1278}U^{0.1278}V^{0.2494}(D/2a_c)^{0.6228}}$$

.

Eq. 3-5

In this case the mechanisms of pure gravity, pure diffusion and advection/gravity were not considered since the results have shown that these mechanisms are not relevant for the collectors 2-5. The relative calibration diagram is shown in Figure 3-10.

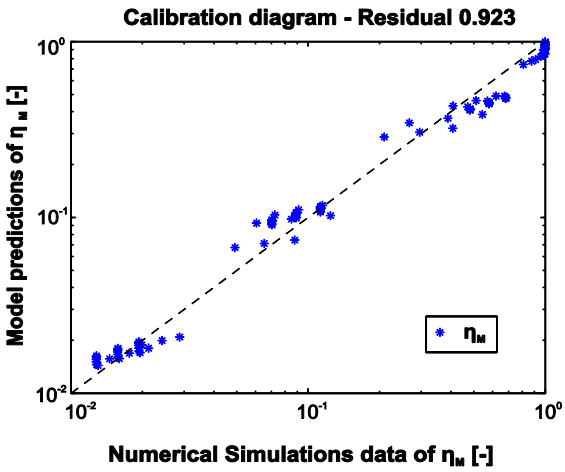

Figure 3-10: Calibration diagram of η_M

In Figure 3-11, the two proposed models (Eq. 3-4 and Eq. 3-5) are compared to numerical data for two typical ranges of parameters, showing that efficiency trend is well capture by the proposed equations.

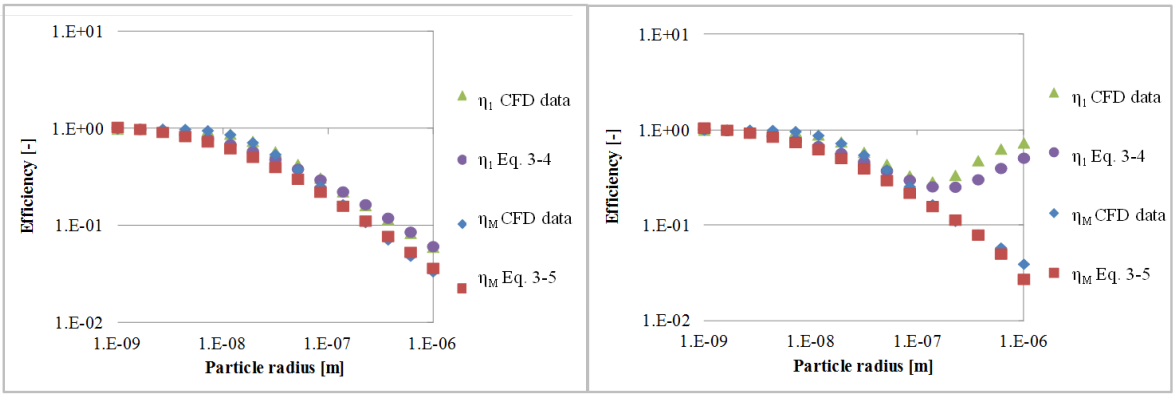

Figure 3-11: Comparison between the proposed equations (Eq. 3-4 and Eq. 3-5) and the numerical data for the efficiency of the first sphere and the average efficiency on the other spheres, in absence of steric effect. Data: n = 0.46, U = 10^{-6} m/s, a_c = 250 µm, T = 298 K and (from left to right) ρ_p = 998 , 5000 kg/m^3.

3.4 Conclusions

Based on the results presented in this chapter, it can be concluded that the common assumption that all the collectors of a porous medium act equally is not always applicable. In particular, when gravity plays an important role in deposition, the first sphere of a packing shows efficiency values considerably higher than the others. On the contrary, the assumption of constant efficiency along the packed bed is adequate when gravity is

negligible. Therefore a new equation to predict filter bed efficiency was proposed by introducing two collector efficiencies: one, η, for the first sphere of a packing and another, η_M, for the other collectors. A first attempt to evaluate η and η_M was also performed, without considering the steric effect. A further refinement will be carried out in the next future.

4 Chapter 4 - Conclusions

The importance of investigating particle transport and deposition in porous media and the wide use of deep bed filtration in various applications were discussed in the first chapter of this thesis. We particularly focus on the use of micro- and nano- particles in the aquifer remediation field.

In recent years, numerical simulations have become a very powerful tool to investigate colloid deposition from a microscale point of view, which is essential to understand the mechanisms at the base of the filtration phenomenon. One of the most important parameters used in the colloid filtration theory is the single collector contact efficiency η_0. This parameter can be defined and quantitatively estimated only from microscale studies, and, through appropriate equations, can be used to describe the filtration phenomenon at the macroscale, which is the point of view considered in real remediation activities and when planning field interventions.

Particle transport studies can be performed with Lagrangian or Eulerian approaches. The former has the advantage of allowing a rigorous mathematical description of all the forces acting on the particles. However, it is very computationally expensive and does not allow the investigation of the transport of a high number of particles. Therefore, it is extremely complex to apply a Lagrangian approach if statistical valuations of the results are required. On the contrary, the Eulerian approach allows the investigation of the problem from a different point of view, by describing the particles collectively in terms of their distribution in space. It permits the derivation of a number of results eligible to provide elaborations and statistics.

The aim of the first part of this thesis was to study and quantitatively evaluate the single collector contact efficiency η_0. For the above mentioned reasons, in this work the Eulerian approach was mainly used, considering the Lagrangian approach only when necessary (i.e., null diffusion cases).

Several models and correlation equations already exist in the literature to predict the single collector contact efficiency, but, given the complexity of the phenomenon, further analysis are needed. Moreover, the applicability of existing models presents some limitations. Firstly, many models predict efficiency values greater than one under specific conditions (i.e., for very small and very large particles and for low approach velocity). Secondly, they were derived under limiting assumptions that make them valid only within a specific range of parameters (namely N_{Pe} >70).

The complexity of the problem faced here requires the assumption of simplified geometries (isolate sphere) and models (perfect sink model, Smoluchowski-Levich approximation, etc.). Therefore, the work presented in this

thesis considers only the basic transport mechanisms (advection, gravity, Brownian diffusion and steric effect, without interaction forces) in a simple geometry, but investigates a wide range of parameters. The additivity concept, commonly used when deriving equations for the single collector efficiency, was not used here and different transport configurations were considered: a hierarchical fitting was performed leading to a new definition of the single collector efficiency (*total flux normalized* efficiency) and to the formulation of a new correlation equation. The proposed correlation equation has specific innovative and important features: it predicts efficiency values always lower than one and it is valid for a wide range of parameters. Moreover, it is also valid when one or more transport mechanisms are not active or are negligible and it includes also mixed terms accounting for the mutual interaction of concomitant transport mechanisms (i.e. advection, gravity and Brownian motion) and steric effect. The derived correlation equation was also extended in order to include porosity dependence and a reduced form was presented, including the most important mechanisms.

The second step of the work was to investigate the particle deposition in a column of spherical grains. The study outlined that the grains cannot be considered to operate identically, especially when gravity plays an important role in deposition. Therefore, a new equation to predict filter bed efficiency was proposed by introducing two collector efficiencies, one for the first sphere of a packing and another for all the other collectors, which can all be considered similar. Two models were proposed to predict these two efficiencies without considering the steric effect.

In conclusion, this work outlines the importance of a hierarchical approach to evaluate the efficiency of a single collector, in order to consider each possible deposition mechanism, and it highlights the different behaviour of the collectors in a simple packing.

These observations, if properly analysed and developed, would have important consequences for the study of colloid filtration. For instance, the understanding of particle deposition and retention mechanisms in aquifer systems is extremely important to estimate and plan the injection of reactants into the subsoil for remediation activities. Indeed, the deposition mechanisms knowledge is convenient to design a monitored and controlled delivery during the injection.

Future studies should focus on more complex and realistic geometries, e.g. a packing of non-spherical collectors. Moreover, particle-collector interaction mechanisms, in particular Van der Waals force and electric double layer interaction, should be considered in future works, together with the effect on the deposition efficiency of grain shape and of the structure of the porous medium void spaces. In this context, the work undertaken in this thesis can be considered a preliminary step for future developments.

5 Nomenclature

Symbol	Parameter	Units of measurement
A	Hamaker constant	J
A_{ii}	Hamaker constant for the material *i* interacting with the same material through void space	J
A_{ikj}	Hamaker constant for the material *i* interacting with the material *j* through the material *k*	J
a_c	Collector radius	m
a_p	Particle radius	m
A_s	Porosity dependent parameter	-
b	Radius of fluid envelope in Happel's model	m
c	Fluid-phase particle concentration	mol/m^3
C	Outlet particle concentration (in a packed bed)	mol/m3
C_0	Inlet particle concentration	mol/m^3
$\boldsymbol{D}$	Particle diffusion coefficient tensor	m^2/s
δ_m	Mass boundary layer thickness	m
e	Electron charge	C
$\boldsymbol{f_e}$	External body force exerted on a unit mass of the fluid	N/kg
$\boldsymbol{f}$	Resultant force on the particle	N
f_i	Hydrodynamic coefficients of delay (i=1,2,3,4)	-
$\boldsymbol{F}$	External force vector	N
$\boldsymbol{F_B}$	Brownian force	N
$\boldsymbol{F_D}$	Drag force	N
$\boldsymbol{F_{EDL}}$	Electric double layer force	N

$\boldsymbol{F_G}$	Gravity force	N
$\boldsymbol{F_{vdw}}$	Van der Waals force	N
$\boldsymbol{g}$	Acceleration of gravity	m/s^2
h	Particle-collector distance	m
H	Dimensionless particle – collector distance	-
I_s	Overall particle deposition rate	mol/s
$\hat{I}_S$	Overall particle deposition rate (CFD data)	mol/s
I_C	Overall particle rate through the cylinder surface	mol/s
$\hat{I}_C$	Overall particle rate through the cylinder surface (CFD data)	mol/s
k_B	Boltzman's constant	J/K
k	Permeability	m^2
L_0	Characteristic length of a system	m
L	Filter bed length	m
l	Thickness of the brush layer	m
M_s	Saturation magnetization	
M_w	Molecular weight of a polymer	uma
m	Particle mass	kg
$\overline{m_i}$	Magnetic dipole moment	Nm/T
n	Porosity	-
n	Versor normal to a surface	-
$n_{i,o}$	Bulk number concentration of ions of the i^{th} type	-
N_C	Total number of *UBE*	-
N_A	Attraction number	-
N_G	Gravity number	-
N_{Gi}	Function of the gravity number	-
N_{Lo}	London number	-
N_{Pe}	Pèclet number	-
N_{Re}	Reynolds number	-

N_R	Aspect ratio number	-
N_{Sc}	Smith number	-
N_{VdW}	Wan der Waals number	-
p	Hydrostatic pressure	N/m^2
$\tilde{p}$	Dimensionless hydrostatic pressure	N/m^2
r	Radial coordinate	m
R	Random-normal distribution number	-
T	Absolute temperature	K
$\boldsymbol{u}$	Particle velocity vector	m/s
U	Approach flow velocity	m/s
U_∞	Uniform flow velocity entering Happel's or Kuwabara's cell	m/s
$\boldsymbol{v}$	Fluid velocity vector	m/s
$\bar{v}$	Volume of one polymer molecule	m^3
$\tilde{v}$	Dimensionless velocity	-
v_ϕ	Fluid velocity component along ϕ coordinate	m/s
v_r	Fluid velocity components along r coordinate	m/s
v_θ	Fluid velocity components along θ coordinate	m/s
$\mathbf{V}$	Stokes sedimentation velocity	m/s
V_{EDL}	Electrical double layer potential	V
V_{el}	Elastic interaction potential	V
V_m	Magnetic interaction potential	V
V_{osm}	Osmotic interaction potential	V
V_{VdW}	Van der Waals potential	V
V_b	Born repulsion potential	V
V_{tot}	Total interaction potential	V
z_i	Valence of the i^{th} ions	-
α	Attachment efficiency	-
γ	Porosity function	-
ε_0	Dielectric constant of the void	F/m
ε_r	Relative dielectric constant of the material	-

ζ_c	Collector zeta potential	V
ζ_p	Particle zeta potential	V
η	Single collector removal efficiency (Isolate sphere)	-
η_γ	Single collector remuval efficiency (Happel's model)	-
η_0	Single collector contact efficiency (Isolate sphere)	-
$\eta_{0,\gamma}$	Single collector contact efficiency (Happel's model)	-
η_D	Single collector efficiency due to Brownian diffusion	-
η_G	Single collector efficiency due to gravitational sedimentation	-
η_I	Single collector efficiency due to interception	-
η_0^i	Single collector efficiency due to the *i*-mechanism of transport	-
η_N	Total flux normalized single collector efficiency	
$\hat{\eta}_N$	Total flux normalized single collector efficiency (CFD data)	
ξ	Friction coefficient (equal to $6\pi\mu a_p$)	Pa·s·m
θ	Tangential coordinate	rad
ϕ	coordinate	rad
κ	Debye - Huckel parameter	1/m
λ	Average wavelength of electron oscillation	m
μ	Fluid viscosity	Pa·s
v_0	Magnetic permeability in the vacuum	Tm/A
ρ_f	Fluid density	kg/m^3
ρ_p	Particle density	kg/m^3
ρ_χ	Polimer density	kg/m^3
σ_c	Collision diameter	m

φ_χ	Volume fraction of brush layer occupied by one molecule of polymer	-
χ	Flory-Huggins parameter	-
ψ	Steam function	m^2/s

Annex I – Different boundary conditions for the Happel's model

The Happel's model was described in Chapter 1 together with the analytical solution of its flow field. Several studies about colloid deposition used this model in order to represent the porous medium. Between these one of the most famous and used model is the one proposed in 2004 by Tufenkji and Elimelech (Tufenkji and Elimelech 2004). They performed numerical simulations with an Eulerian approach considering Brownian diffusion, gravity, interception and van der Waals interactions. They solved the convective diffusion equation (Eq. 1-35) with the following boundary conditions:

$$\text{a) } c = 0 \qquad \text{for } r = a_c$$
$$\text{b) } c = C_0 \qquad \text{for } r = b$$

Eq. A 1

In their work they derived the full correlation equation of η_N by evaluating, in three different steps, the three terms of deposition due to diffusion, gravity and interception, by using the additivity assumption. The final equation is reported in Table 1-3.

Different boundary conditions were proposed by Song and Elimelech (Song and Elimelech 1992) to avoid efficiency values greater than one:

$$\text{a) } c = 0 \qquad \text{for } r = a_c$$
$$\text{b) } v_r c - D\frac{\partial c}{\partial r} = -UC_0\cos\theta \qquad \text{for } r = b, 0 \le \theta < \frac{\pi}{2}$$
$$\text{c) } \frac{\partial c}{\partial r} = 0 \qquad \text{for } r = b, \frac{\pi}{2} \le \theta \le \pi$$

Eq. A 2

Different concentration profile, for low Peclet number, can be obtained by applying the two kinds of boundary conditions, as inferable from Figure A 1 and Figure A 2. The two boundary conditions coincide for medium/high Peclet numbers.

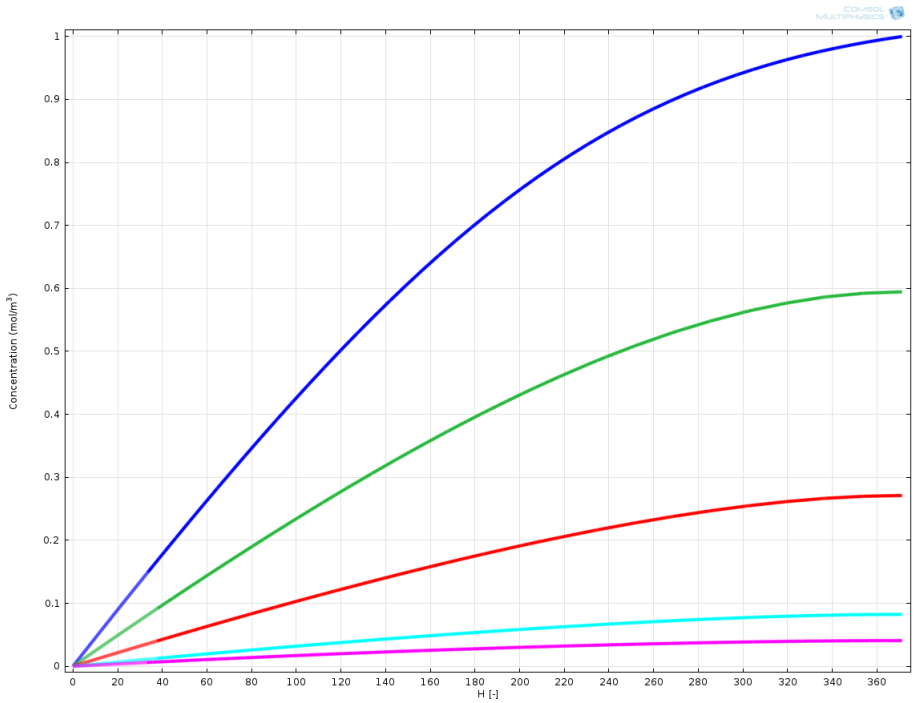

Figure A 1: Concentration profiles as function of the dimensionless distance *H* in different section of the Happel's model (blue line, θ = 0°; green line, θ = 120°; red line, θ = 150°; cyan line, θ = 170°; magenta line, θ = 180°). Song and Elimelech (Song and Elimelech 1992) boundary conditions were applied. N_{Pe} = 0.025. [Adapted from (Song and Elimelech 1992)].

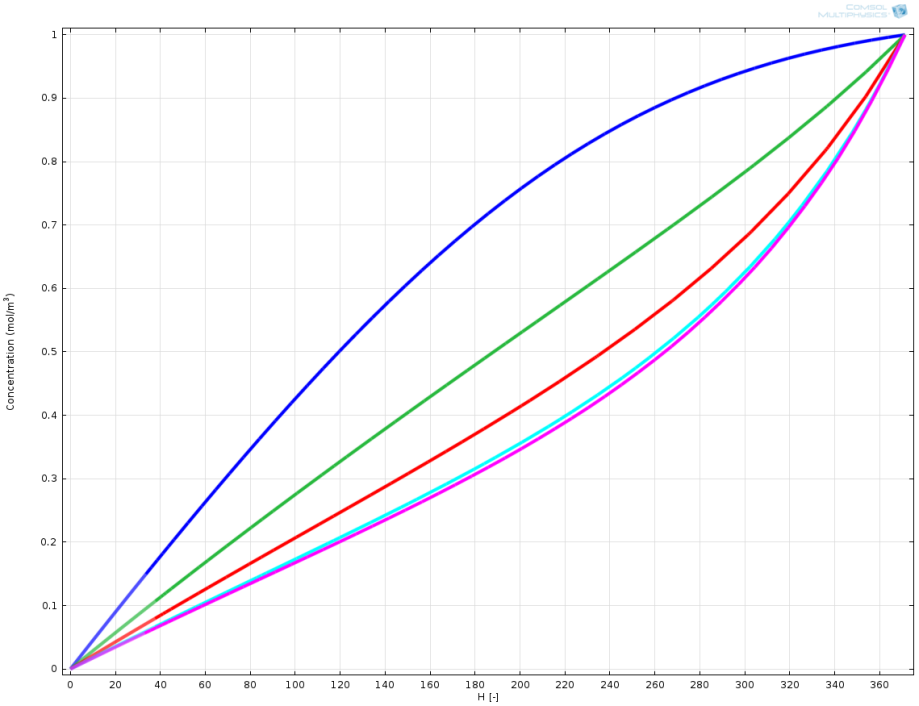

Figure A 2: : Concentration profiles as function of the dimensionless distance *H* in different section of the Happel's model (blue line, θ = 0°; green line, θ = 120°; red line, θ = 150°; cyan line, θ = 170°; magenta line, θ = 180°). Tufenkji and Elimelech (Tufenkji and Elimelech 2004) boundary conditions were applied. N_{Pe} = 0.025. [Adapted from (Song and Elimelech 1992)].

Annex II - Fitting procedure steps

All the steps of the hierarchical fitting of the study proposed in Chapter 0 are here presented.

In each of the figure below the red crosses represent the CFD simulations results and the blue circles are the model predictions. In each figure the mass flux on the spherical collector I_s (upper graph), the mass flux through the cylinder surface I_c (middle graph) and the *total flux normalized* efficiency η_N (lower graph) are reported, together with their equations.

First step (single transport mechanisms)

- (1.a) Advection

Analytical solutions are available in this case (Eq. A 3):

$$I_S = 0$$
$$I_C = \pi a_c^2 U$$
$$\eta_N = \frac{I_S}{I_C}$$

Eq. A 3

- (2.a) Gravity

Analytical solutions are available in this case (Eq. A 4):

$$I_S = \pi a_c^2 V$$
$$I_C = \pi a_c^2 V$$
$$\eta_N = \frac{I_S}{I_C}$$

Eq. A 4

- (3.a) Diffusion

Figure A 3 reports the CFD data and the model predictions.

$$I_S = \pi a_c^2 7.5609\left(D/2a_c\right)$$

$$I_C = \pi a_c^2 7.5609\left(D/2a_c\right)$$

$$\eta_N = \frac{I_S}{I_C}$$

Eq. A 5

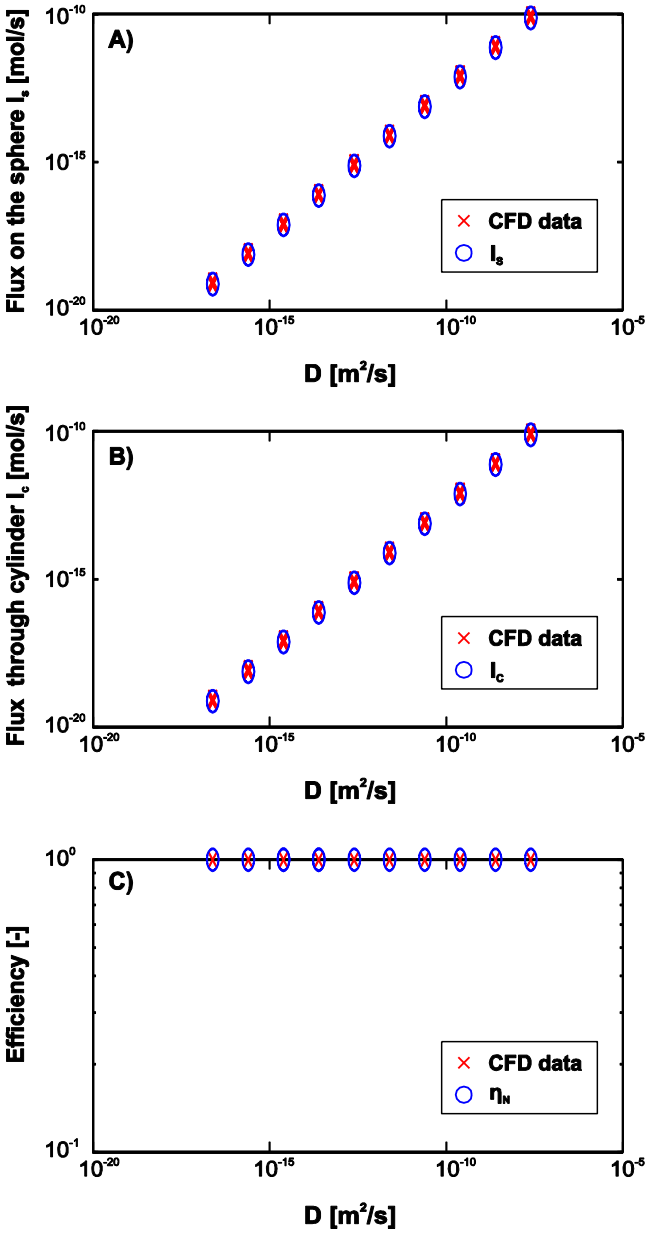

Figure A 3: Flux on the sphere (A), flux through the cylinder (B) and normalized efficiency (C) in case of pure diffusion. The equations are shown in Eq. A 5.

- (1.b) Advection and steric effect

Figure A 4 reports the CFD data and the model predictions.

$$I_S = \pi a_c^2 1.5062 N_R^{1.9834}$$
$$I_C = \pi a_c^2 U \left(1 + 6.0098 N_R^{1.9834}\right)$$
$$\eta_N = \frac{I_S}{I_C}$$

Eq. A 6

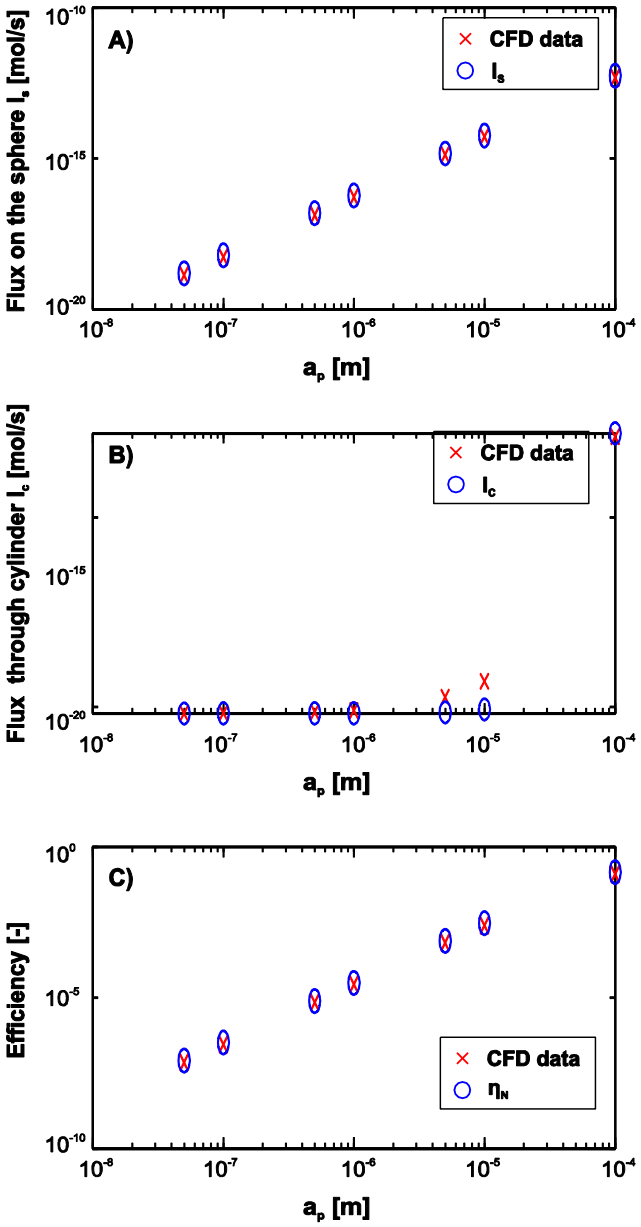

Figure A 4: Flux on the sphere (A), flux through the cylinder (B) and normalized efficiency (C) in case of advection and steric effect (interception). The equations are shown in Eq. A 6.

- (2.b) Diffusion and steric effect

Figure A 5 reports the CFD data and the model predictions.

$$I_S = \pi a_c^2 \left(D / 2a_c \right) \left(7.5609 + 4.9534 N_R^1 \right)$$

$$I_C = \pi a_c^2 \left(D / 2a_c \right) \left(7.5609 + 4.9534 N_R^1 \right)$$

$$\eta_N = \frac{I_S}{I_C}$$

Eq. A 7

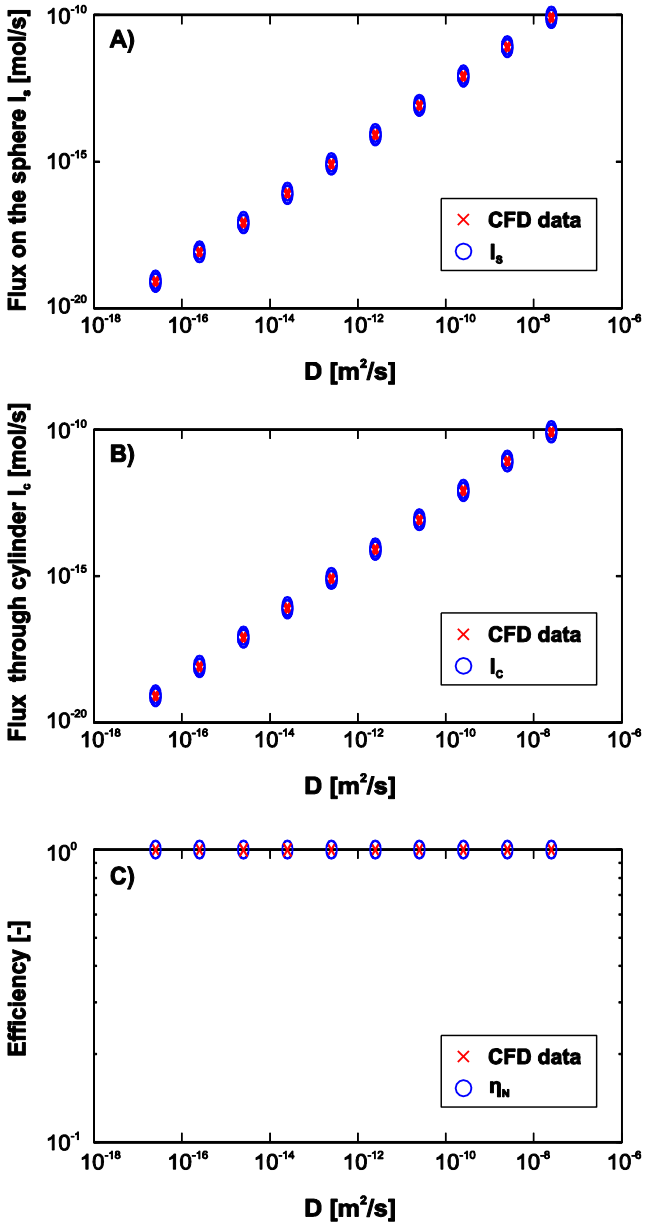

Figure A 5: Flux on the sphere (A), flux through the cylinder (B) and normalized efficiency (C) in case of diffusion and steric effect. The equations are shown in Eq. A 7.

- (3.b) Gravity and steric effect

Figure A 6 reports the CFD data and the model predictions.

$$I_S = \pi a_c^2 V \left(1 + 6.0187 N_R^2\right)$$

$$I_C = \pi a_c^2 V \left(1 + 6.0187 N_R^2\right)$$

$$\eta_N = \frac{I_S}{I_C}$$

Eq. A 8

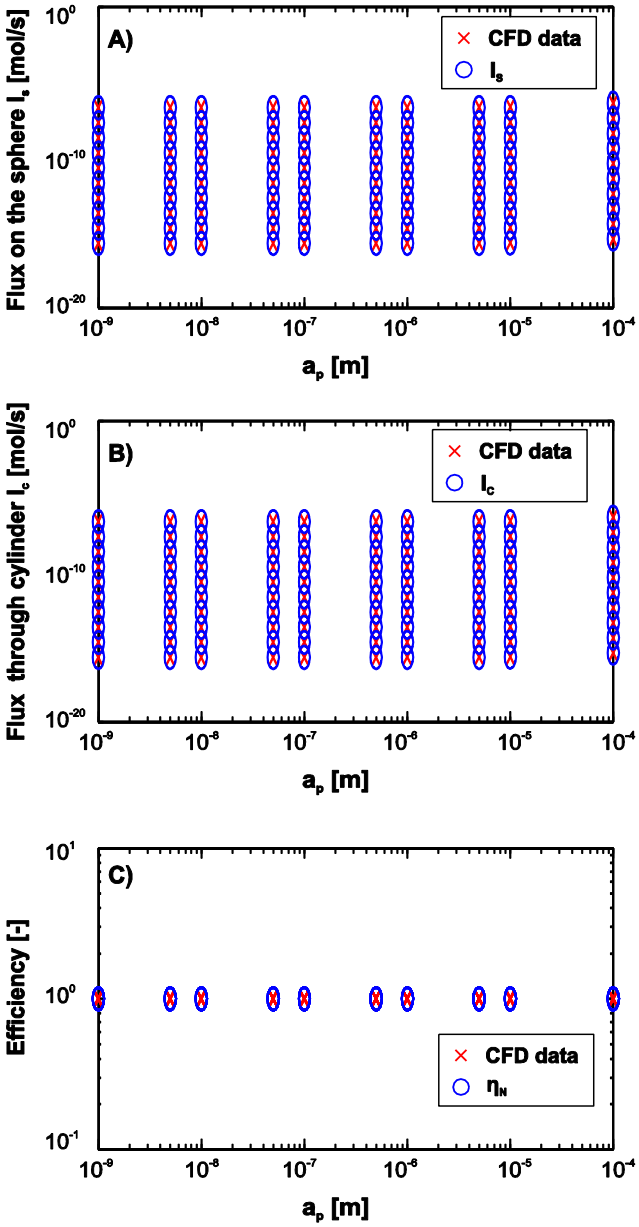

Figure A 6: Flux on the sphere (A), flux through the cylinder (B) and normalized efficiency (C) in case of gravity and steric effect. The equations are shown in Eq. A 8.

Second step (coupled transport mechanisms)

- (4.a) Advection and gravity

Figure A 7 reports the CFD data and the model predictions.

$$I_S = \pi a_c^2 \left[V + 0.0442 U^{0.1259} V^{0.8741} \right]$$

$$I_C = \pi a_c^2 V \left[V + 0.0442 U^{0.1259} V^{0.8741} \right]$$

$$\eta_N = \frac{I_S}{I_C}$$

Eq. A 9

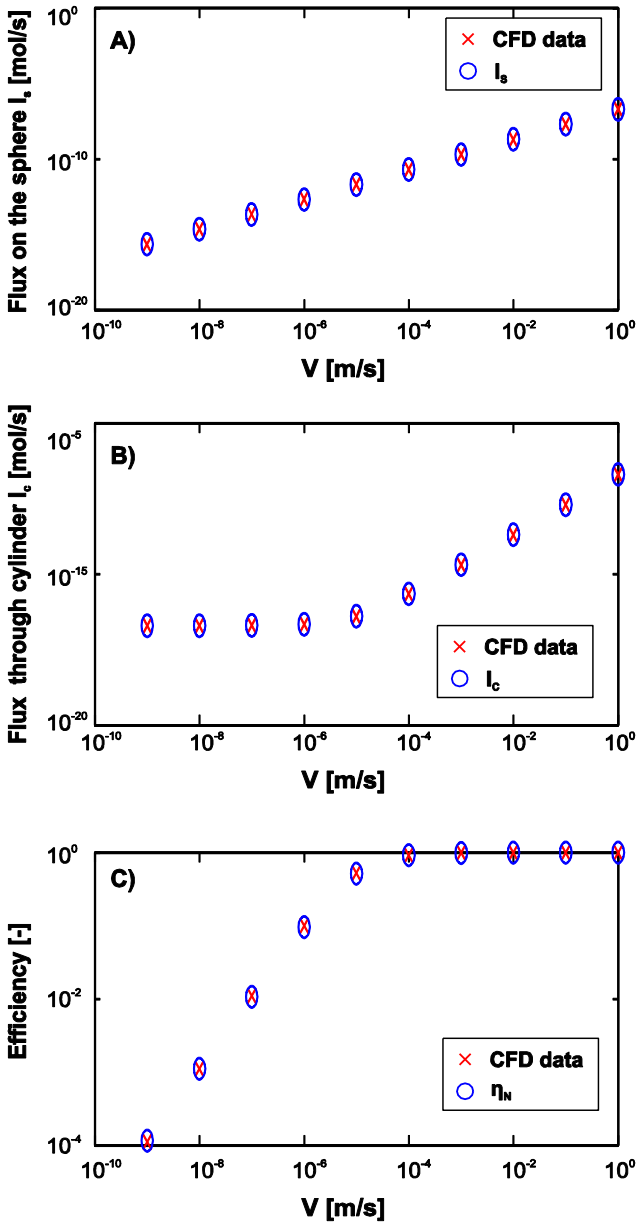

Figure A 7: Flux on the sphere (A), flux through the cylinder (B) and normalized efficiency (C) in case of gravity and advection. The equations are shown in Eq. A 9.

- (5.a) Advection and diffusion

Figure A 8 reports the CFD data and the model predictions.

$$I_S = \pi a_c^2 \left[7.5609 \left(D/2a_c \right) + 2.9352 U^{0.3662} \left(D/2a_c \right)^{0.6338} \right]$$

$$I_C = \pi a_c^2 \left[7.5609 \left(D/2a_c \right) + 2.9352 U^{0.3662} \left(D/2a_c \right)^{0.6338} \right]$$

$$\eta_N = \frac{I_S}{I_C}$$

Eq. A 10

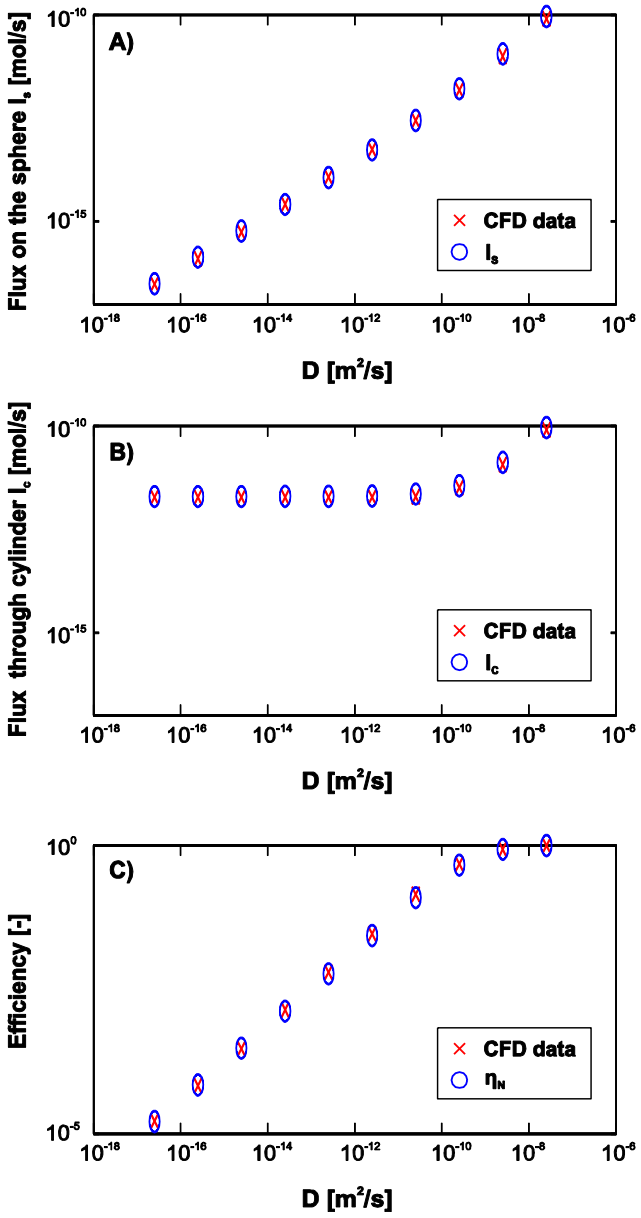

Figure A 8: Flux on the sphere (A), flux through the cylinder (B) and normalized efficiency (C) in case of diffusion and advection. The equations are shown in Eq. A 10.

- (6.a) Diffusion and gravity

Figure A 9 reports the CFD data and the model predictions.

$$I_S = \pi a_c^2 \left[V + 7.5609 \left(D/2a_c \right) + 0.9461 V^{0.6650} \left(D/2a_c \right)^{0.3450} \right]$$

$$I_C = \pi a_c^2 \left[V + 7.5609 \left(D/2a_c \right) + 2.7972 V^{0.6650} \left(D/2a_c \right)^{0.3450} \right]$$

$$\eta_N = \frac{I_S}{I_C}$$

Eq. A 11

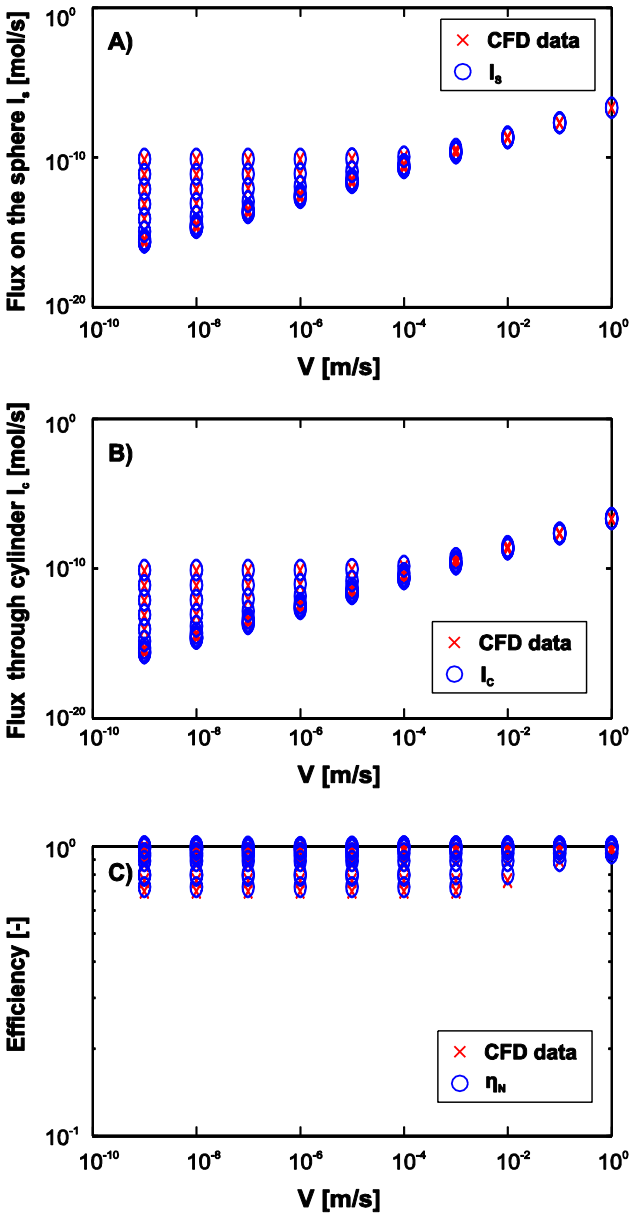

Figure A 9: Flux on the sphere (A), flux through the cylinder (B) and normalized efficiency (C) in case of diffusion and gravity. The equations are shown in Eq. A 11.

- (4.b) Advection, gravity and steric effect

Figure A 10 reports the CFD data and the model predictions.

$$I_S = \pi a_c^2 \left[1.5062 U N_R^{1.9834} + V\left(1 + 6.0187 N_R^2\right) + U^{0.1259} V^{0.8741} \left(0.0442 + 0.1220 N_R^{0.4210}\right) \right]$$

$$I_C = \pi a_c^2 \left[U\left(1 + 6.0098 N_R^{1.9834}\right) + V\left(1 + 6.0187 N_R^2\right) + U^{0.1259} V^{0.8741} \left(0.0442 + 0.1220 N_R^{0.4210}\right) \right]$$

$$\eta_N = \frac{I_S}{I_C}$$

Eq. A 12

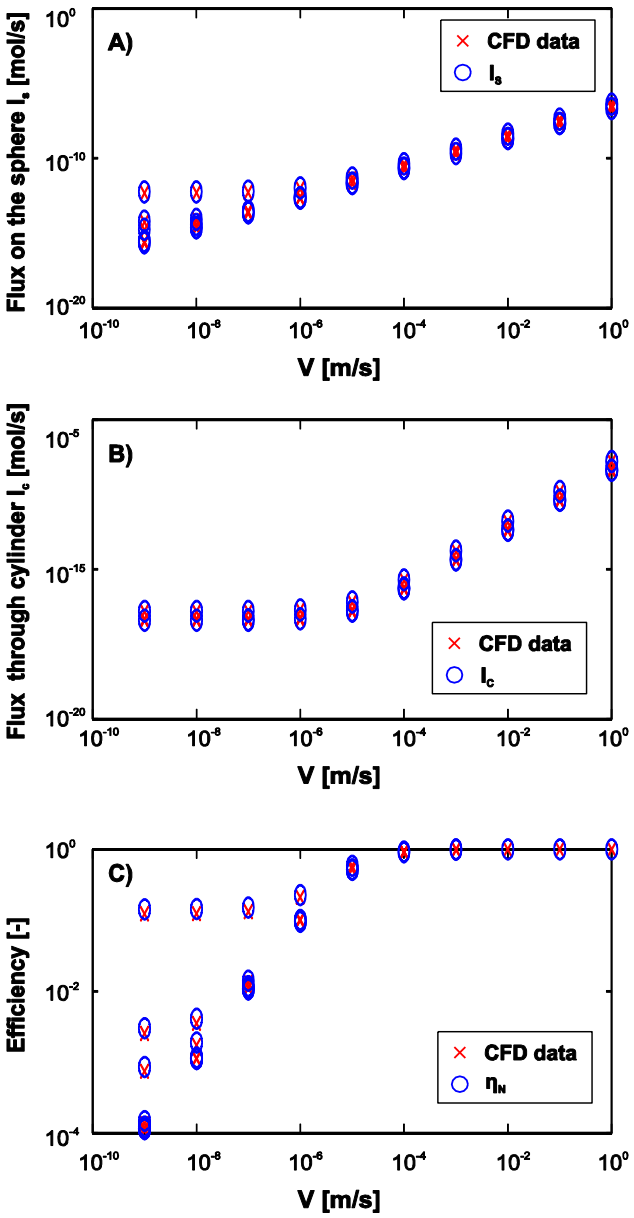

Figure A 10: Flux on the sphere (A), flux through the cylinder (B) and normalized efficiency (C) in case of advection, gravity and steric effect. The equations are shown in Eq. A 12.

- (5.b) Advection, diffusion and steric effect

Figure A 11 reports the CFD data and the model predictions.

$$I_S = \pi a_c^2 \left[1.5062 U N_R^{1.9834} + \left(D/2a_c \right) \left(7.5609 + 4.9534 N_R^1 \right) + U^{0.3662} \left(D/2a_c \right)^{0.6338} \left(2.9352 + 2.7480 N_R^{0.3737} \right) \right]$$

$$I_C = \pi a_c^2 \left[U \left(1 + 6.0098 N_R^{1.9834} \right) + \left(D/2a_c \right) \left(7.5609 + 4.9534 N_R^1 \right) + U^{0.3662} \left(D/2a_c \right)^{0.6338} \left(2.9352 + 2.7480 N_R^{0.3737} \right) \right]$$

$$\eta_N = \frac{I_S}{I_C}$$

Eq. A 13

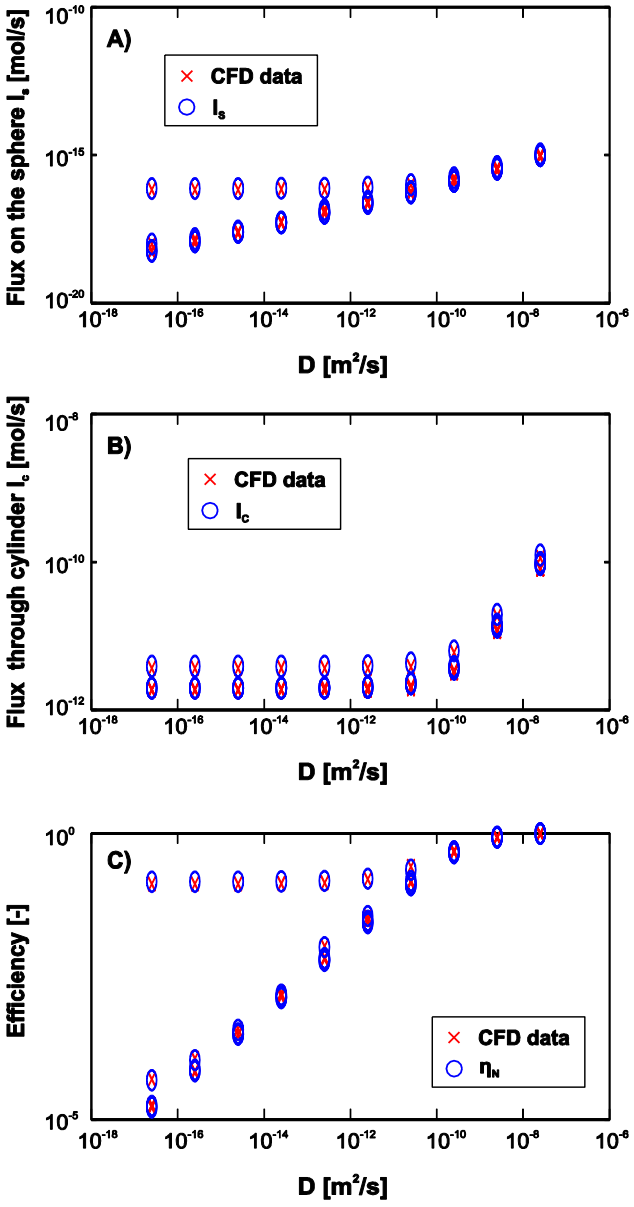

Figure A 11: Flux on the sphere (A), flux through the cylinder (B) and normalized efficiency (C) in case of advection, diffusion and steric effect. The equations are shown in Eq. A 13.

- (6.b) Diffusion, gravity and steric effect

Figure A 12 reports the CFD data and the model predictions.

$$I_S = \pi a_c^2 \left[V\left(1+6.0187N_R^2\right) + \left(D/2a_c\right)\left(7.5609+4.9534N_R^1\right) + V^{0.6650}\left(D/2a_c\right)^{0.3450}\left(0.9461+1.1626N_R^{0.6012}\right)\right]$$

$$I_C = \pi a_c^2 \left[V\left(1+6.0187N_R^2\right) + \left(D/2a_c\right)\left(7.5609+4.9534N_R^1\right) + V^{0.6650}\left(D/2a_c\right)^{0.3450}\left(2.7972+3.4372N_R^{0.6012}\right)\right]$$

$$\eta_N = \frac{I_S}{I_C}$$

Eq. A 14

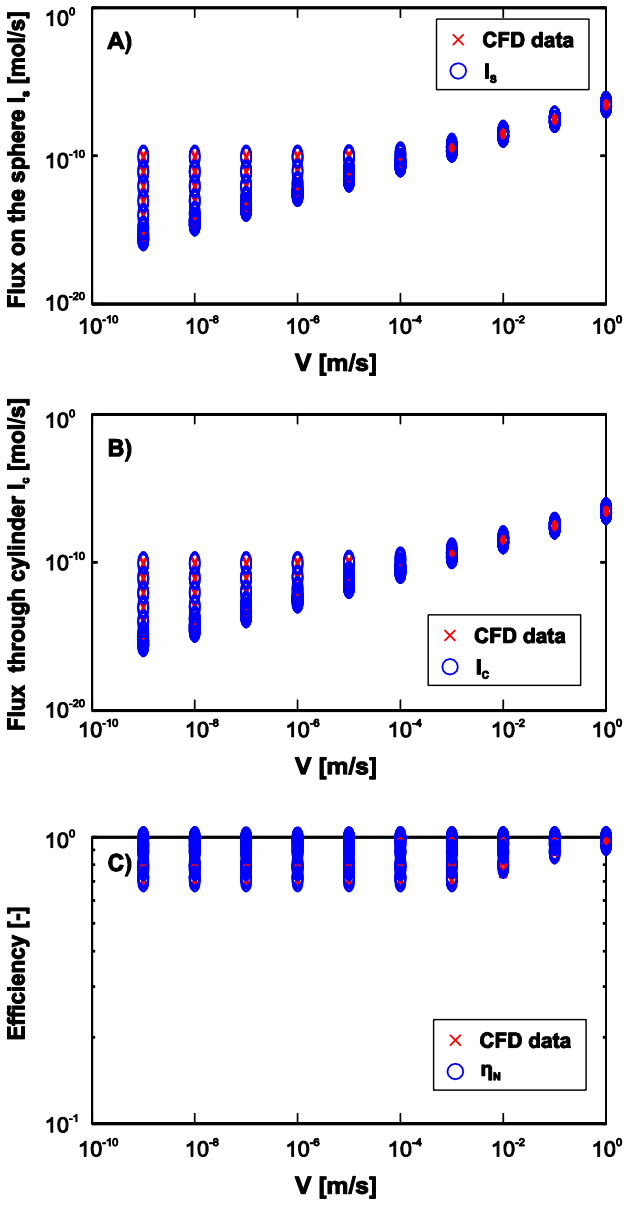

Figure A 12: Flux on the sphere (A), flux through the cylinder (B) and normalized efficiency (C) in case of gravity, diffusion and steric effect. The equations are shown in Eq. A 14.

Third step (three transport mechanisms)

- (7.a) Advection, diffusion and gravity

Figure A 13 reports the CFD data and the model predictions.

$$I_S = \pi a_c^2 \left[V + 7.5609\left(D/2a_c\right) + 0.0442U^{0.1259}V^{0.8741} + 2.9352U^{0.3662}\left(D/2a_c\right)^{0.6338} + 0.9461V^{0.6650}\left(D/2a_c\right)^{0.3450} - 0.6740U^{0.1562}V^{0.5873}\left(D/2a_c\right)^{0.2565} \right]$$

$$I_C = \pi a_c^2 \left[V + 7.5609\left(D/2a_c\right) + 0.0442U^{0.1259}V^{0.8741} + 2.9352U^{0.3662}\left(D/2a_c\right)^{0.6338} + 2.7972V^{0.6650}\left(D/2a_c\right)^{0.3450} - 1.1945U^{0.1562}V^{0.5873}\left(D/2a_c\right)^{0.2565} \right]$$

$$\eta_N = \frac{I_S}{I_C}$$

Eq. A 15

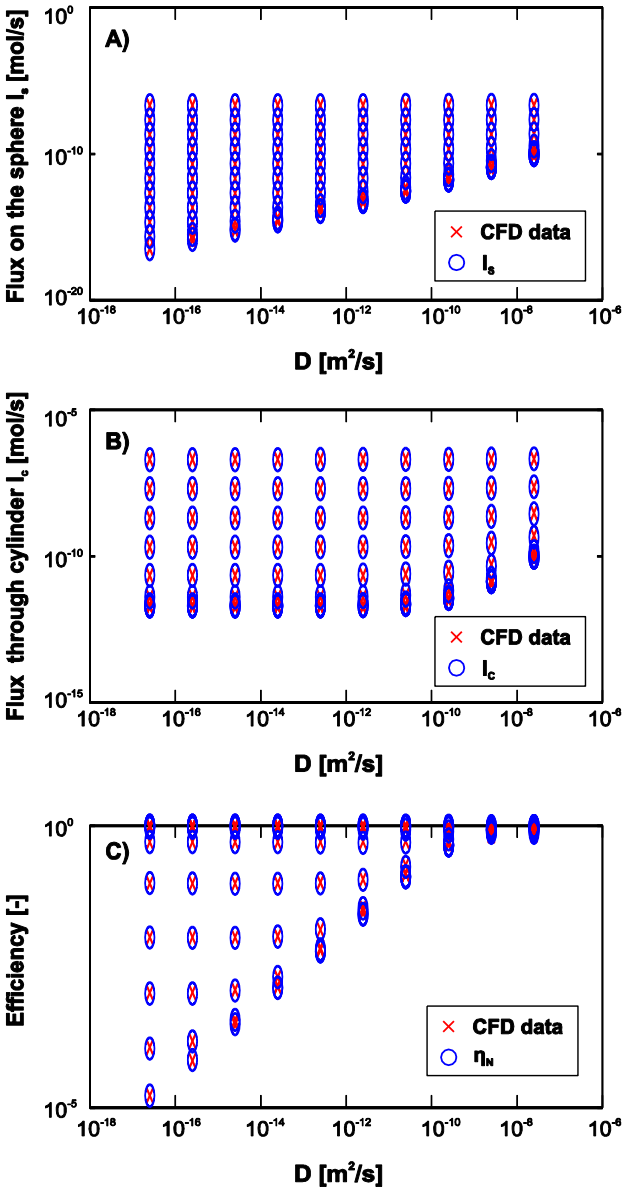

Figure A 13: Flux on the sphere (A), flux through the cylinder (B) and normalized efficiency (C) in case of advection, gravity and diffusion. The equations are shown in Eq. A 15.

- (7.b) Advection, diffusion, gravity and steric effect

Figure A 14 reports the CFD data and the model predictions.

$$I_S = \pi a_c^2 \left[1.5062 U N_R^{1.9834} + V\left(1 + 6.0187 N_R^2\right) + \left(D/2a_c\right)\left(7.5609 + 4.9534 N_R^1\right) + \right.$$
$$U^{0.1259} V^{0.8741}\left(0.0442 + 0.1220 N_R^{0.4210}\right) + U^{0.3662}\left(D/2a_c\right)^{0.6338}\left(2.9352 + 2.7480 N_R^{0.3737}\right) +$$
$$\left. V^{0.6650}\left(D/2a_c\right)^{0.3450}\left(0.9461 + 1.1626 N_R^{0.6012}\right) + U^{0.1562} V^{0.5873}\left(D/2a_c\right)^{0.2565}\left(-0.6740 - 0.7119 N_R^{0.5438}\right) \right]$$

$$I_C = \pi a_c^2 \left[U\left(1 + 6.0098 N_R^{1.9834}\right) + V\left(1 + 6.0187 N_R^2\right) + \left(D/2a_c\right)\left(7.5609 + 4.9534 N_R^1\right) + \right.$$
$$U^{0.1259} V^{0.8741}\left(0.0442 + 0.1220 N_R^{0.4210}\right) + U^{0.3662}\left(D/2a_c\right)^{0.6338}\left(2.9352 + 2.7480 N_R^{0.3737}\right) +$$
$$\left. V^{0.6650}\left(D/2a_c\right)^{0.3450}\left(2.7972 + 3.4372 N_R^{0.6012}\right) + U^{0.1562} V^{0.5873}\left(D/2a_c\right)^{0.2565}\left(-1.1945 - 1.2616 N_R^{0.5438}\right) \right]$$

$$\eta_N = \frac{I_S}{I_C}$$

Eq. A 16

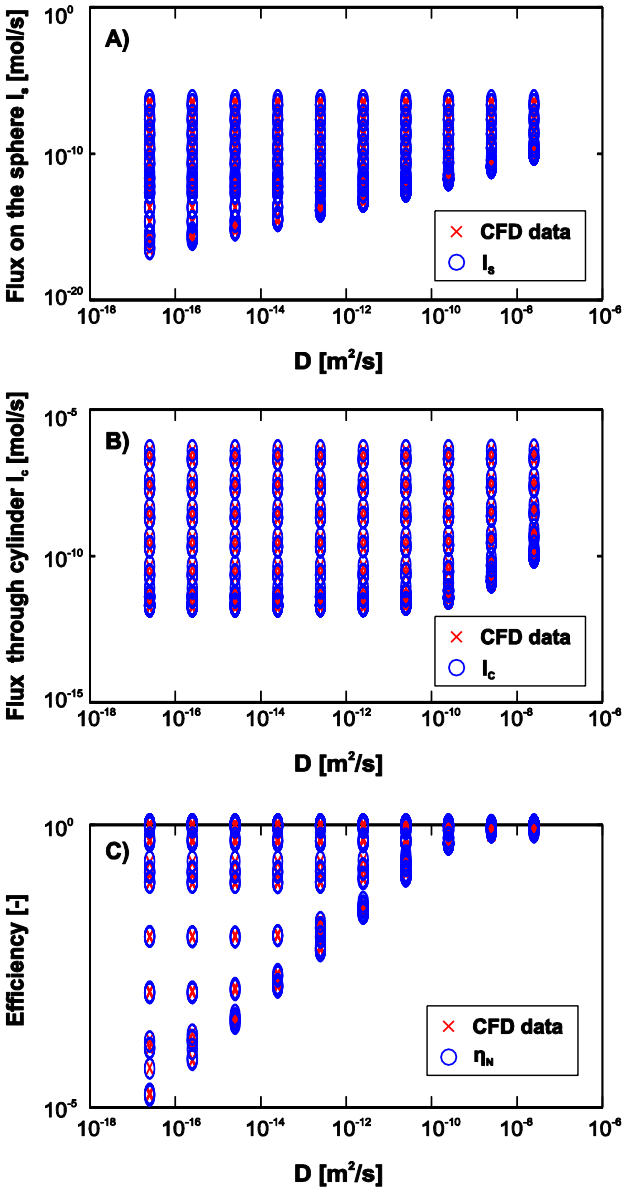

Figure A 14: Flux on the sphere (A), flux through the cylinder (B) and normalized efficiency (C) in case of advection, gravity, diffusion and steric effect. The equations are shown in Eq. A 16.

Annex III – Different η_N precision degrees

The fitting of the data used in the study proposed in Chapter 0 was performed with a hierarchical process starting from the cases with only one active transport mechanism and ending with the case with all of them active. Each step contributes to make the fitting more precise and to reduce the residual between the model of η_N and the numerical data.

Single mechanisms

If only single transport mechanisms are considered, the equation of η_N becomes:

$$\eta_N = \frac{\sum_{i=1}^{3} I_{s,i}}{\sum_{i=1}^{3} I_{c,i}} = \frac{I_{s,1}^{A,S} + I_{s,2}^{G,S} + I_{s,3}^{D,S}}{I_{c,1}^{A,S} + I_{c,2}^{G,S} + I_{c,3}^{D,S}}$$

Eq. A 17

Figure A15 reports the calibration diagram in this case; the plot shows a very bad agreement between the model and the CFD data.

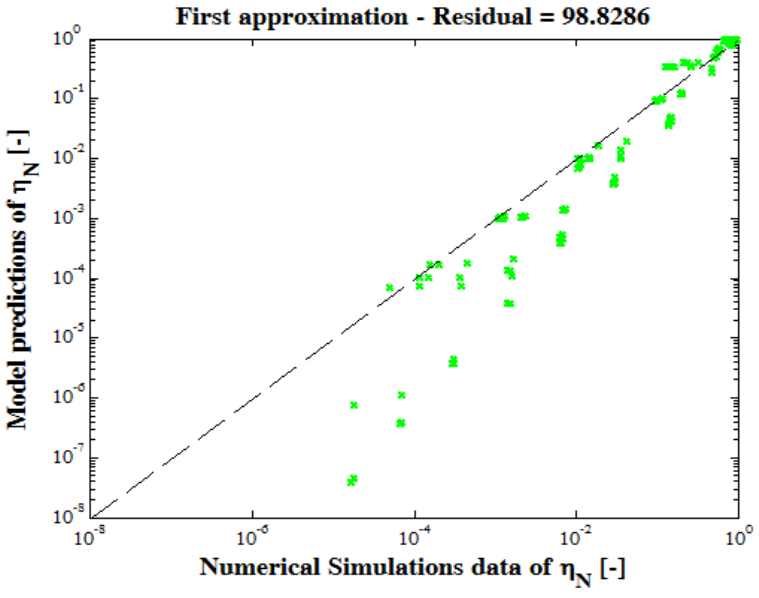

Figure A15: Calibration diagram of η_N when only single transport mechanisms are considered.

Single and coupled mechanisms

If single transport mechanism terms *(i=1-3)* and the mixed terms *(i=4-6)* are considered, the equation of η_N becomes:

$$\eta_N = \frac{\sum_{i=1}^{6} I_{s,i}}{\sum_{i=1}^{6} I_{c,i}} = \frac{I_{s,1}^{A,S} + I_{s,2}^{G,S} + I_{s,3}^{D,S} + I_{s,4}^{AG,S} + I_{s,5}^{AD,S} + I_{s,6}^{DG,S}}{I_{c,1}^{A,S} + I_{c,2}^{G,S} + I_{c,3}^{D,S} + I_{c,4}^{AG,S} + I_{c,5}^{AD,S} + I_{c,6}^{DG,S}}$$

Eq. A 18

The calibration diagram is reported in Figure A 16, the agreement between the model and the CFD data is considerably improved.

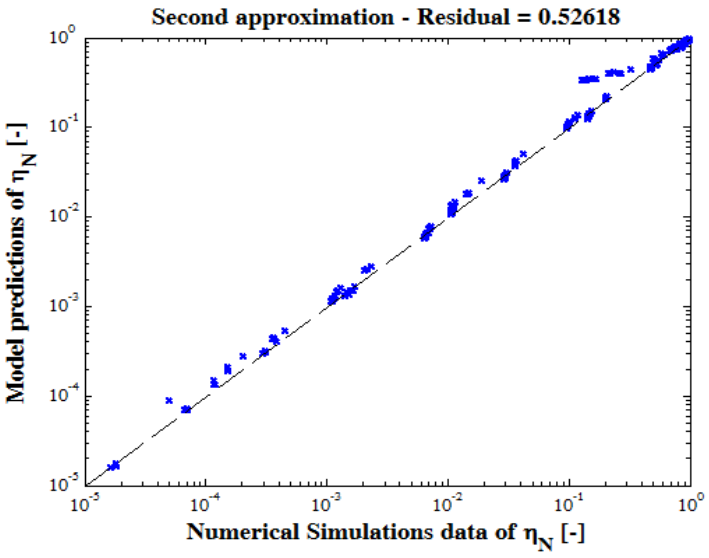

Figure A 16: Calibration diagram of η_N when single and coupled transport mechanisms are considered.

Full η_N equation

If also the triple term *(i=7)* which considers the interaction between all the possible transport mechanisms is considered (together with the others determined in the previous steps) the final equation of the *total flux normalized* becomes:

$$\eta_N = \frac{\sum_{i=1}^{7} I_{s,i}}{\sum_{i=1}^{7} I_{c,i}} = \frac{I_{s,1}^{A,S} + I_{s,2}^{G,S} + I_{s,3}^{D,S} + I_{s,4}^{AG,S} + I_{s,5}^{AD,S} + I_{s,6}^{DG,S} + I_{s,7}^{AGD,S}}{I_{c,1}^{A,S} + I_{c,2}^{G,S} + I_{c,3}^{D,S} + I_{c,4}^{AG,S} + I_{c,5}^{AD,S} + I_{c,6}^{DG,S} + I_{c,7}^{AGD,S}}$$

Eq. A 19

The calibration diagram is reported in Figure A 16.

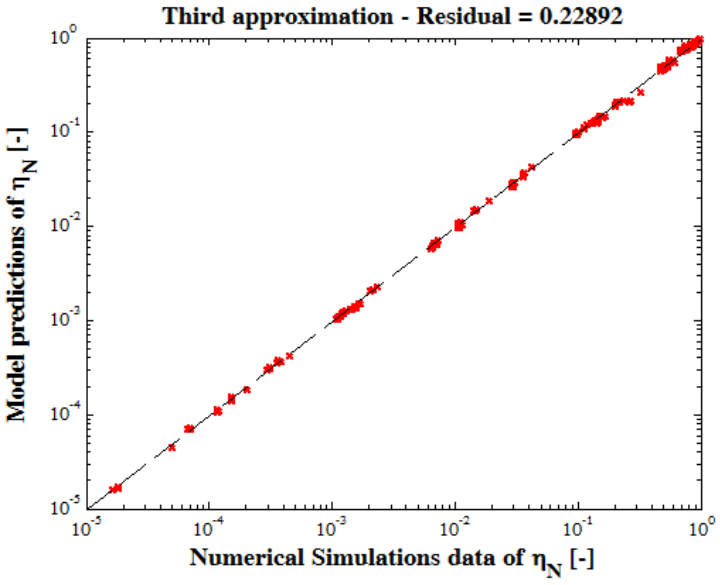

Figure A 17 Calibration diagram of η_N (the full model).

Annex IV – Role of Porosity

In this appendix the introduction of porosity dependency in the *total flux normalized* efficiency correlation equation (presented in Chapter 0) will be discussed. The derivation of the pure diffusion term will also be provided here.

Firstly, we want to remind here that most of the correlation equations available in literature were derived for the Happel's sphere in cell model (or the hemisphere in cell model), which accounts for porosity dependency through the two parameters A_S and γ, whose definitions are:

$$\gamma = (1-n)^{1/3}$$

$$\gamma = a_c / b \quad \text{for the Happel's model}$$

$$A_S = \frac{2(1-\gamma^5)}{2-3\gamma+3\gamma^5-2\gamma^6}$$

Eq. A 20

where n is the porosity, a_c is the collector radius and b is the fluid envelope radius in the Happel's model.

As already mention in Chapter 1, the original Yao et al. equation (Yao, et al. 1971) doesn't account for porosity variations since it was derived for a sphere in an infinite domain ($n \rightarrow 1$). Yao et al. reported a correction for the diffusive term by introducing the coefficient $A_S^{1/3}$, derived by Pfeffer (Pfeffer 1964). Also the interception term was corrected by A_S leading to Eq. 1-39 (Elimelech 1995).

Analogously, our correlation equations of η_N and η_0 (Eq. 2-9 and Eq. 2-10) were corrected introducing, in the in each term, A_S raised with the same power of the advective velocity U. Because of gravitational sedimentation is not affected by porosity (Tufenkji and Elimelech 2005), the terms related to gravity were not changed. Conversely, the pure diffusion deposition term need to be related to porosity. With this purpose, the term due to pure diffusion was divided by $(2-2\gamma)$ in order to switch from a pseudo infinite domain to the Happel's sphere in cell model (with the boundary conditions proposed by Song and Elimelech (Song and Elimelech 1992)). Moreover, the relationships were further modified, considering also γ^2, in order to normalized the efficiency over the whole fluid envelope according to Eq. 1-40 (Logan, et al. 1995; Nelson and Ginn 2005) leading to Eq. 2-11 and Eq. 2-12.

Deposition due to pure diffusion

The aim of this paragraph is to explain the mathematical passages that lead to the evaluation of the particle flux due to pure diffusion ($N_{Pe} \to 0$) on a spherical collector.

The same mathematical procedure performed by Levich (Levich 1962) will be presented starting from the advection-diffusion equation in radial coordinate:

$$v_r \frac{\partial c}{\partial r} + \frac{v_\theta}{r} \frac{\partial c}{\partial \theta} = D\left(\frac{\partial^2 c}{\partial r^2} + \frac{2}{r} \frac{\partial c}{\partial r} \right)$$

Eq. A 21

which, in case of null advection $(v_r, v_\theta) = (0,0)$, becomes:

$$\frac{\partial^2 c}{\partial r^2} = -\frac{2}{r} \frac{\partial c}{\partial r}$$

Eq. A 22

By introducing the new variable $t = \frac{\partial c}{\partial r}$ and performing the following passages, Eq. A 23 can be derived:

$$\frac{\partial t}{\partial r} = -\frac{2}{r} t$$

$$\frac{\partial t}{t} = -\frac{2}{r} \partial r$$

$$\ln(t) = -2\ln(r) + k$$

$$t = K r^{-2} = \frac{K}{r^2}$$

$$\frac{\partial c}{\partial r} = \frac{K}{r^2}$$

$$\partial c = \frac{K}{r^2} \partial r$$

$$c = -\frac{K}{r} + K_1$$

Eq. A 23

The final solution of Eq. A 23 depends on the boundary conditions and, therefore, on the geometry.

Spherical collector in an infinite domain

In case of a spherical collector in an infinite domain the boundary conditions used to solve Eq. A 23 are:

$$\begin{cases} c = 0 & \text{at } r = a_c \\ c = C_0 & \text{at } r = \infty \end{cases}$$

Eq. A 24

By implementing Eq. A 24 in Eq. A 23, K and K_1 are fixed:

$$\begin{cases} C_0 = K_1 \\ 0 = -\dfrac{K}{a_c} + K_1 \rightarrow K = C_0 a_c \end{cases}$$

Therefore, the final solution of Eq. A 23, for an isolate sphere, is:

$$c = -\frac{C_0 a_c}{r} + C_0 = C_0\left(1 - \frac{a_c}{r}\right)$$

Eq. A 25

The diffusion flux to the surface of the collector J_S is:

$$J_s = D\left(\frac{\partial c}{\partial r}\right)_{r=a_c} = D\left(\frac{C_0 a_c}{r^2}\right)_{r=a_c} = \frac{DC_0}{a_c}$$

Eq. A 26

and the total flux I_s:

$$I_s = \int_{S\_sphere} J_S dS = \frac{DC_0}{a_c} 4\pi a_c^2 = 4\pi a_c DC_0$$

Eq. A 27

By dividing I_s by the advective flux coming from the collector projection (definition of η_0) we obtain:

$$\eta_0^D = \frac{4\pi a_c DC_0}{C_0 U \pi a_c^2} = 8N_{Pe}^{-1}$$

Eq. A 28

(in accordance with the term of pure diffusion of the proposed model of η_N, which is $7.5609N_{Pe}^{-1}$).

The diffusive flux coming into the "infinite" domain can be described with:

$$I_{r=\infty} = \lim_{r\to\infty} \int_{S(r)} JdS = \lim_{r\to\infty}\left(\frac{DC_0 a_c}{r^2} 4\pi r_c^2\right) = 4\pi a_c DC_0$$

Eq. A 29

The diffusive flux which deposits onto the spherical isolate collector is equal to the flux entering into the domain (in accordance with the results reported in Annex II - Fitting procedure steps).

Happel's sphere in an infinite domain

The easier boundary conditions (Tufenkji and Elimelech 2004) to solve Eq. A 23 in the Happel's model are:

$$\begin{cases} c = 0 & \text{at } r = a_c \\ c = C_0 & \text{at } r = b \end{cases}$$

Eq. A 30

By implementing Eq. A 30 in Eq. A 23, K and K_1 are fixed:

$$\begin{cases} C_0 = -\dfrac{K}{b} + K_1 \\ 0 = -\dfrac{K}{a_c} + K_1 \rightarrow K = C_0 a_c \end{cases} \rightarrow \begin{cases} K_1 = \dfrac{C_0}{1-\gamma} \\ K = \dfrac{C_0 a_c}{1-\gamma} \end{cases}$$

Therefore, the final solution of Eq. A 23, for the Happel's model, is:

$$c = -\frac{1}{r}\frac{C_0 a_c}{(1-\gamma)} + \frac{C_0}{(1-\gamma)} = \frac{C_0}{(1-\gamma)}\left(1 - \frac{a_c}{r}\right)$$

Eq. A 31

The diffusion flux to the surface of the collector J_S is:

$$J_s = D\left(\frac{\partial c}{\partial r}\right)_{r=a_c} = \frac{DC_0}{(1-\gamma)}\left(\frac{a_c}{r^2}\right)_{r=a_c} = \frac{DC_0}{(1-\gamma)a_c}$$

Eq. A 32

and the total flux I_s:

$$I_s = \int_{S\_sphere} J_S dS = \frac{DC_0}{(1-\gamma)a_c} 4\pi a_c^2 = \frac{4\pi a_c DC_0}{(1-\gamma)}$$

Eq. A 33

By dividing I_s by the advective flux coming from the collector projection (definition of η_0) we obtain:

$$\eta_0^D = \frac{4\pi a_c DC_0 / (1-\gamma)}{C_0 U \pi a_c^2} = \frac{8}{(1-\gamma)} N_{Pe}^{-1}$$

Eq. A 34

The diffusive flux coming from the entire fluid shell surface of radius b, I_{FSb}, is reported in Eq. A 36.

$$J_b = D\left(\frac{\partial c}{\partial r}\right)_{r=b} = \frac{DC_0}{(1-\gamma)}\left(\frac{a_c}{r^2}\right)_{r=b} = \frac{DC_0 a_c}{(1-\gamma)b^2} = \gamma^2 \frac{DC_0}{(1-\gamma)a_c}$$

Eq. A 35

$$I_{FSb} = \int_{S\_FSb} J_b dS = \gamma^2 \frac{DC_0}{(1-\gamma)a_c} 4\pi b^2 = \frac{4\pi a_c DC_0}{(1-\gamma)}$$

Eq. A 36

The diffusive flux that enters only from the part of the fluid shell which corresponds to the collector projection (I_{FSac} - a schematic representation and the area calculation are shown in Figure A 18) is:

$$I_{FSa_c} = \int_{S\_FSa_c} J_b dS = \gamma^2 \frac{DC_0}{(1-\gamma)a_c} 2\pi bh = \gamma^2 \frac{DC_0}{(1-\gamma)a_c} 2\pi b^2 \left(1-\sqrt{1-\gamma^2}\right) = \frac{2\pi a_c DC_0}{(1-\gamma)}\left(1-\sqrt{1-\gamma^2}\right)$$

Eq. A 37

Assuming that this particular area can be assimilate with a plan (circle of area πa_c^2) (this is valid if $n \to 1$) the following flux can be considered instead of Eq. A 37:

$$I_{\pi a_c^2} = \int_{S\_\pi a_c^2} J_b dS = \gamma^2 \frac{DC_0}{(1-\gamma)a_c} \pi a_c^2 = \gamma^2 \frac{\pi a_c DC_0}{(1-\gamma)}$$

Eq. A 38

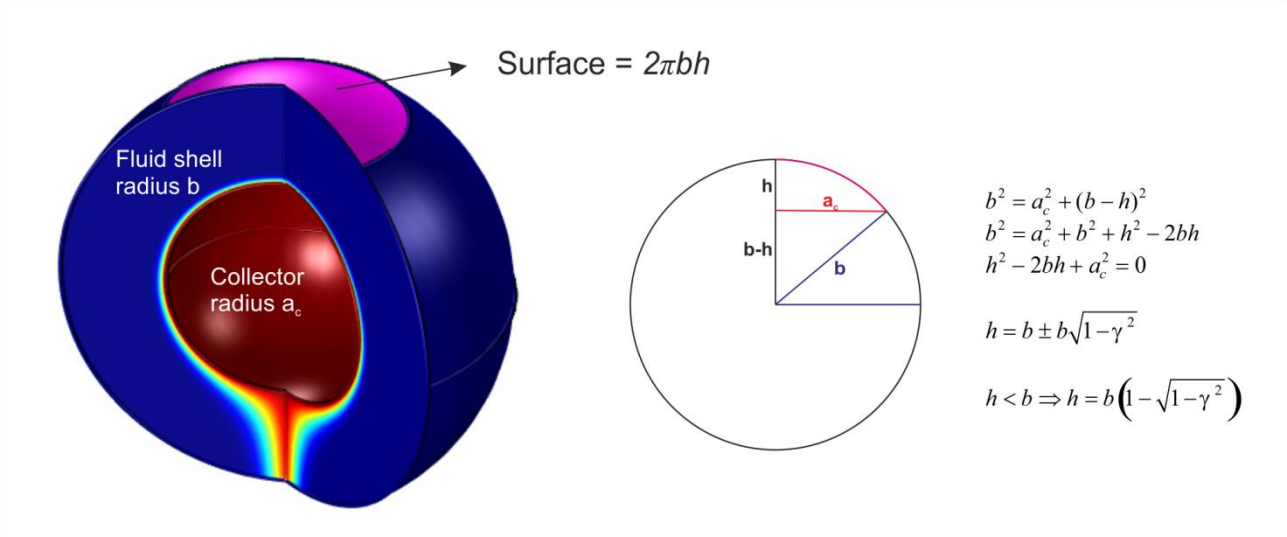

Figure A 18: Area of the fluid envelope which corresponds to the collector projection.

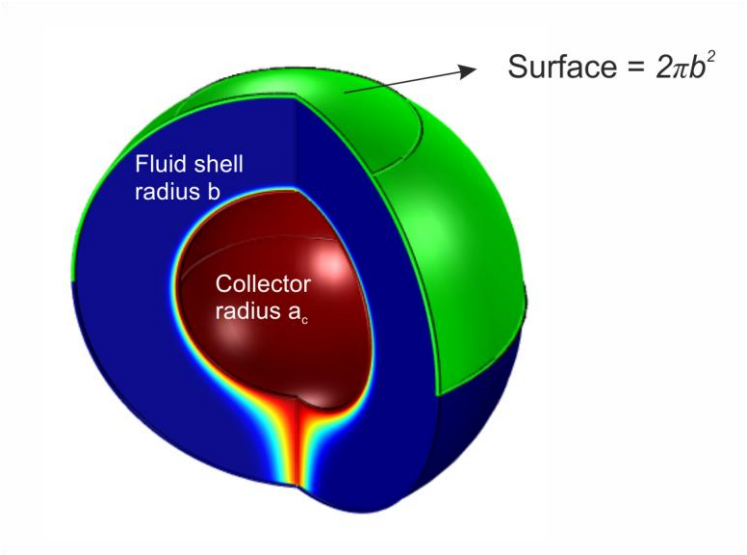

Figure A 19: Area of the semi fluid envelope.

If Song and Elimelech (Song and Elimelech 1992) boundary conditions (particle inlet only from the semi upper part of the fluid envelope, Figure A 19) are considered, both the total flux on the collector I_s and that from the fluid shell I_{FSb}, need to be divided by two, leading to:

$$I_S = \frac{2\pi a_c DC_0}{(1-\gamma)}$$

Eq. A 39

$$I_{FSb} = \frac{2\pi a_c DC_0}{(1-\gamma)}$$

Eq. A 40

$I_{\pi a_c^2}$ and I_{FSa_c} do not change.

Eq. A 39 and Eq. A 40 were used in our original correlation equations of η_N and η_0 (Eq. 2-9 and Eq. 2-10) in order to correct the pure diffusion term, leading to the final forms of Eq. 2-11 and Eq. 2-12, which:

1. consider porosity dependency in the advection terms thought A_S ;
2. consider porosity dependency in the pure diffusion term by introducing $(2-2\gamma)$ (according with Song and Elimelech boundary conditions);
3. normalize the efficiency over the entire semi fluid shell of radius *b*, by considering also γ^2 ($\eta_{0,\gamma}$).

If we want to consider the projection of the collector (thus neglect the third point of the list above) Eq. A 41 can be used for the non-normalized efficiency η_0 and Eq. A 42 (obtained by using Eq. A 37) for the *total flux normalized* efficiency η_N (or Eq. A 43 if the simplified Eq. A 38 is considered instead).

$$\eta_{0,a_c} = \left[1.5062 A_S N_R^{1.9834} + N_G\left(1+6.0187 N_R^2\right) + N_{Pe}^{-1}\left(7.5609+4.9534 N_R^1\right)/(2-2\gamma) + \right.$$
$$+ A_S^{0.1259} N_G^{0.8741}\left(0.0442+0.1220 N_R^{0.4210}\right) + A_S^{0.3662} N_{Pe}^{-0.6338}\left(2.9352+2.7480 N_R^{0.3737}\right) +$$
$$\left. + N_G^{0.6550} N_{Pe}^{-0.3450}\left(0.9461+1.1626 N_R^{0.6012}\right) + A_S^{0.1562} N_G^{0.5873} N_{Pe}^{-0.2565}\left(-0.6740-0.7119 N_R^{0.5438}\right)\right]$$

Eq. A 41

$$\eta_{N,a_c} = \eta_{0,a_c} / \left[\left(1+A_S\, 6.0098 N_R^{1.9834}\right) + N_G\left(1+6.0187 N_R^2\right) + \left(1-\sqrt{1-\gamma^2}\right) N_{Pe}^{-1}\left(7.5609+4.9534 N_R^1\right)/(2-2\gamma) + \right.$$
$$+ A_S^{0.1259} N_G^{0.8741}\left(0.0442+0.1220 N_R^{0.4210}\right) + A_S^{0.3662} N_{Pe}^{-0.6338}\left(2.9352+2.7480 N_R^{0.3737}\right) +$$
$$\left. N_G^{0.6550} N_{Pe}^{-0.3450}\left(2.7972+3.4372 N_R^{0.6012}\right) + A_S^{0.1562} N_G^{0.5873} N_{Pe}^{-0.2565}\left(-1.1945-1.2616 N_R^{0.5438}\right)\right]$$

Eq. A 42

$$\eta_{N,a_c} = \eta_{0,a_c} / \left[\left(1+A_S\, 6.0098 N_R^{1.9834}\right) + N_G\left(1+6.0187 N_R^2\right) + \gamma^2 N_{Pe}^{-1}\left(7.5609+4.9534 N_R^1\right)/(4-4\gamma) + \right.$$
$$+ A_S^{0.1259} N_G^{0.8741}\left(0.0442+0.1220 N_R^{0.4210}\right) + A_S^{0.3662} N_{Pe}^{-0.6338}\left(2.9352+2.7480 N_R^{0.3737}\right) +$$
$$\left. N_G^{0.6550} N_{Pe}^{-0.3450}\left(2.7972+3.4372 N_R^{0.6012}\right) + A_S^{0.1562} N_G^{0.5873} N_{Pe}^{-0.2565}\left(-1.1945-1.2616 N_R^{0.5438}\right)\right]$$

Eq. A 43

Table A 1 reports a summary of the results presented in this appendix.

Table A 1: Summary of the diffusion fluxes. (TE) (Tufenkji and Elimelech 2004), (SE) (Song and Elimelech 1992)

Geometry	Boundary Conditions	Flux	Mathematical value	Efficiency η_0^D
Isolate sphere	-	On the collector I_s	$I_s = 4\pi a_c D C_0$	$\eta_0^D = 8N_{Pe}^{-1}$
Happel's model	TE	On the collector I_s	$I_s = \frac{4\pi a_c D C_0}{(1-\gamma)}$	$\eta_0^D = \frac{8}{(1-\gamma)} N_{Pe}^{-1}$
	SE	On the collector I_s	$I_s = \frac{2\pi a_c D C_0}{(1-\gamma)}$	$\eta_0^D = \frac{8}{(2-2\gamma)} N_{Pe}^{-1}$
	TE	Entire fluid shell I_{FSb}	$I_{FS} = \frac{4\pi a_c D C_0}{(1-\gamma)}$	$\eta^D = \frac{8}{(1-\gamma)} N_{Pe}^{-1}$
	SE	Entire fluid shell I_{FSb}	$I_{FS} = \frac{2\pi a_c D C_0}{(1-\gamma)}$	$\eta^D = \frac{8}{(2-2\gamma)} N_{Pe}^{-1}$
	-	Fluid shell corresponding to the collector projection I_{FSac}	$I_{FSa_c} = \frac{2\pi a_c D C_0}{(1-\gamma)}\left(1-\sqrt{1-\gamma^2}\right)$	$\eta^D = \frac{8}{(2-2\gamma)} N_{Pe}^{-1}\left(1-\sqrt{1-\gamma^2}\right)$
	-	Circle corresponding to the collector projection $I_{\pi a_c^2}$	$I_{\pi a_c^2} = \gamma^2 \frac{\pi a_c D C_0}{(1-\gamma)}$	$\eta^D = \gamma^2 \frac{8}{(4-4\gamma)} N_{Pe}^{-1}$

Annex V - Reduced models

The reduced models for η_N and η_0, reported in Eq. 2-13 and Eq. 2-14, were obtained by eliminating progressively each term from the full equations and by evaluating, each time, the residual between the "reduced" model and the CFD data, mediating this residual on the full and wide data set. Therefore, the terms were classified based on their weight (the bigger was the residual between the numerical data and the model without the *i*-term, the more important was the *i*-term).

Obviously the weight of each term with respect to the others depends on the system parameters (e.g., the relative importance between interception and gravity depends on particle density).

If, in the derivation of the reduced model, a particular range of parameters had been considered, instead of the entire and wide range of data, the relative importance of each term would have been different, but the results would not have been equally general.

In the following figures η_N and η_0 are decomposed in their single terms (η_0 like in Eq. 2-7 and η_N in the same way, but considering for each term, the full denominator). As inferable from Figure A 20 and Figure A 21, some mechanisms are more important than others, the importance of each mechanism is function of the particle size, but also of particle density, flow velocity, etc. The pure diffusion term (η_0^D and η_N^D) and the advective-diffusive term (η_0^{AD} and η_N^{AD}) are always predominant for small particle (low N_{Pe}) and the gravity term (η_0^G and η_N^G) is always the most important for big particles (in case $\rho_p \neq \rho_f$). Instead the interception term (η_0^{AS} and η_N^{AS}) can be more or less important depending on particle density and on flow velocity. Therefore different reduced models can be proposed, depending on the parameters which characterize the system.

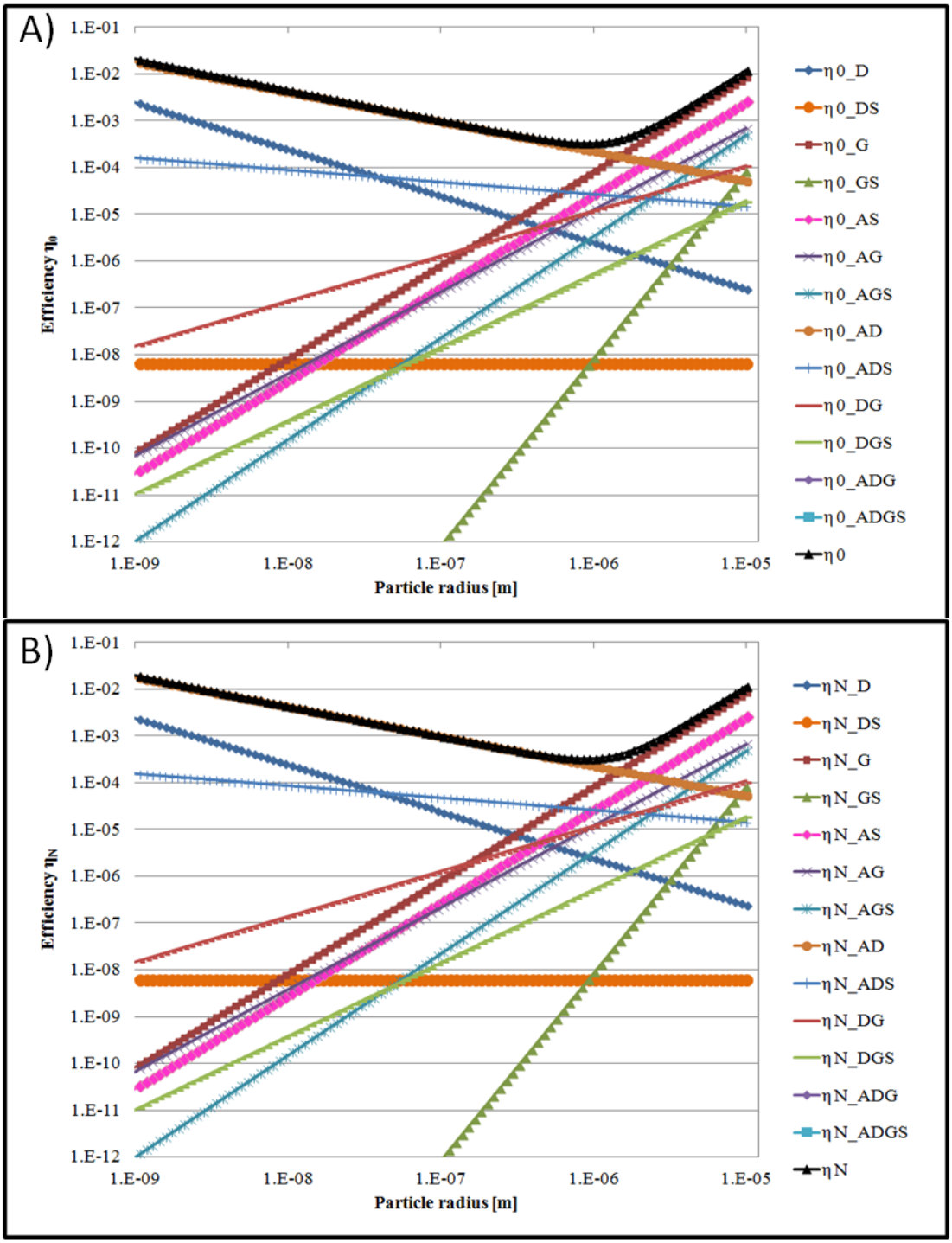

Figure A 20: Decomposition of η_0 (A) and η_N (B) in their terms. Data: U=1.36·10^{-3}m/s, ρ_p =1050 kg/m^3, ρ_f =998 kg/m^3, T=298 K, μ =9.8·10^{-4} Pa·s and a_c =250 µm.

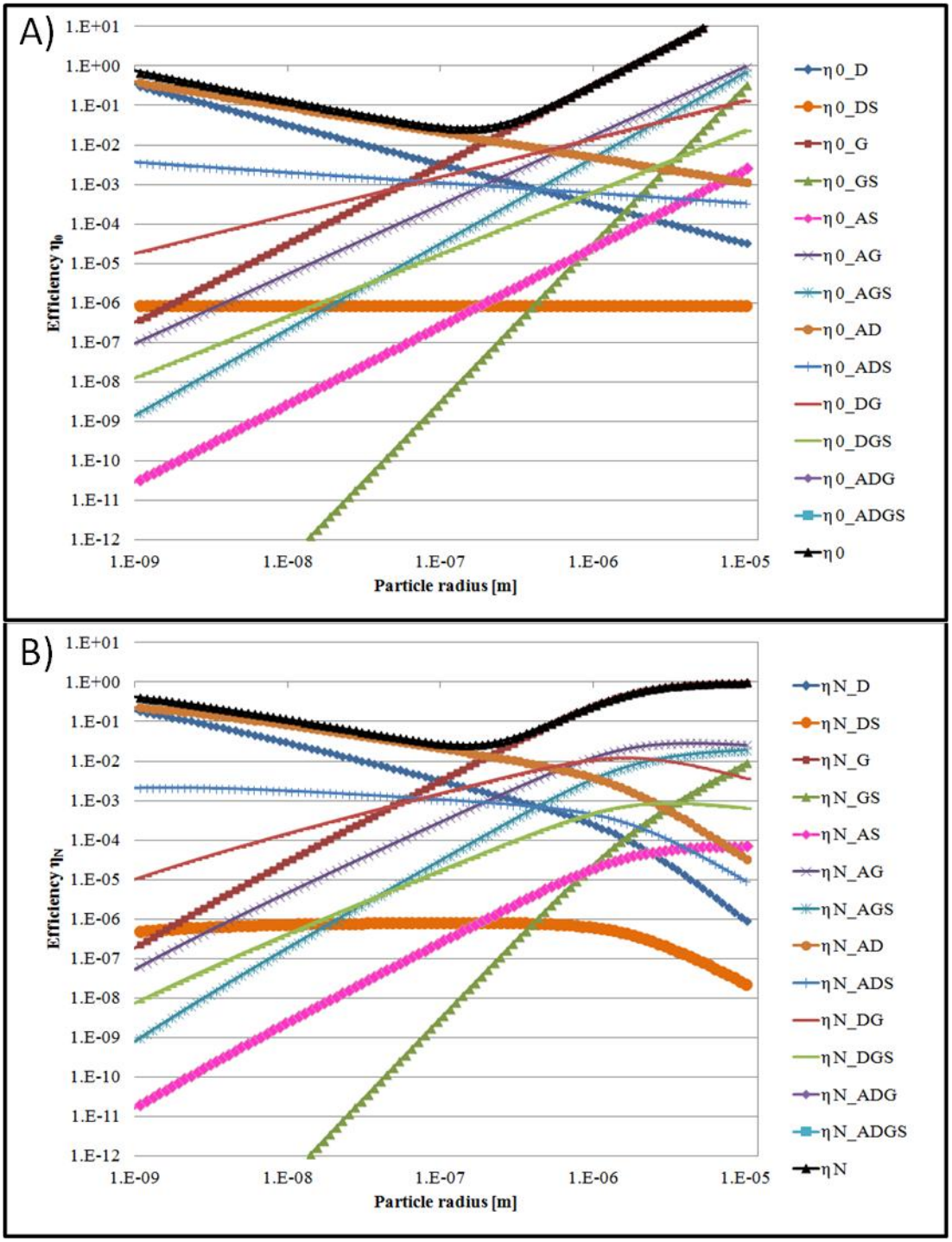

Figure A 21: Decomposition of η_0 (A) and η_N (B) in their terms. Data: U=10^{-5}m/s, ρ_p =2500 kg/m^3, ρ_f =998 kg/m^3, T=298 K, μ =9.8·10^{-4} Pa·s and a_c =250 µm.

References

Adamczyk, Z., et al.
1983 Particle Transfer to Solid-Surfaces. Advances in Colloid and Interface Science 19(3):183-252.
Bensaid, S., D. L. Marchisio, and D. Fino
2010 Numerical simulation of soot filtration and combustion within diesel particulate filters. Chemical Engineering Science 65(1):357-363.
Bensaid, S., et al.
2009 Experimental investigation of soot deposition in diesel particulate filters. Catalysis Today 147:S295-S300.
Bhattacharjee, S., J. N. Ryan, and M. Elimelech
2002 Virus transport in physically and geochemically heterogeneous subsurface porous media. Journal of Contaminant Hydrology 57(3-4):161-187.
Blunt, M. J.
2001 Flow in porous media — pore-network models and multiphase flow. Current Opinion in Colloid & Interface Science 6(3):197-207.
Blunt, Martin, and Peter King
1990 Macroscopic parameters from simulations of pore scale flow. Physical Review A 42(8):4780.
Boccardo, G., D. L. Marchisio, and R. Sethi
2014 Microscale simulation of particle deposition in porous media. J Colloid Interface Sci 417:227-37.
Bradford, S. A., et al.
2014 Modeling Microorganism Transport and Survival in the Subsurface. Journal of Environmental Quality 43(2):421-440.
Brenner, H.
1961 The slow motion of a sphere through a viscous fluid towards a plane surface. Chemical Engineering Science 16(3-4):242-251.
Brinkman, HC
1947 A calculation of the viscosity and the sedimentation constant for solutions of large chain molecules taking into account the hampered flow of the solvent through these molecules. Physica 13(8):447-448.
Comba, S., et al.
2011 Rheological characterization of xanthan suspensions of nanoscale iron for injection in porous media. Journal of Hazardous Materials 185(2-3):598-605.
Cushing, Robert S., and Desmond F. Lawler
1998 Depth Filtration: Fundamental Investigation through Three-Dimensional Trajectory Analysis. Environmental Science & Technology 32(23):3793-3801.
Dalla Vecchia, E., M. Luna, and R. Sethi
2009 Transport in Porous Media of Highly Concentrated Iron Micro- and Nanoparticles in the Presence of Xanthan Gum. Environmental Science & Technology 43(23):8942-8947.
de Vicente, J., et al.
2000 Stability of Cobalt Ferrite Colloidal Particles. Effect of pH and Applied Magnetic Fields Langmuir 16(21):7954 -7961.
Elimelech, M.
1994 Particle deposition on ideal collectors from dilute flowing suspensions: Mathematical formulation, numerical solution, and simulations. Separations Technology 4(4):186-212.
—
1995 Particle deposition and aggregation : measurement, modelling, and simulation. Oxford [England] ; Boston: Butterworth-Heinemann.
Fenwick, Darryl H, and Martin J Blunt
1998 Three-dimensional modeling of three phase imbibition and drainage. Advances in Water Resources 21(2):121-143.
Ferziger, J.H., and M. Peric
1999 Computational Methods for fluid Dynamics Berlin: Springer
Garcia-Otero, J., et al.

2000 Influence of dipolar interaction on magnetic properties of ultrafine ferromagnetic particles. Physical Review Letters 84(1):167-170.

Gordon, A. C., et al.
2014 Localized Hyperthermia with Iron Oxide-Doped Yttrium Microparticles: Steps toward Image-Guided Thermoradiotherapy in Liver Cancer. Journal of Vascular and Interventional Radiology 25(3):397-404.

Gregory, J.
1981 Approximate Expressions for Retarded Vanderwaals Interaction. Journal of Colloid and Interface Science 83(1):138-145.

Happel, J., and H. Brenner
1983 Low Reynolds number hydrodynamics with special applications to particulate media. The Hague: M. Nijhoff.

Happel, John
1958 Viscous flow in multiparticle systems: Slow motion of fluids relative to beds of spherical particles. Aiche Journal 4(2):197-201.

Hogg, R., T. W. Healy, and D. W. Fuerstenau
1966 Mutual coagulation of colloidal dispersions. Transactions of the Faraday Society 62:1638.

Hunter, Robert J.
2001 Foundations of colloid science. Oxford ; New York: Oxford University Press.

Johnson, W. P., and M. Hilpert
2013 Upscaling colloid transport and retention under unfavorable conditions: Linking mass transfer to pore and grain topology. Water Resources Research 49(9):5328-5341.

Johnson, WP, Xiqing Li, and Gozde Yal
2007 Colloid retention in porous media: Mechanistic confirmation of wedging and retention in zones of flow stagnation. Environmental science & technology 41(4):1279-1287.

Kamiyama, Y., and J. Israelachvili
1992 Effect of Ph and Salt on the Adsorption and Interactions of an Amphoteric Polyelectrolyte. Macromolecules 25(19):5081-5088.

Kocur, C. M., et al.
2014 Characterization of nZVI Mobility in a Field Scale Test. Environmental Science & Technology 48(5):2862-2869.

Levich, V. G.
1962 Physicochemical hydrodynamics. Englewood Cliffs, N.J.,: Prentice-Hall.

Liang, Y., et al.
2013 Retention and Remobilization of Stabilized Silver Nanoparticles in an Undisturbed Loamy Sand Soil. Environmental Science & Technology 47(21):12229-12237.

Lifshitz, E. M.
1956 Theory of molecular attractive forces. Soviet Physics JETP 2:73-83.

Logan, B. E., et al.
1995 Clarification of clean-bed filtration models. Journal of Environmental Engineering 121(12):869-873.

Long, W., and M. Hilpert
2009 A Correlation for the Collector Efficiency of Brownian Particles in Clean-Bed Filtration in Sphere Packings by a Lattice-Boltzmann Method. Environmental Science & Technology 43(12):4419-4424.

Loveland, J. P., et al.
2003 Colloid transport in a geochemically heterogeneous porous medium: aquifer tank experiment and modeling. Journal of Contaminant Hydrology 65(3-4):161-182.

Lowry, Michael I, and Cass T Miller
1995 Pore-Scale Modeling of Nonwetting-Phase Residual in Porous Media. Water Resources Research 31(3):455-473.

Ma, H. L., M. Hradisky, and W. P. Johnson
2013 Extending Applicability of Correlation Equations to Predict Colloidal Retention in Porous Media at Low Fluid Velocity. Environmental Science & Technology 47(5):2272-2278.

Ma, Huilian, et al.
2009 Hemispheres-in-Cell Geometry to Predict Colloid Deposition in Porous Media. Environmental Science & Technology 43(22):8573-8579.

Masliyah, Jacob H., and Subir Bhattacharjee
2006 Electrokinetic and colloid transport phenomena. Hoboken, N.J.: Wiley-Interscience.

Matijevic, E.
1971 Surface and Colloid Science. New York Wiley.

Mccarthy, J. F., and J. M. Zachara
1989 Subsurface Transport of Contaminants - Mobile Colloids in the Subsurface Environment May Alter the Transport of Contaminants. Environmental Science & Technology 23(5):496-502.
Meakin, Paul, and Alexandre M. Tartakovsky
2009 Modeling and simulation of pore-scale multiphase fluid flow and reactive transport in fractured and porous media. Reviews of Geophysics 47(3):RG3002.
Mehmani, A., M. Prodanovic, and F. Javadpour
2013 Multiscale, Multiphysics Network Modeling of Shale Matrix Gas Flows. Transport in Porous Media 99(2):377-390.
Messina, F., D. Marchisio, and R. Sethi
2015 An extended and total flux normalized correlation equation for predicting single-collector efficiency. Journal of Colloid and Interface Science 446:185-193.
Nelson, K. E., and T. R. Ginn
2011 New collector efficiency equation for colloid filtration in both natural and engineered flow conditions. Water Resources Research 47.
Nelson, K. E., T. R. Ginn, and T. Kemai
2013 Comment on "Extending Applicability of Correlation Equations to Predict Colloidal Retention in Porous Media at Low Fluid Velocity". Environmental Science & Technology 47(14):8078-8079.
Nelson, Kirk E., and Timothy R. Ginn
2005 Colloid Filtration Theory and the Happel Sphere-in-Cell Model Revisited with Direct Numerical Simulation of Colloids. Langmuir 21(6):2173-2184.
O'Carroll, D., et al.
2013 Nanoscale zero valent iron and bimetallic particles for contaminated site remediation. Advances in Water Resources 51:104-122.
O'May, C., and N. Tufenkji
2011 The Swarming Motility of Pseudomonas aeruginosa Is Blocked by Cranberry Proanthocyanidins and Other Tannin-Containing Materials. Applied and Environmental Microbiology 77(9):3061-3067.
Pankhurst, Q. A., et al.
2009 Progress in applications of magnetic nanoparticles in biomedicine. Journal of Physics D-Applied Physics 42(22).
Payatake.Ac, C. Tien, and R. M. Turian
1973 New Model for Granular Porous Media - Model Formulation. Aiche Journal 19(1):58-67.
Petosa, A. R., et al.
2010 Aggregation and Deposition of Engineered Nanomaterials in Aquatic Environments: Role of Physicochemical Interactions. Environmental Science & Technology 44(17):6532-6549.
Pfeffer, R.
1964 Heat and Mass transport in multiparticle systems.
Phenrat, T., et al.
2007 Aggregation and sedimentation of aqueous nanoscale zerovalent iron dispersions. Environmental Science & Technology 41(1):284-290.
Prieve, Dennis C., and Eli Ruckenstein
1974 Effect of London forces upon the rate of deposition of Brownian particles. Aiche Journal 20(6):1178-1187.
Prodanovic, M., S. L. Bryant, and Z. T. Karpyn
2010 Investigating Matrix/Fracture Transfer via a Level Set Method for Drainage and Imbibition. Spe Journal 15(1):125-136.
Rajagopalan, Rajamani, and Chi Tien
1976 Trajectory analysis of deep-bed filtration with the sphere-in-cell porous media model. Aiche Journal 22(3):523-533.
Ruckenstein, E., and D. C. Prieve
1976 Adsorption and Desorption of Particles and Their Chromatographic-Separation. Aiche Journal 22(2):276-283.
Ryan, Joseph N, and Menachem Elimelech
1996 Colloid mobilization and transport in groundwater. Colloids and Surfaces A: Physicochemical and Engineering Aspects 107:1-56.
Saiers, James E., and J. N. Ryan
2005 Colloid deposition on non-ideal porous media: The influences of collector shape and roughness on the single-collector efficiency. Geophysical Research Letters 32(21):L21406.
Schijven, J. F., et al.

2000 Removal of microorganisms by deep well injection. Journal of Contaminant Hydrology 44(3-4):301-327.

Seetha, N., et al.
2014 Virus-sized colloid transport in a single pore: Model development and sensitivity analysis. Journal of Contaminant Hydrology 164:163-180.

Shi, X. Y., et al.
2013 Coupled solid and fluid mechanics modeling of formation damage near wellbore. Journal of Petroleum Science and Engineering 112:88-96.

Song, L. F., and M. Elimelech
1992 Deposition of Brownian Particles in Porous-Media - Modified Boundary-Conditions for the Sphere-in-Cell Model. Journal of Colloid and Interface Science 153(1):294-297.

Syngouna, V. I., and C. V. Chrysikopoulos
2012 Transport of biocolloids in water saturated columns packed with sand: Effect of grain size and pore water velocity (vol 126, pg 301, 2011). Journal of Contaminant Hydrology 129:10-10.

Tien, C., and A. C. Payatakes
1979 Advances in Deep Bed Filtration. Aiche Journal 25(5):737-759.

Tien C., Ramarao B.V.
1989 Granular Filtration of Aerosols and Hydrosols.

Tiraferri, A., et al.
2008 Reduced aggregation and sedimentation of zero-valent iron nanoparticles in the presence of guar gum. Journal of Colloid and Interface Science 324(1-2):71-79.

Tobiason, John E., and Charles R. O'Melia
1988 Physicochemical aspects of particle removal in depth filtration. Journal / American Water Works Association 80(12):54-64.

Tosco, T.
2010 Modelling the transport of iron-based colloids in saturated porous media, Politecnico di Torino.

Tosco, T., et al.
2013 Extension of the Darcy-Forchheimer Law for Shear-Thinning Fluids and Validation via Pore-Scale Flow Simulations. Transport in Porous Media 96(1):1-20.

Tosco, T., et al.
Submitted Computational models for nanoparticle transport in porous media: from pore- to macro-scale.

Tosco, T., et al.
2014 Nanoscale zerovalent iron particles for groundwater remediation: a review. Journal of Cleaner Production 77:10-21.

Tufenkji, N., and M. Elimelech
2004 Correlation equation for predicting single-collector efficiency in physicochemical filtration in saturated porous media. Environmental Science & Technology 38(2):529-536.

—
2005 Response to comment on "Correlation equation for predicting single-collector efficiency in physicochemical filtration in saturated porous media". Environmental Science & Technology 39(14):5496-5497.

Vincent, B., et al.
1986 Depletion Flocculation in Dispersions of Sterically-Stabilized Particles (Soft Spheres). Colloids and Surfaces 18(2-4):261-281.

Warszyński, Piotr
2000 Coupling of hydrodynamic and electric interactions in adsorption of colloidal particles. Advances in Colloid and Interface Science 84(1–3):47-142.

Wei, Yu-Ting, and Shian-chee Wu
2010 Development of a Trajectory Model for Predicting Attachment of Submicrometer Particles in Porous Media: Stabilized NZVI as a Case Study. Environmental Science & Technology 44(23):8996-9002.

Yao, K. M.
1968 Influence of suspended particle size on the transport aspect of water filtration, Engineering, sanitary and municipal, University of North Carolina at Chapel Hill.

Yao, Kuan-Mu, Mohammad T. Habibian, and Charles R. O'Melia
1971 Water and waste water filtration. Concepts and applications. Environmental Science & Technology 5(11):1105-1112.